

AFGL-TR-85-0115  
SDL/85-032

4  
DTIC FILE COPY

AD-A189 105

ROCKETBORNE AND GROUND BASED MEASUREMENTS IN SUPPORT OF  
THE FIELD-WIDENED INTERFEROMETER EXPERIMENT - SERGEANT A30.276

by

J.C. Ulwick, G.D. Allred, K.D. Baker and L.C. Howlett

Space Dynamics Laboratories  
Utah State University UMC-41  
Logan, Utah 84322

28 May 1985

Scientific Report No. 7

Approved for Public Release  
Distribution Unlimited

Prepared for:

Air Force Geophysics Laboratory  
Air Force Systems Command  
United States Air Force  
Hanscom AFB, Massachusetts 01731

DTIC  
SELECTED  
FEB 08 1988  
D  
E

88 1 28 034

Unclassified

SECURITY CLASSIFICATION OF THIS PAGE

REPORT DOCUMENTATION PAGE

|   |  |  |                           |
|---|--|--|---------------------------|
| 1a. REPORT SECURITY CLASSIFICATION<br>Unclassified  |  | 1b. RESTRICTIVE MARKINGS   |                           |
| 2a. SECURITY CLASSIFICATION AUTHORITY   |  | 3. DISTRIBUTION/AVAILABILITY OF REPORT   |                           |
| 2b. DECLASSIFICATION/DOWNGRADING SCHEDULE   |  | Approved for public release; distribution unlimited.                                       |                           |
| 4. PERFORMING ORGANIZATION REPORT NUMBER(S)<br>SDL/85-032   |  | 5. MONITORING ORGANIZATION REPORT NUMBER(S)<br>AFGL-TR-85-0115                             |                           |
| 6a. NAME OF PERFORMING ORGANIZATION<br>Space Dynamics Laboratories  | 6b. OFFICE SYMBOL<br>(If applicable)   | 7a. NAME OF MONITORING ORGANIZATION<br>Air Force Geophysics Laboratory                     |                           |
| 6c. ADDRESS (City, State and ZIP Code)<br>Utah State University<br>Logan, Utah 84322-4140   |  | 7b. ADDRESS (City, State and ZIP Code)<br>L.G. Hanscom Air Force Base<br>Bedford, MA 01731 |                           |
| 8a. NAME OF FUNDING/SPONSORING<br>ORGANIZATION<br>AFGL  | 8b. OFFICE SYMBOL<br>(If applicable)   | 9. PROCUREMENT INSTRUMENT IDENTIFICATION NUMBER<br>F19628-83-C-0056                        |                           |
| 10. SOURCE OF FUNDING NOS.  |  | 11. TITLE (Include Security Classification)<br>See Block 16                                |                           |
| 12. PERSONAL AUTHORIS<br>J.C. Ulwick, G.D. Allred, R.D. Baker, and L.C. Howlett   |  |  |                           |
| 13a. TYPE OF REPORT<br>Scientific No. 7   | 13b. TIME COVERED<br>FROM _____ TO _____   | 14. DATE OF REPORT (Yr., Mo., Day)<br>28 May 1985  | 15. PAGE COUNT<br>108     |
| 16. SUPPLEMENTARY NOTATION<br>Rocketborne and Ground Based Measurements in Support of the Field-Widened Interferometer Experiment - Sergeant A30.276  |  |  |                           |
| 17. COSATI CODES<br>FIELD    GROUP    SUB. GR.<br>1    1C    1C   | 18. SUBJECT TERMS (Continue on reverse if necessary and identify by block number)<br>Auroral measurements, Rocket Payload Instrumentation, Rocketborne/Ground Based Auroral Measurements |  |                           |
| 19. ABSTRACT (Continue on reverse if necessary and identify by block number)<br>In April 1983 Utah State University and Air Force Geophysics Laboratory experimenters launched a Sergeant (A30.276) sounding rocket from the Poker Flat Research Range, Alaska. The prime purpose of the flight was to obtain infrared spectral measurements in the 2 - 1.5 $\mu$ m range during an auroral event. In addition to the prime experiment, which has already been reported, the payload contained four photometers, and energy deposition scintillator and an atomic oxygen detector to gather <u>in-situ</u> supporting data. Simultaneously, all-sky television, meridian scanning photometers, riometer, and magnetometers supported the flight from ground based measuring sites. This report presents a summary of the rocketborne supporting instruments and the data they gathered and provides a time/intensity history of the event as documented by the ground based meridian scanners and all-sky television. |  |  |                           |
| 20. DISTRIBUTION/AVAILABILITY OF ABSTRACT<br>UNCLASSIFIED/UNLIMITED <input checked="" type="checkbox"/> SAME AS RPT. <input type="checkbox"/> DTIC USERS <input type="checkbox"/>   |  | 21. ABSTRACT SECURITY CLASSIFICATION<br>Unclassified                                       |                           |
| 22a. NAME OF RESPONSIBLE INDIVIDUAL<br>Monitor: Francis X. Robert   |  | 22b. TELEPHONE NUMBER<br>(Include Area Code)<br>(617) 377-3641                             | 22c. OFFICE SYMBOL<br>LSP |

## LIST OF CONTRIBUTORS

### Utah State University

Allan J. Steed, Principal Investigator

G.D. Allred  
J.C. Ballard  
K.D. Baker  
D.R. Bunnell  
L.C. Howlett  
J.C. Ulwick

### Defense Nuclear Agency

Wm. McKeckney, Col.

### Air Force Geophysics Laboratory

F. Cook  
S. Hoskins  
A. McIntyre  
R. Murphy  
A.T. Stair, Jr.  
R. Straka

## RELATED CONTRACTS AND PUBLICATIONS

F19628-81-C-0140  
F19628-77-C-0203  
F19628-76-C-0261



Burt, D.A., and G.D. Allred, Rocketborne ionospheric studies: 1976-1979, Final Report AFGL-TR-79-0179, Contract No. F19628-76-C-0261, 148 pp., Space Measurements Laboratory, Utah State University, Logan, 6 August 1979.  
ADA078799

|                    |                                     |
|--------------------|-------------------------------------|
| Accession For      |                                     |
| NTIS GRA&I         | <input checked="" type="checkbox"/> |
| DTIC TAB           | <input type="checkbox"/>            |
| Unannounced        | <input type="checkbox"/>            |
| Justification      |                                     |
| By                 |                                     |
| Distribution/      |                                     |
| Availability Codes |                                     |
| Dist               | Avail and/or<br>Special             |
| A-1                |                                     |

This page intentionally left blank.

## TABLE OF CONTENTS

|  | <u>Page</u> |
|--|-------------|
| DD1473 . . . . .   | i           |
| LIST OF CONTRIBUTORS . . . . .                                 | .iii        |
| RELATED CONTRACTS AND PUBLICATIONS . . . . .                   | .iii        |
| LIST OF ILLUSTRATIONS. . . . .                                 | .vii        |
| LIST OF TABLES . . . . .                                       | xiii        |
| INTRODUCTION . . . . .   | 1           |
| FLIGHT SUMMARY . . . . .                                       | 3           |
| INSTRUMENTATION. . . . .                                       | 5           |
| Flight Instrumentation. . . . .                                | 5           |
| Field-Widened Interferometer . . . . .                         | 7           |
| Atomic Oxygen Detector . . . . .                               | 8           |
| Energy Deposition Scintillator . . . . .                       | 12          |
| Photometers. . . . .   | 15          |
| Ground Based Support Instrumentation. . . . .                  | 19          |
| APPENDIX A - Atomic Oxygen Detector ATOX 83-1. . . . .         | 73          |
| APPENDIX B - Energy Deposition Scintillator EDS 75-7 . . . . . | 81          |
| APPENDIX C - Photometers PM2-96, PM2-99B, PM2-107B . . . . .   | 85          |

This page intentionally left blank.

## LIST OF ILLUSTRATIONS

| <u>Figure No.</u> | <u>Title</u>  | <u>Page No.</u> |
|-------------------|---|-----------------|
| 1 . . . . .       | Sergeant A30.276 trajectory . . . . .   | 4               |
| 2 . . . . .       | Sergeant A30.276 payload configuration. . . . .   | 6               |
| 3 . . . . .       | Atomic oxygen detector - block diagram. . . . .   | 10              |
| 4 . . . . .       | Atomic oxygen detector - density profile measured during the flight of A30.276. . . . .   | 11              |
| 5 . . . . .       | Energy deposition scintillator - block diagram. . . . .   | 13              |
| 6 . . . . .       | Energy deposition scintillator - ascent and descent power density profiles measured during the flight of A30.276 . . . . .                          | 14              |
| 7 . . . . .       | Photometer - block diagram. . . . .   | 15              |
| 8 (a & b) . . .   | Photometer locations and fields of view orientations relative to field-widened interferometer field of view. . . . .                                | 17              |
| 9 . . . . .       | Emission intensity vs. altitude profile at 3914 Å as measured by photometers No. 1, 3, and 4 (PM2-107B, PM2-96, and PM2-998 respectively) . . . . . | 18              |
| 10 . . . . .      | Meridian scanning photometers at 5577 Å, 4278 Å, 6300 Å, and H <sub>β</sub> , for the time period T-979 seconds through T-939 seconds . . . . .     | 22              |
| 11 . . . . .      | Meridian scanning photometers at 5577 Å, 4278 Å, 6300 Å, and H <sub>β</sub> , for the time period T-939 seconds through T-891 seconds . . . . .     | 23              |
| 12 . . . . .      | Meridian scanning photometers at 5577 Å, 4278 Å, 6300 Å, and H <sub>β</sub> , for the time period T-891 seconds through T-843 seconds . . . . .     | 24              |
| 13 . . . . .      | Meridian scanning photometers at 5577 Å, 4278 Å, 6300 Å, and H <sub>β</sub> , for the time period T-843 seconds through T-795 seconds . . . . .     | 25              |
| 14 . . . . .      | Meridian scanning photometers at 5577 Å, 4278 Å, 6300 Å, and H <sub>β</sub> , for the time period T-795 seconds through T-747 seconds . . . . .     | 26              |
| 15 . . . . .      | Meridian scanning photometers at 5577 Å, 4278 Å, 6300 Å, and H <sub>β</sub> , for the time period T-747 seconds through T-699 seconds . . . . .     | 27              |

LIST OF ILLUSTRATIONS (Cont.)

| <u>Figure No.</u> | <u>Title</u>   | <u>Page No.</u> |
|-------------------|--|-----------------|
| 16 . . . . .      | Meridian scanning photometers at 5577 Å,<br>4278 Å, 6300 Å, and HB, for the time period<br>T-699 seconds through T-651 seconds . . . . . | 28              |
| 17 . . . . .      | Meridian scanning photometers at 5577 Å,<br>4278 Å, 6300 Å, and HB, for the time period<br>T-651 seconds through T-603 seconds . . . . . | 29              |
| 18 . . . . .      | Meridian scanning photometers at 5577 Å,<br>4278 Å, 6300 Å, and HB, for the time period<br>T-603 seconds through T-555 seconds . . . . . | 30              |
| 19 . . . . .      | Meridian scanning photometers at 5577 Å,<br>4278 Å, 6300 Å, and HB, for the time period<br>T-555 seconds through T-507 seconds . . . . . | 31              |
| 20 . . . . .      | Meridian scanning photometers at 5577 Å,<br>4278 Å, 6300 Å, and HB, for the time period<br>T-507 seconds through T-459 seconds . . . . . | 32              |
| 21 . . . . .      | Meridian scanning photometers at 5577 Å,<br>4278 Å, 6300 Å, and HB, for the time period<br>T-459 seconds through T-411 seconds . . . . . | 33              |
| 22 . . . . .      | Meridian scanning photometers at 5577 Å,<br>4278 Å, 6300 Å, and HB, for the time period<br>T-411 seconds through T-363 seconds . . . . . | 34              |
| 23 . . . . .      | Meridian scanning photometers at 5577 Å,<br>4278 Å, 6300 Å, and HB, for the time period<br>T-363 seconds through T-315 seconds . . . . . | 35              |
| 24 . . . . .      | Meridian scanning photometers at 5577 Å,<br>4278 Å, 6300 Å, and HB, for the time period<br>T-315 seconds through T-267 seconds . . . . . | 36              |
| 25 . . . . .      | Meridian scanning photometers at 5577 Å,<br>4278 Å, 6300 Å, and HB, for the time period<br>T-267 seconds through T-219 seconds . . . . . | 37              |
| 26 . . . . .      | Meridian scanning photometers at 5577 Å,<br>4278 Å, 6300 Å, and HB, for the time period<br>T-219 seconds through T-171 seconds . . . . . | 38              |
| 27 . . . . .      | Meridian scanning photometers at 5577 Å,<br>4278 Å, 6300 Å, and HB, for the time period<br>T-171 seconds through T-123 seconds . . . . . | 39              |
| 28 . . . . .      | All-sky TV frames at eight-second intervals<br>from T-95 seconds through T-79 seconds . . . . .  | 40              |

LIST OF ILLUSTRATIONS (Cont.)

| <u>Figure No.</u> | <u>Title</u>   | <u>Page No.</u> |
|-------------------|--|-----------------|
| 29 . . . . .      | Meridian scanning photometers at 5577 Å,<br>4278 Å, 6300 Å, and HB, for the time period<br>T-123 seconds through T-75 seconds. . . . .   | 41              |
| 30 . . . . .      | All-sky TV frames at eight-second intervals<br>from T-71 seconds through T-31 seconds. . . . .   | 42              |
| 31 . . . . .      | Meridian scanning photometers at 5577 Å,<br>4278 Å, 6300 Å, and HB, for the time period<br>T-75 seconds through T-27 seconds . . . . .   | 43              |
| 32 . . . . .      | All-sky TV frames at eight-second intervals<br>from T-23 seconds through T+17 seconds. . . . .   | 44              |
| 33 . . . . .      | Meridian scanning photometers at 5577 Å,<br>4278 Å, 6300 Å, and HB, for the time period<br>T-27 seconds through T-21 seconds . . . . .   | 45              |
| 34 . . . . .      | All-sky TV frames at eight-second intervals<br>from T-25 seconds through T+65 seconds. . . . .   | 46              |
| 35 . . . . .      | Meridian scanning photometers at 5577 Å,<br>4278 Å, 6300 Å, and HB, for the time period<br>T+21 seconds through T+69 seconds . . . . .   | 47              |
| 36 . . . . .      | All-sky TV frames at eight-second intervals<br>from T+73 seconds through T+113 seconds . . . . .   | 48              |
| 37 . . . . .      | Meridian scanning photometers at 5577 Å,<br>4278 Å, 6300 Å, and HB, for the time period<br>T+69 seconds through T+117 seconds. . . . .   | 49              |
| 38 . . . . .      | All-sky TV frames at eight-second intervals<br>from T+121 seconds through T+161 seconds. . . . .   | 50              |
| 39 . . . . .      | Meridian scanning photometers at 5577 Å,<br>4278 Å, 6300 Å, and HB, for the time period<br>T+117 seconds through T+165 seconds . . . . . | 51              |
| 40 . . . . .      | All-sky TV frames at eight-second intervals<br>from T+169 seconds through T+209 seconds. . . . .   | 52              |
| 41 . . . . .      | Meridian scanning photometers at 5577 Å,<br>4278 Å, 6300 Å, and HB, for the time period<br>T+165 seconds through T+213 seconds . . . . . | 53              |
| 42 . . . . .      | All-sky TV frames at eight-second intervals<br>from T+217 seconds through T+257 seconds. . . . .   | 54              |

LIST OF ILLUSTRATIONS (Cont.)

| <u>Figure No.</u> | <u>Title</u>   | <u>Page No.</u> |
|-------------------|--|-----------------|
| 43 . . . . .      | Meridian scanning photometers at 5577 Å,<br>4278 Å, 6300 Å, and HB, for the time period<br>T+213 seconds through T+261 seconds . . . . . | 55              |
| 44 . . . . .      | All-sky TV frames at eight-second intervals<br>from T+265 seconds through T+305 seconds. . . . .   | 56              |
| 45 . . . . .      | Meridian scanning photometers at 5577 Å,<br>4278 Å, 6300 Å, and HB, for the time period<br>T+261 seconds through T+309 seconds . . . . . | 57              |
| 46 . . . . .      | All-sky TV frames at eight-second intervals<br>from T+313 seconds through T+353 seconds. . . . .   | 58              |
| 47 . . . . .      | Meridian scanning photometers at 5577 Å,<br>4278 Å, 6300 Å, and HB, for the time period<br>T+309 seconds through T+357 seconds . . . . . | 59              |
| 48 . . . . .      | All-sky TV frames at eight-second intervals<br>from T+361 seconds through T+401 seconds. . . . .   | 60              |
| 49 . . . . .      | Meridian scanning photometers at 5577 Å,<br>4278 Å, 6300 Å, and HB, for the time period<br>T+357 seconds through T+405 seconds . . . . . | 61              |
| 50 . . . . .      | All-sky TV frames at eight-second intervals<br>from T+409 seconds through T+449 seconds. . . . .   | 62              |
| 51 . . . . .      | Meridian scanning photometers at 5577 Å,<br>4278 Å, 6300 Å, and HB, for the time period<br>T+405 seconds through T+453 seconds . . . . . | 63              |
| 52 . . . . .      | All-sky TV frames at eight-second intervals<br>from T+457 seconds through T+497 seconds. . . . .   | 64              |
| 53 . . . . .      | Meridian scanning photometers at 5577 Å,<br>4278 Å, 6300 Å, and HB, for the time period<br>T+453 seconds through T+501 seconds . . . . . | 65              |
| 54 . . . . .      | All-sky TV frames at eight-second intervals<br>from T+505 seconds through T+545 seconds. . . . .   | 66              |
| 55 . . . . .      | Meridian scanning photometers at 5577 Å,<br>4278 Å, 6300 Å, and HB, for the time period<br>T+501 seconds through T+549 seconds . . . . . | 67              |
| 56 . . . . .      | All-sky TV frames at eight-second intervals<br>from T+553 seconds through T+569 seconds. . . . .   | 68              |

LIST OF ILLUSTRATIONS (Cont.)

| <u>Figure No.</u> | <u>Title</u>   | <u>Page No.</u> |
|-------------------|--|-----------------|
| 57 . . . . .      | Meridian scanning photometers at 5577 Å, 4278 Å, 6300 Å, and HB, for the time period T+549 seconds through T+573 seconds . . . . . | 69              |
| 58 . . . . .      | Time history of emission intensity at 82°, the point of rocket entry at 100 km, for 5577 Å, 6300 Å, and 4278 Å. . . . .            | 70              |
| 59 . . . . .      | Time history of emission intensity at 103°, the magnetic zenith, for 5577 Å, 6300 Å, and 4278 Å. . . . .                           | 71              |
| A-1 . . . . .     | Atomic oxygen detector - lamp and preregulator schematic diagram . . . . .   | 75              |
| A-2 . . . . .     | Atomic oxygen detector - detector schematic diagram . . . . .  | 76              |
| A-3 . . . . .     | Atomic oxygen detector - counting logic schematic diagram . . . . .  | 77              |
| A-4 . . . . .     | Atomic oxygen detector - timing logic schematic diagram . . . . .  | 78              |
| A-5 . . . . .     | Atomic oxygen detector - output electronics schematic diagram . . . . .  | 79              |
| B-1 . . . . .     | Energy deposition scintillator - schematic diagram. . .  | 83              |
| B-2 . . . . .     | Energy deposition scintillator - input power density vs. output voltage calibration. . . . .                                       | 84              |
| C-1 . . . . .     | Photometer - schematic diagram. . . . .  | 88              |
| C-2 . . . . .     | Photometer - high voltage monitor calibration curve . .  | 89              |
| C-3 . . . . .     | Light transmission characteristics for flexible fiber optics in the photometers . . . . .  | 89              |
| C-4 . . . . .     | Photometer PM2-96 field of view . . . . .  | 90              |
| C-5 . . . . .     | Photometer PM2-96 filter transmission . . . . .  | 91              |
| C-6 . . . . .     | Photometer PM2-96 output voltage vs. photon sterance calibration . . . . .   | 91              |
| C-7 . . . . .     | Photometer PM2-99B field of view. . . . .  | 92              |
| C-8 . . . . .     | Photometer PM2-99B filter transmission. . . . .  | 92              |

LIST OF ILLUSTRATIONS (Continued)

| <u>Figure No.</u> | <u>Title</u>  | <u>Page No.</u> |
|-------------------|---|-----------------|
| C-9 . . . . .     | Photometer PM2-99B output voltage vs.<br>photon sterance calibration . . . . .  | 93              |
| C-10 . . . . .    | Photometer PM2-107B field of view . . . . .                                     | 93              |
| C-11 . . . . .    | Photometer PM2-107B filter transmission . . . . .                               | 94              |
| C-12 . . . . .    | Photometer PM2-107B output voltage vs.<br>photon sterance calibration . . . . . | 94              |

## LIST OF TABLES

| <u>Table No.</u> | <u>Title</u>  | <u>Page No.</u> |
|------------------|---|-----------------|
| 1 . . . . .      | Sergeant A30.276 Payload Instrumentation . . . . .        | 5               |
| 2 . . . . .      | Sergeant A30.276 Timer Settings . . . . .                 | 7               |
| 3 . . . . .      | Summary of Ground Based Support Instrumentation . . . . . | 20              |
| C-1 . . . . .    | High Voltage Monitor Values for A30.276 Photometers. . .  | 87              |

This page intentionally left blank.

## INTRODUCTION

On 13 April 1983, experimenters from Utah State University and Air Force Geophysics Laboratory launched a Sergeant rocket (A30.276) from the Poker Flat Research Range, Alaska, into an IBC Class II aurora. The purpose of the flight was to obtain high resolution spectral measurements of atmospheric infrared radiation during the auroral event and to provide supporting measurements that would assist in characterizing and documenting the event.

This volume presents a summary of the supporting instrumentation aboard the A30.276 vehicle and the data obtained from those sources. Additionally, instrumentation at the ground monitoring stations provided data worthwhile in documenting and characterizing the auroral event. We present that data here also.

To set this information in context, some information on the rocket configuration is necessary and although in some aspects this may be redundant to that presented in previous reports, we include it in the present report for the sake of continuity.

Since the Rocket-borne Field Widened Interferometer and the data from that source is thoroughly reported in other documents, we present minimal information here on that instrument.

**This page intentionally left blank.**

## FLIGHT SUMMARY

The launch of Sergeant A30.276 occurred at 0906:23 (GMT) on 13 April 1983, from the Poker Flat Research Range, Alaska. The payload achieved an apogee of 139.25 km. An on-board parachute provided the means for successful post-flight recovery of the instrumented payload. Figure 1 is a trajectory plot for the flight.

### Auroral Conditions at Launch and During Flight

Prior to the launch of Sergeant A30.276, an auroral arc system moved to the south of the launch site. Final stages of launch countdown commenced as the aurora brightened and began moving back to the north. Decision to launch came as the aurora brightened to 60-80 kR of green line (5577 Å) and the brightest forms moved toward the elevation required for rocket penetration. Aurora of about 40 kR or greater intensity, filled the region within approximately  $\pm 30^\circ$  of zenith. At launch, auroral movement appeared to stop, and the brightest regions remained south of the zenith. The region penetrated by the rocket dimmed to about 15 kR (5577 Å) by the time of penetration. On rocket descent the aurora penetrated by the rocket was about 4 kR. Therefore, the rocket instrumentation measured in regions where the prompt effects were only moderately bright, but which had been predosed by significant electron input.

### Flight Parameters

All door, cover, and nose tip ejections occurred during the flight as programmed. The side door was ejected at approximately T+68 seconds. The nose tip ejected at 75.5 seconds (84 km) exposing the forward looking instruments. All instruments aboard the payload functioned throughout the flight.

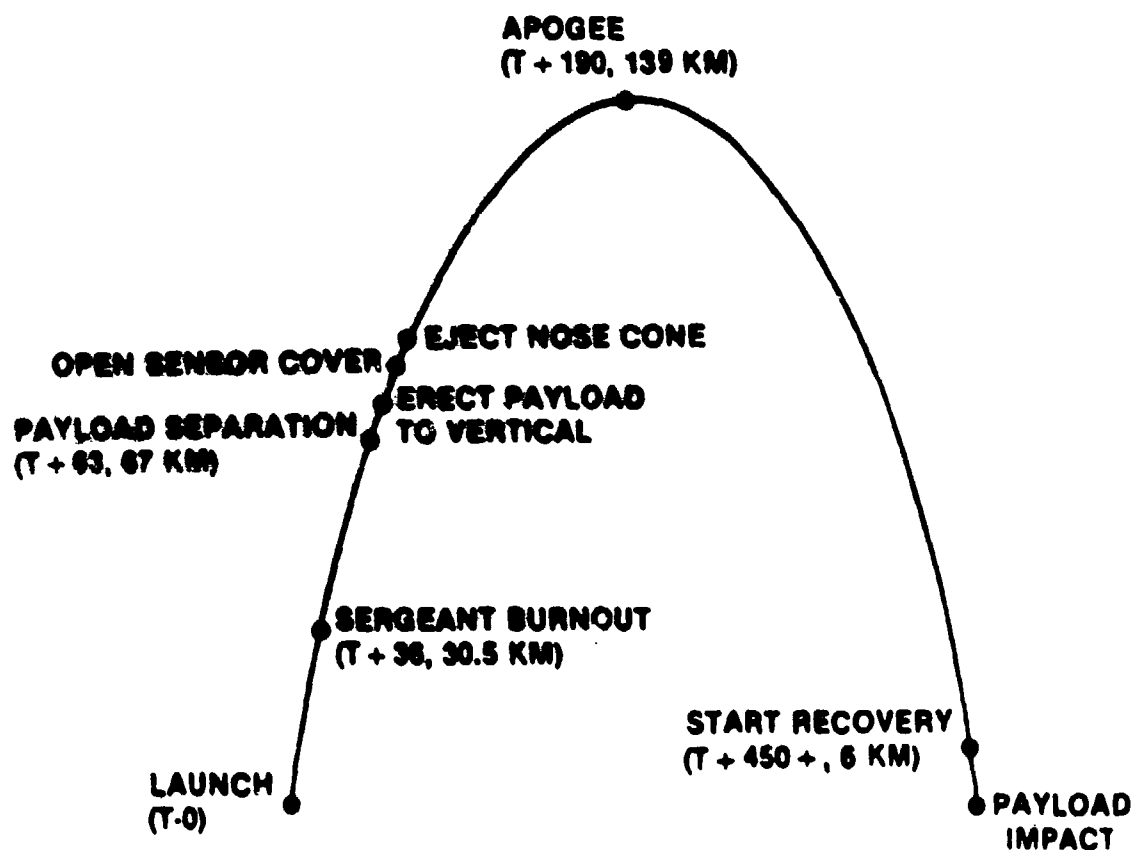


Figure 1. Flight profile for Sergeant A30.276 with payload functions shown.

## INSTRUMENTATION

The instrumentation involved in the application of payload A30.276 falls basically into two categories, i.e., 1.) those instruments for flight measurements, and 2.) those for ground based measurements.

### Flight Instrumentation

The payload of A30.276 contained both prime and secondary (supporting) instrumentation. Table 1 gives an overview of the instrumentation aboard the payload and defines the role played by each instrument. Figure 2 shows the relative location of the instruments in the payload.

TABLE 1.  
Sergeant A30.276 Payload Instrumentation

| Instrument/Serial No.   | Function   |
|---|--|
| Field-Widened Interferometer<br>FWI-2-1<br>(Prime Instrumentation)  | Measurements of spectral emission of the atmosphere in the 2 - 7.5 $\mu$ m range |
| Atomic Oxygen Detector<br>ATOX 83-1<br>(Secondary Instrumentation)  | Altitude profile of atomic oxygen concentration                                  |
| 3914 Å Photometers (4)<br>PM2-89B (Photometer #2)<br>PM2-96 (Photometer #3)<br>PM2-99B (Photometer #4)<br>PM2-107B (Photometer #1)<br>(Secondary Instrumentation) | Measurements of auroral intensity in 4 quadrants of interferometer FOV           |
| Energy Deposition Scintillator<br>EDS 75-7<br>(Secondary Instrumentation)   | Measurements of energy >3 KeV carried by electrons                               |

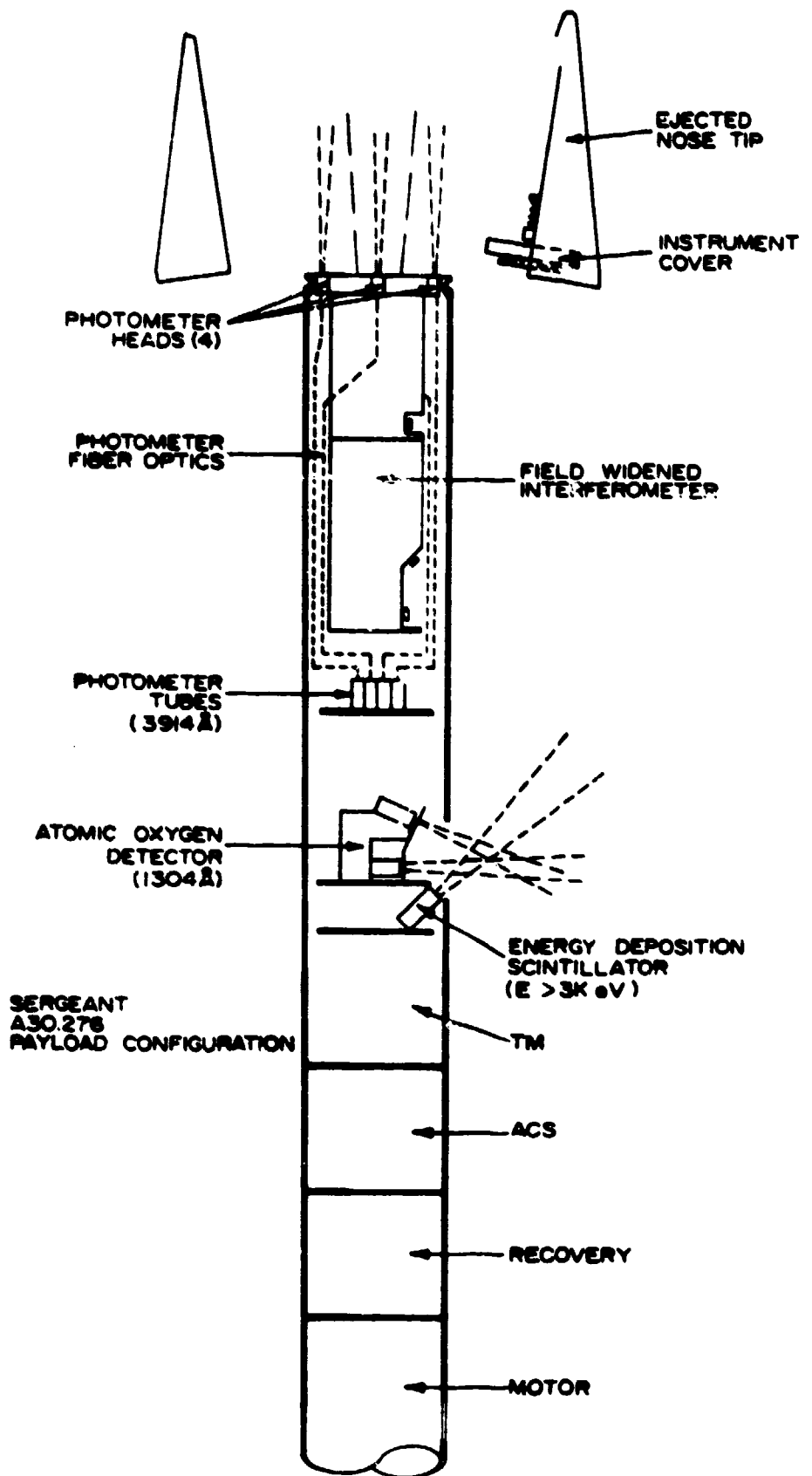


Figure 2. Sergeant A30.276 payload configuration.

Several mechanical and electrical functions are necessary to configure the payload for the measurements phase of the flight subsequent to motor burnout. Redundant, mechanical, G-activated timers close switches to accomplish these functions, thereby initiating the pyrotechnics for nosetip and doors ejection, and applying high voltage where necessary. Table 2 shows the primary and secondary timer settings. Figure 1 shows the occurrence of events initiated by the timers compared to the payload trajectory.

TABLE 2  
Sergeant A30.276 Timer Settings

| Setting   | Timer #1<br>Function  | Setting   | Timer #2<br>Function  |
|-----------|---|-----------|---|
| 33.6 sec. | Drive Control   | 33.1 sec. | Drive Control   |
| 45.5 sec. | Shutter Open  | 45.5 sec. | Shutter Open  |
| 46.6 sec. | Atomic Oxygen Valve**   | 46.3 sec. | Atomic Oxygen Valve**   |
| 53.2 sec. | Cal. Diode  | 77.4 sec. | Cal. Diode  |
| 68.6 sec. | Atomic Oxygen & Energy<br>Deposition Scintillator<br>Door Eject** | 68.1 sec. | Atomic Oxygen & Energy<br>Deposition Scintillator<br>Door Eject** |
| 73.1 sec. | Pop Cover Eject*  | 73.0 sec. | Pop Cover Eject*  |
| 75.5 sec. | Nosetip Eject*  | 76.0 sec. | Nosetip Eject*  |

\* Pyrotechnic bellows actuators

\*\* Pyrotechnic guillotines

#### Field-Widened Interferometer

The field-widened interferometer was the prime measuring instrument aboard the payload of Sergeant A30.276. The instrument and data from that source has been thoroughly discussed in an earlier report; refer to that source for further documentation.

### Atomic Oxygen Detector

The Atomic Oxygen Detector provides a measurement profile of the column density of atomic oxygen during the payload flight. The detector provides data on the concentration of atomic oxygen by measuring the intensity of OI 1304 Å EUV radiation that is resonantly scattered from the ambient atomic oxygen. The source of the radiation is an RF-excited oxygen resonance lamp which provides a collimated, modulated beam that impinges on the atmosphere. A portion of the beam is resonantly scattered by the ambient atomic oxygen into a photon detector. The effective cross section for resonant scattering of the 1304 Å radiation is large ( $\sim 3.4 \times 10^{-14} \text{ cm}^2$ ), thereby providing a generous return signal. This large signal return is important for elimination of the effects of background light from atmospheric Rayleigh scattering, from airglow and auroral emissions, and from extraterrestrial sources. Additional background rejection is achieved by square wave modulation of the light source so that the background (light source off) is also measured for subtraction from the signal plus background (light source on). Figure 3 is a block diagram. Appendix A contains schematic diagrams and other information pertinent to the Atomic Oxygen Detector.

The data reduction process obtains profiles of atomic oxygen from count rate profiles through computer modeling of the resonant scattering process and instrument calibration. This effectively gives the product of the lamp intensity and the detector quantum efficiency. Computer modeling of the scattering process includes a careful evaluation of the lamp as a source of photons into all regions common to both the baffled lamp field of view and the detector acceptance field of view. Modelers treat each line of the resonance triplet separately and consider all effects such as partial occlusion of the

lamp by finite-size baffles and the cylindrical nature of the discharge itself.

Essentially, the data reduction process creates a three dimensional model of glowing atomic oxygen that becomes the source of radiation for the detector acceptance field of view. The process also carefully defines the detector field of view in a manner similar to that used for the lamp. We also consider attenuation between the incremental scattering volume and the detector as well as doing a relatively crude estimation of multiple scattering effects which are important at high oxygen densities. Figure 4 is the data obtained from the atomic oxygen detector during the flight of A30.276. The reader should note that the profiles portrayed in Figure 4 do not extend to payload apogee. Extensive scattering of data above the altitudes shown make retrieval of meaningful information in those realms unfeasible. Because the profiles do not extend to apogee, there is a significant difference in time and space between the tops of the ascent and descent profiles. These temporal and spatial differences create the discontinuity in density values at the tops of the two profiles.

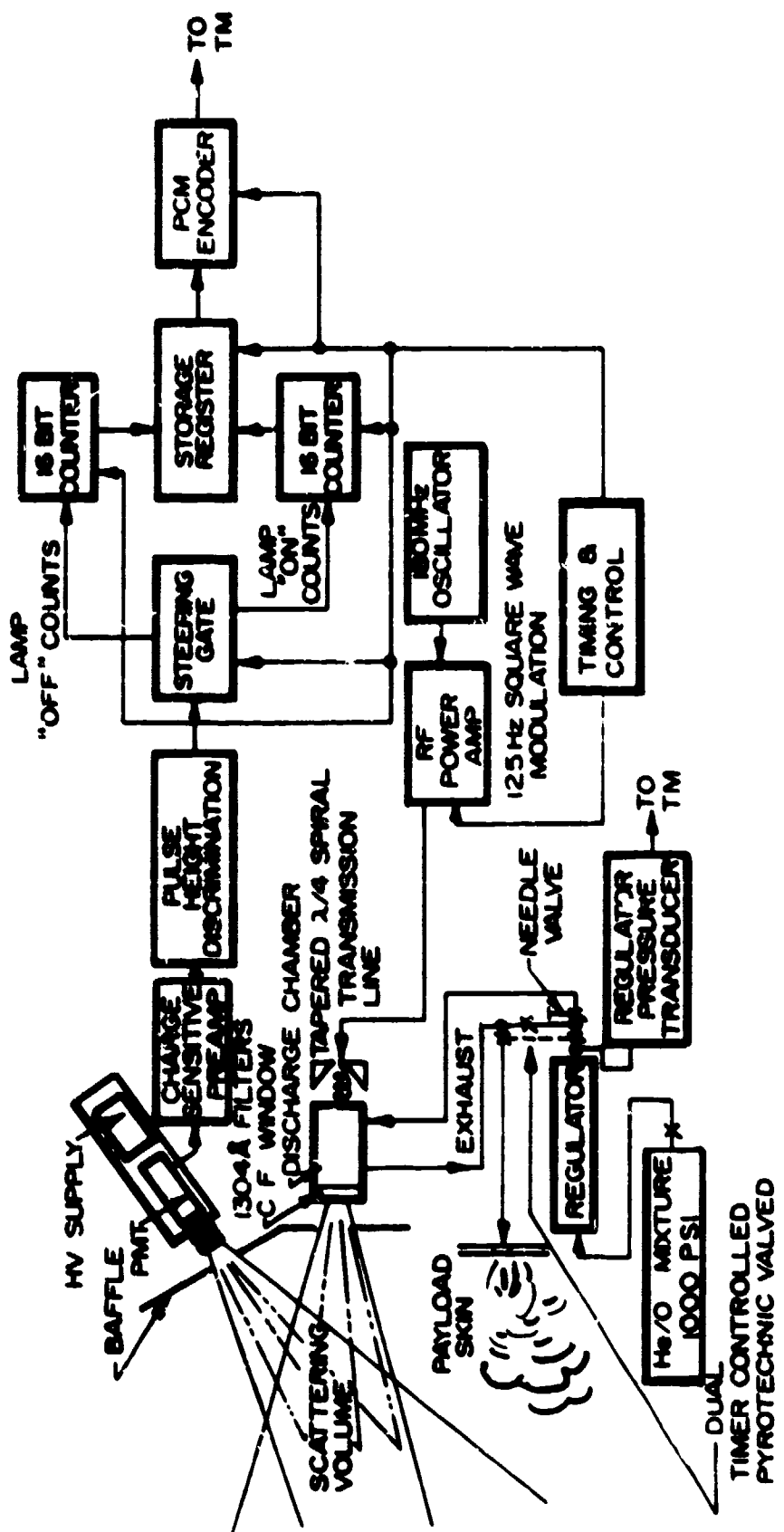


Figure 3. A block diagram of the Atomic Oxygen Detector aboard the payload of Sergeant A30.276.

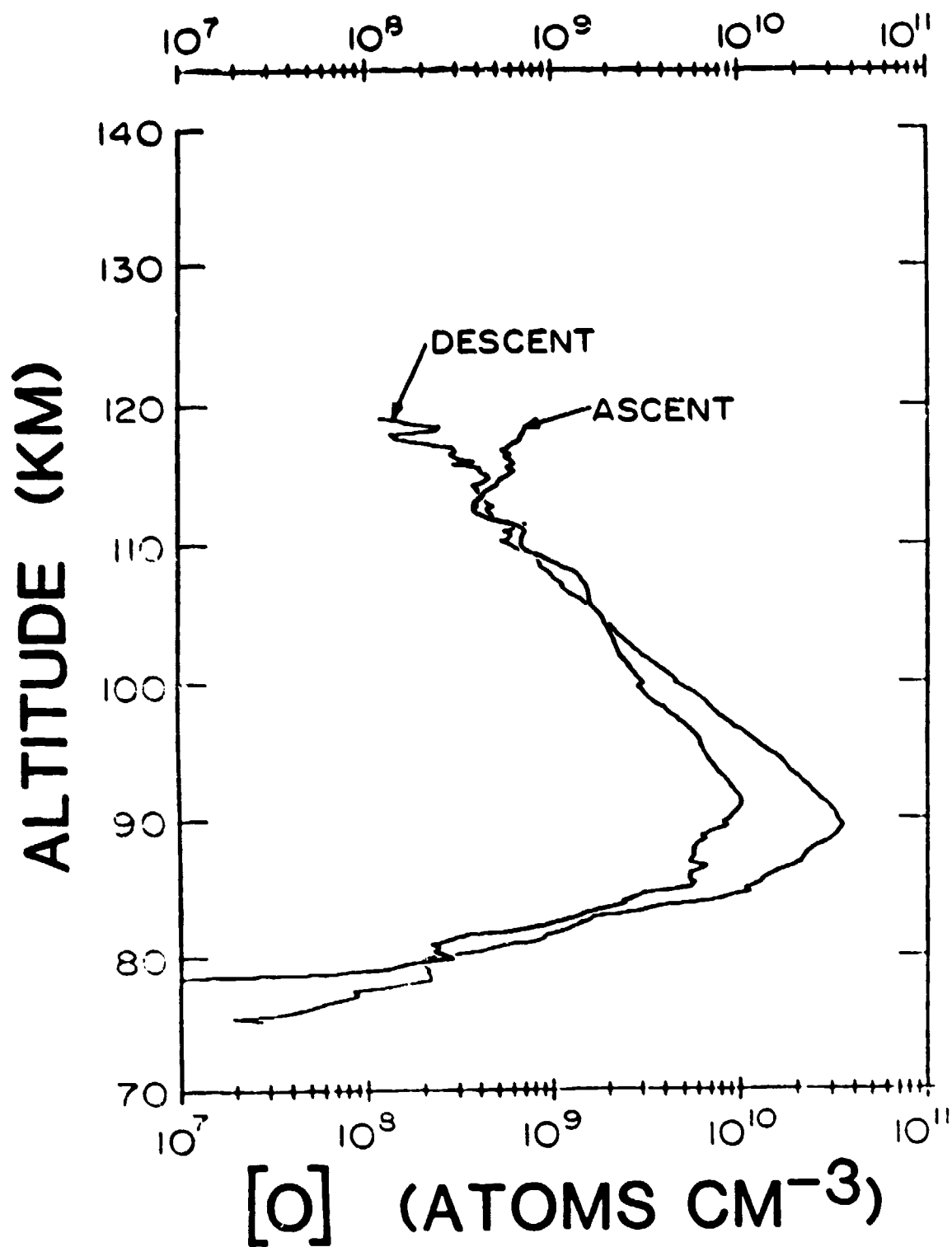


Figure 4. Atomic oxygen density profiles measured during the flight of Sergeant A30.276.

### Energy Deposition Scintillator

The energy deposition scintillator provides measurements of the total power density carried by energetic electrons and protons in the earth's atmosphere. Figure 5 is a block diagram of the energy deposition scintillator. Appendix B contains schematic diagrams of the instrument.

The instrument basically consists of a scintillation phosphor viewed by a photomultiplier tube. The output of the photomultiplier is amplified by four cascaded saturating amplifiers and consists of the summation of the outputs of these amplifiers to provide data compression which can be described over four ranges by linear mathematical functions. This output is a measurement of the rate of energy input due to particles having energies above a predetermined threshold, which is determined by a thin aluminized window placed in front of the scintillation phosphor, and for this application was  $\geq 6.7$  keV for electrons and  $\geq 50$  keV for protons. Additionally, the aluminized window serves to prevent ambient light from directly entering the phototube. The maximum energy which can be measured by the instrument is contingent upon the type and thickness of the scintillation phosphor. For this application, the scintillation phosphor is a pilot B plastic scintillation phosphor, 0.035" thick which imposes a maximum energy measurement capability of 200 keV for electrons and 26 MeV for protons.

The energy deposition scintillator has two monitor circuits for checks of the operation of the instrument. A calibration lamp illuminates the phototube approximately once each 30 seconds for approximately 0.1 second. This provides an output pulse twice each minute and serves to provide a functional check for the instrument. For EDS 75-7 the output with the calibration lamp on, was  $\geq 2.6$  volts. The energy deposition scintillator includes a high voltage monitor to check the operation of the high voltage power supply.

The output voltage from the instrument's high voltage monitor when it was calibrated was 2.64 volts.

The EDS field of view is inclined 45° forward from normal to the vehicle major axis as shown in Figure 2. The instrument has a geometric factor of 0.109 cm<sup>2</sup> ster.

Figure 6 (a & b) shows the power density profiles from the measurements made during the flight of A30.276. While examining these profiles the reader should bear in mind that the uppermost portions do not represent the same point in space and time. We have omitted data between T+170 sec. and T+205 seconds ( $\pm$  apogee) since little change in altitude occurred during that time.

Figure B-2 is the calibration curve which equates output voltage to input power density in ergs cm<sup>-2</sup> sec<sup>-1</sup> ster<sup>-1</sup>.

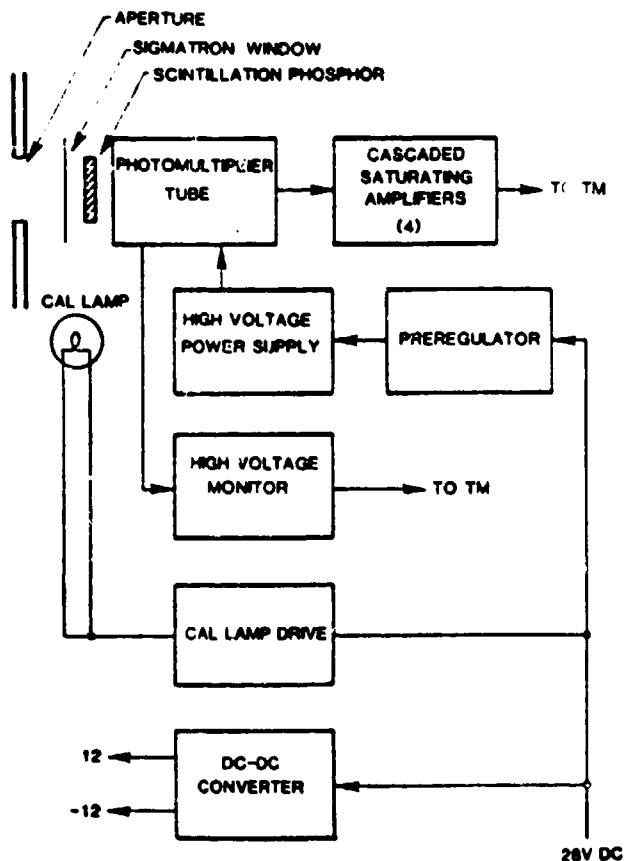


Figure 5. A block diagram of the Energy Deposition Scintillator.

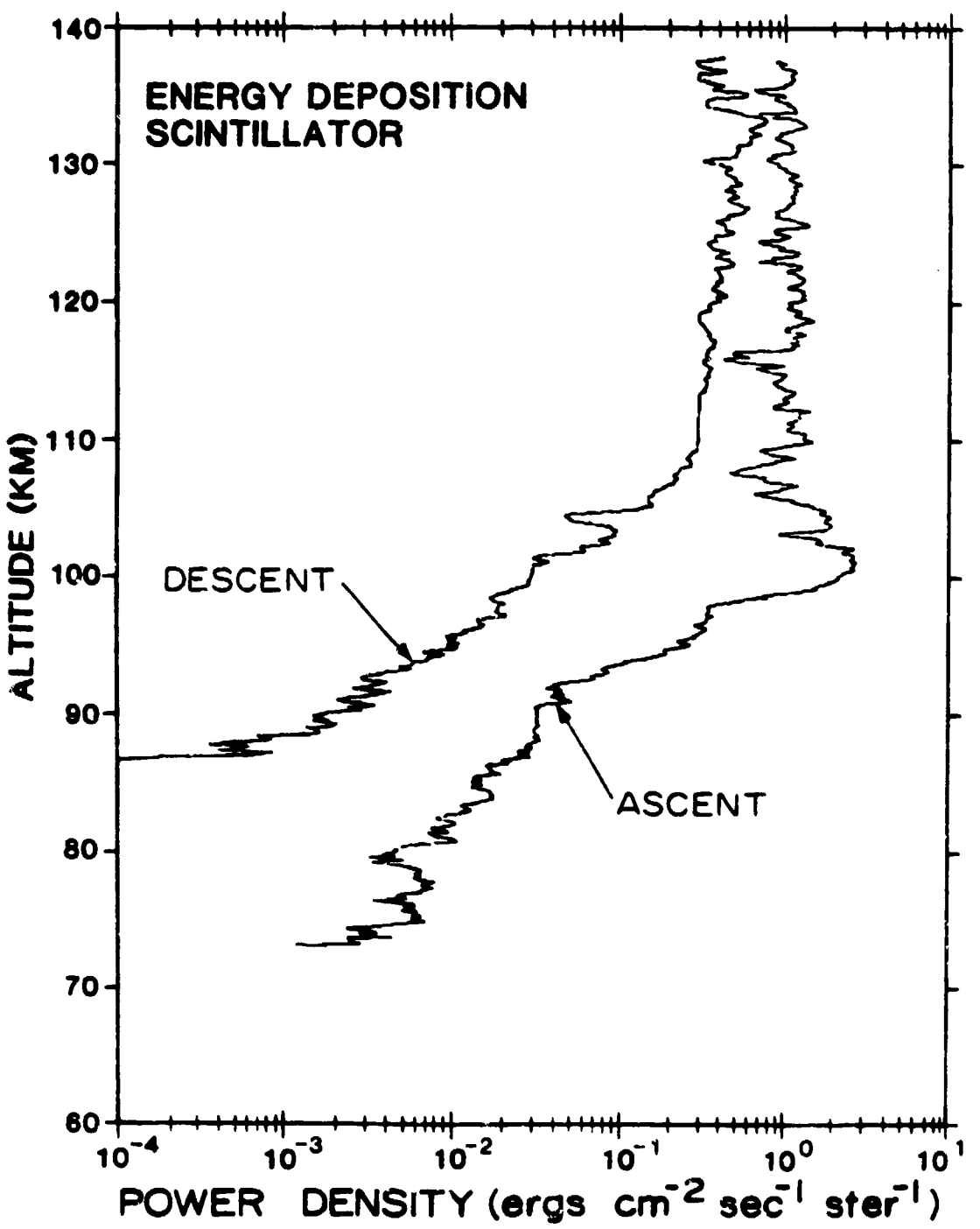


Figure 6. Power density carried by auroral electrons and protons, measured by the EDS during the ascent and descent portions of the flight of A30.276.

### Photometers

The payload of Sergeant A30.276 included four 3914 Å photometers as secondary instrumentation to support the measurements from the field-widened interferometer. These instruments measured the intensity of the ultraviolet emissions from the  $N_2^+$  first negative band system at 3914 Å, thus allowing the creation of an intensity vs. altitude profile.

The photometers were forward viewing devices, each having approximately a 5.5° field of view. Careful alignment of the fields of view of the four instruments provided coverage (in four quadrants) of the same field viewed by the interferometer. The photometer photomultiplier tubes and amplifiers, (located behind the interferometer) received their input energy through light pipes with collecting heads located at the front end of the payload. Figure 2 illustrates this concept diagrammatically. Figure 7 is a block diagram of the photometers. Only one photometer is shown in the diagram, but the rocket payload included four identical units.

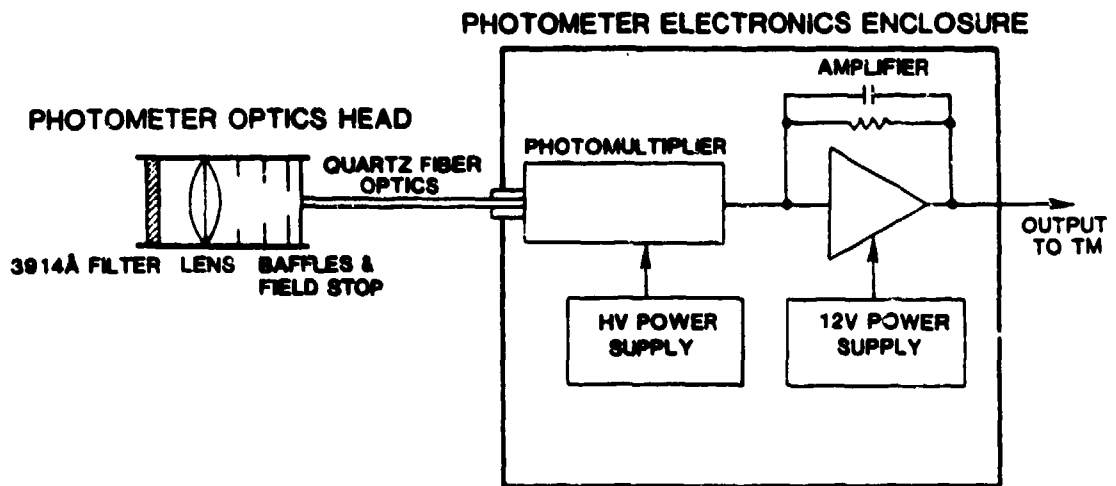


Figure 7. Block diagram of the 3914-Å photometers.

Our design of the mountings for the photometers placed the four units at  $0^\circ$ ,  $90^\circ$ ,  $180^\circ$ , and  $270^\circ$  around the interferometer front end (launch lug at  $0^\circ$ , viewing aft) and tipped the forward end of each unit's optical axis  $3^\circ$  in the CW direction as illustrated in Figure 8a. Thus, the photometers covered essentially the same field of view as the interferometer, as illustrated in Figure 8b, which assumes a vantage point looking back at the rocket from infinity.

Figure 9 contains the emission intensity profiles measured by the photometers during flight. We have not included the ascent intensity profile for photometer 2 (PM2-89B). The data from that photometer were offset (higher) due to a missing aperture stop in that photometer's optical section. The missing stop allowed the instrument to view a larger field and hence, the higher output. We did not recalibrate the photometer to account for the missing stop since the data did not appear to differ significantly in that quadrant from those in the other 3 quadrants.

We note the increase of  $3914 \text{ \AA}$  radiation during rocket ascent beginning at about 130 km and continuing beyond apogee (139.25 km) to about 135 km during descent. Clearly, down to 110 km the descent values are higher than ascent values by amounts ranging from a maximum of 1.5 kR at 135 km, to equal values at about 110 km. We feel this is not due to instrumental effects because it appears on all photometers. We do not have enough supportive data however, to say whether or not this is an effect of temporal/spatial changes in the deposition spectrum at low energies. Examination of the energy deposition scintillator data in Figure 6 shows that temporally (and hence spatially), the deposition through the altitude regime noted above, was continuously decreasing in contrast to the photometer data. However, the energy deposition scintillator measures only those electrons with energies

PHOTOMETER LOCATIONS  
VIEWING AFT

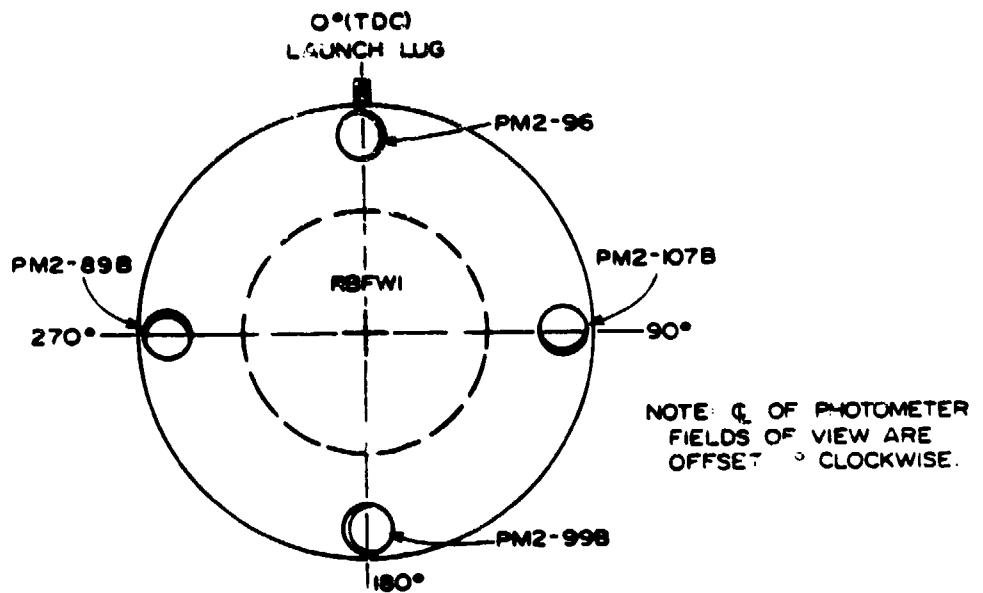


Figure 8a. Locations of the four photometers relative to the vehicle launch lug. The forward end of each photometer's optical axis was inclined  $3^\circ$  clockwise as viewed looking aft to provide coverage, in four quadrants, of the field viewed by the interferometer.

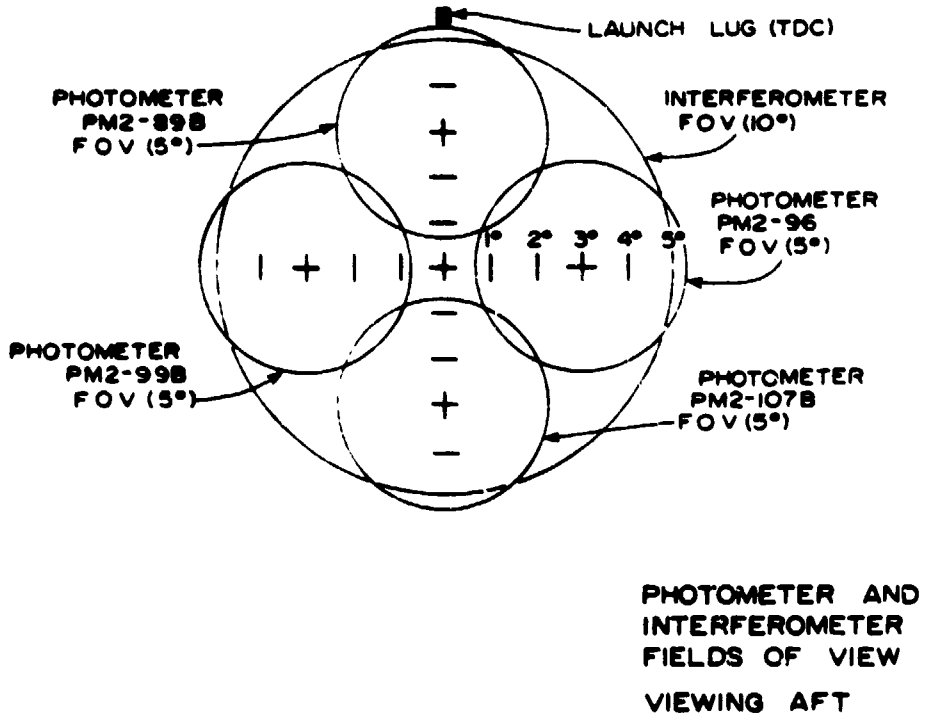


Figure 8b. Relationship of the photometer fields of view to the field of view of the interferometer. The drawing assumes the viewer's vantage point is at infinity looking back at the rocket.

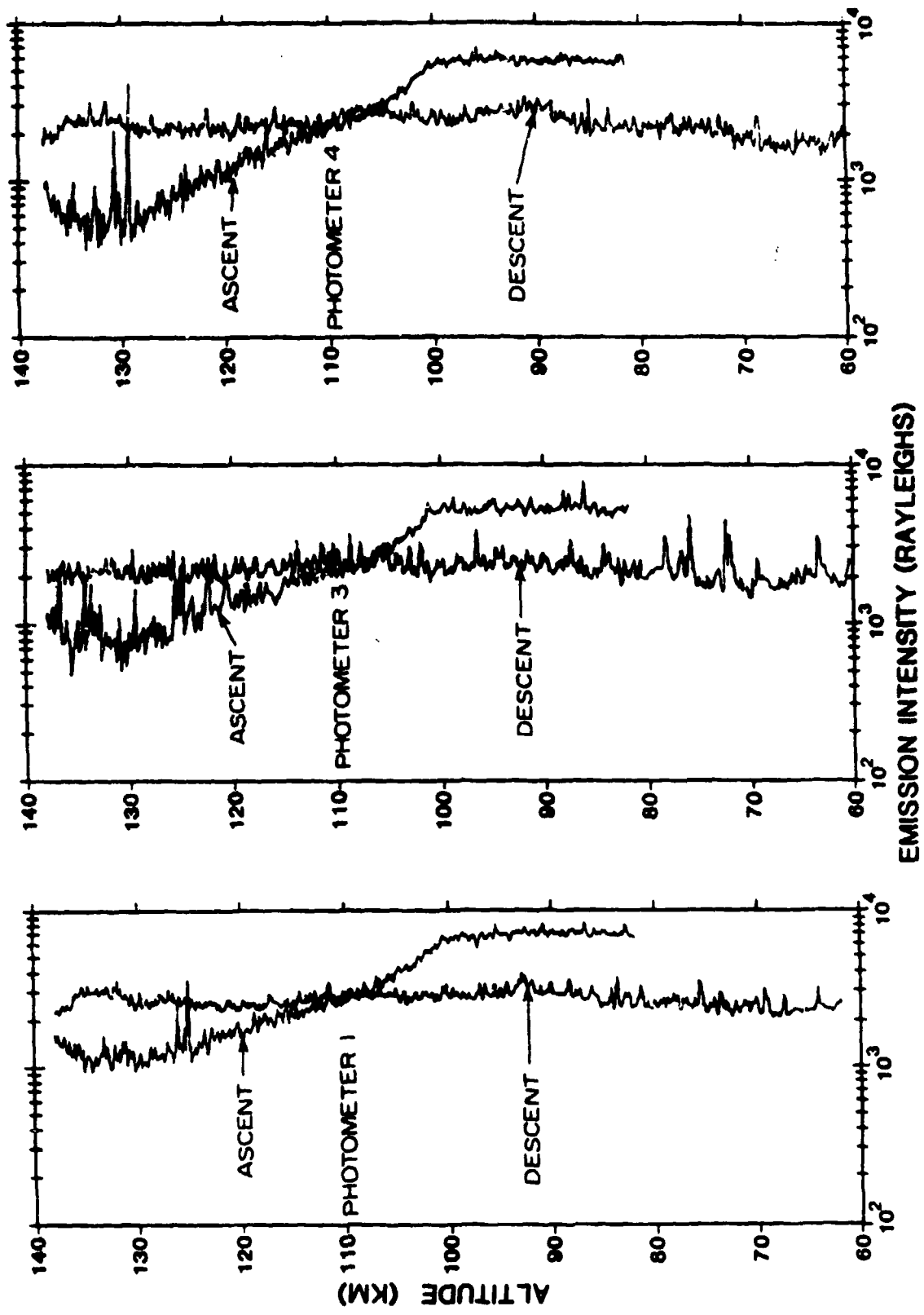


Figure 9. Emission intensity vs. altitude profile at 3914 Å as measured by photometers no. 1, 3, and 4 (PM2-107B, PM2-96, and PM2-99B, respectively).

>7 keV and therefore, these data are not a measure of softer electrons being deposited at or above the rocket's peak altitudes. It is possible that the energy spectrum of energetic particles impinging upon the atmosphere had shifted to a lower value during this time period, and electron deposition was occurring at higher altitudes than those reached by the rocket. If this were the case we would expect an increase in photometer output and a decrease in energy deposition as measured by the energy deposition scintillator.

Appendix C contains schematic diagrams and calibrations for the 3914 Å photometers.

#### Ground Based Support Instrumentation

A complement of ground based instrumentation was operational at Poker Flat and Ft. Yukon to support the flight of Sergeant A30.276. Scientists at the launch site used the output data from these instruments to determine when geophysical conditions met the criteria for launch of the payload. The recorded data from these sources may also help describe and characterize the auroral event into which Sergeant A30.276 flew.

We have not included the data from riometers or magnetometers in this report, but that information is available from the Geophysical Institute, University of Alaska if required for data analysis. We have included here the data from all-sky television and meridian scanning photometers as these more directly describe the auroral conditions during the flight of A30.276.

Figures 10 through 57 contain these data.

Table 3 is a summary of the ground based instrumentation and locations.

Figures 10 through 57 detail the history of the auroral event for the period from T-987 seconds to T+573 seconds. Some notes regarding these Figures are necessary to aid in their interpretation. The meridian scanning

TABLE 3  
Summary of Ground Based Support Instrumentation  
for the Flight of Sergeant A30.276

| Site                      | Instrument   | Measurement   |
|---------------------------|--|---|
| Poker Flat                | All-sky TV Monitor   | Auroral Forms                                       |
| Poker Flat                | Meridian Scanning Photometers<br>at 5577 Å, 4278 Å, 6300 Å<br>and 4861 Å (H <sub>B</sub> ) | Auroral emission<br>intensity, magnetic<br>meridian |
| Poker Flat &<br>Ft. Yukon | Magnetometer   | Magnetic field -<br>3 components                    |
| Poker Flat &<br>Ft. Yukon | Riometer   | Relative ionospheric<br>opacity                     |

We wish to gratefully acknowledge the efforts of personnel at the Geophysical Institute, University of Alaska, for their assistance in providing the ground based measurements.

photometers scan the sky from magnetic north (0°), along the meridian through the zenith to magnetic south (180°) at the rate of one scan per 8 seconds. All of the meridian scans for the period indicated above are reproduced here. They are formatted to include six scans of each of the four colors (5577 Å, 4278 Å, 6300 Å, and H<sub>B</sub>) per page for ease in comparing the relative intensities.

The all-sky video has not been reproduced in its entirety. This data source provides a visual record at the rate of 30 frames per second. We selected frames that corresponded in time with the center of each meridian scan (one video frame per 8 seconds) from T-95 seconds to the end of the period noted above and portrayed them on the page opposite the corresponding meridian scans for easy comparison. We selected the appropriate all-sky frames from the video tape record by using a video monitor with good single frame capability. The frames were photographed and printed using consistent

exposure times, development times and temperatures to represent the video images as accurately as possible. It must be noted, however, that the video record is not an accurate reference for true auroral brightness. The TV camera has an automatic gain feature which reduces image intensity for bright scenes. This is evidenced in Figure 32 (T+9 and T+17) where the bright plume from the rocket has caused the TV camera to reduce its gain. The necessity to halftone screen the resulting prints for reproduction produces a slight moray pattern on some of the prints that lie in the mid-tone range. We point out that these patterns, which assume the form of a narrow banding, are artifacts of the reproduction technique and not auroral phenomena; they should be disregarded. Only  $\frac{1}{240}$  of the video record for the time period of concern has been reproduced here. The entire video record can be obtained, if necessary, from the Geophysical Institute, University of Alaska.

We derived Figures 58 and 59 from the meridian scanning photometer data by measuring the signal magnitude at  $82^\circ$  and  $103^\circ$ , the rocket entry point during ascent at 100 km, and the magnetic zenith, respectively, on each scan. These illustrations, therefore, show a time history of intensity at 5577 Å, 6300 Å, and 4278 Å, for these two important points. Time resolution is eight seconds in these plots.

# MERIDIAN SCANNING PHOTOMETERS

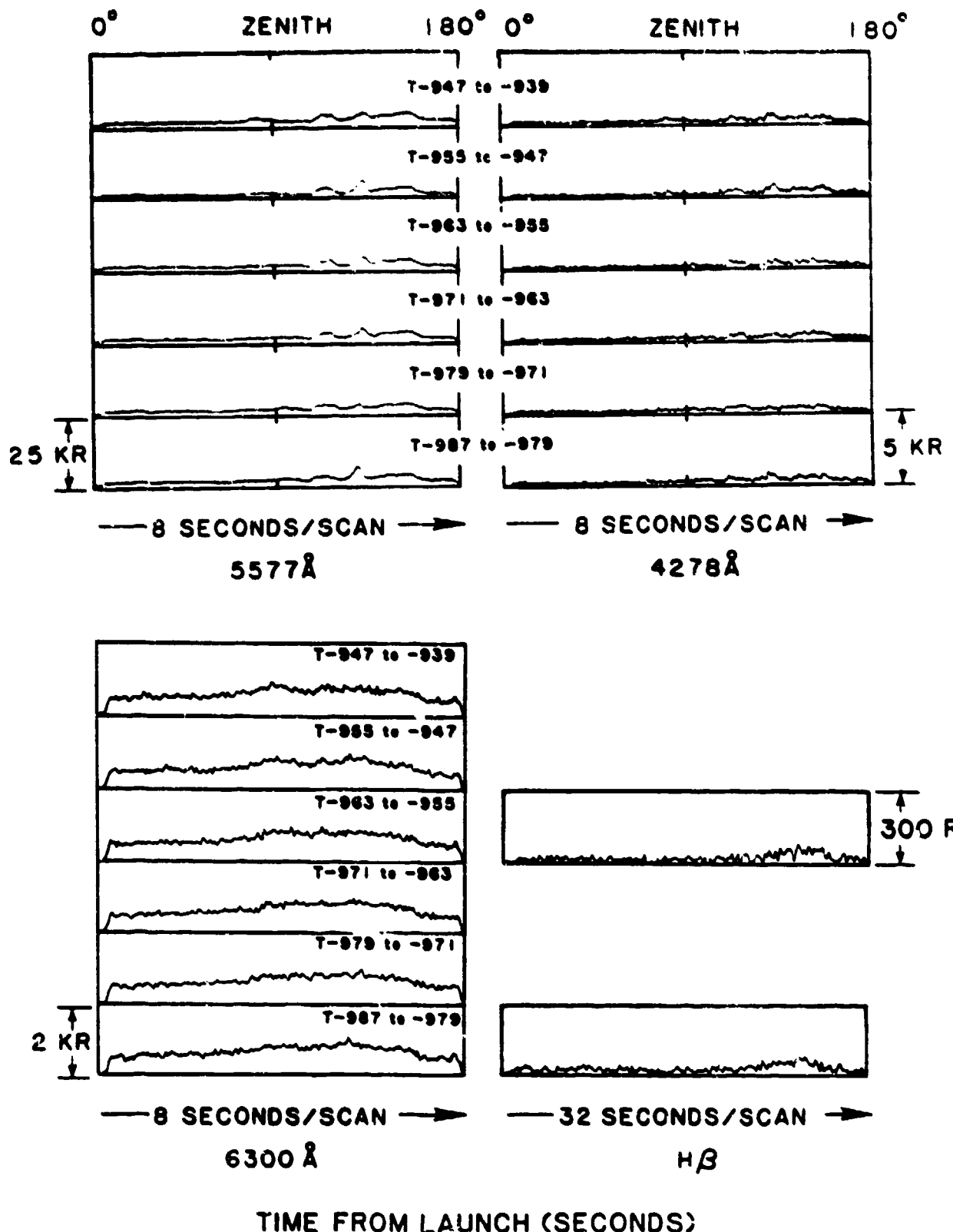


Figure 10. Meridian scanning photometers at 5577 Å, 4278 Å, 6300 Å, and H $\beta$ , for the time period T-979 seconds through T-939 seconds.

# MERIDIAN SCANNING PHOTOMETERS

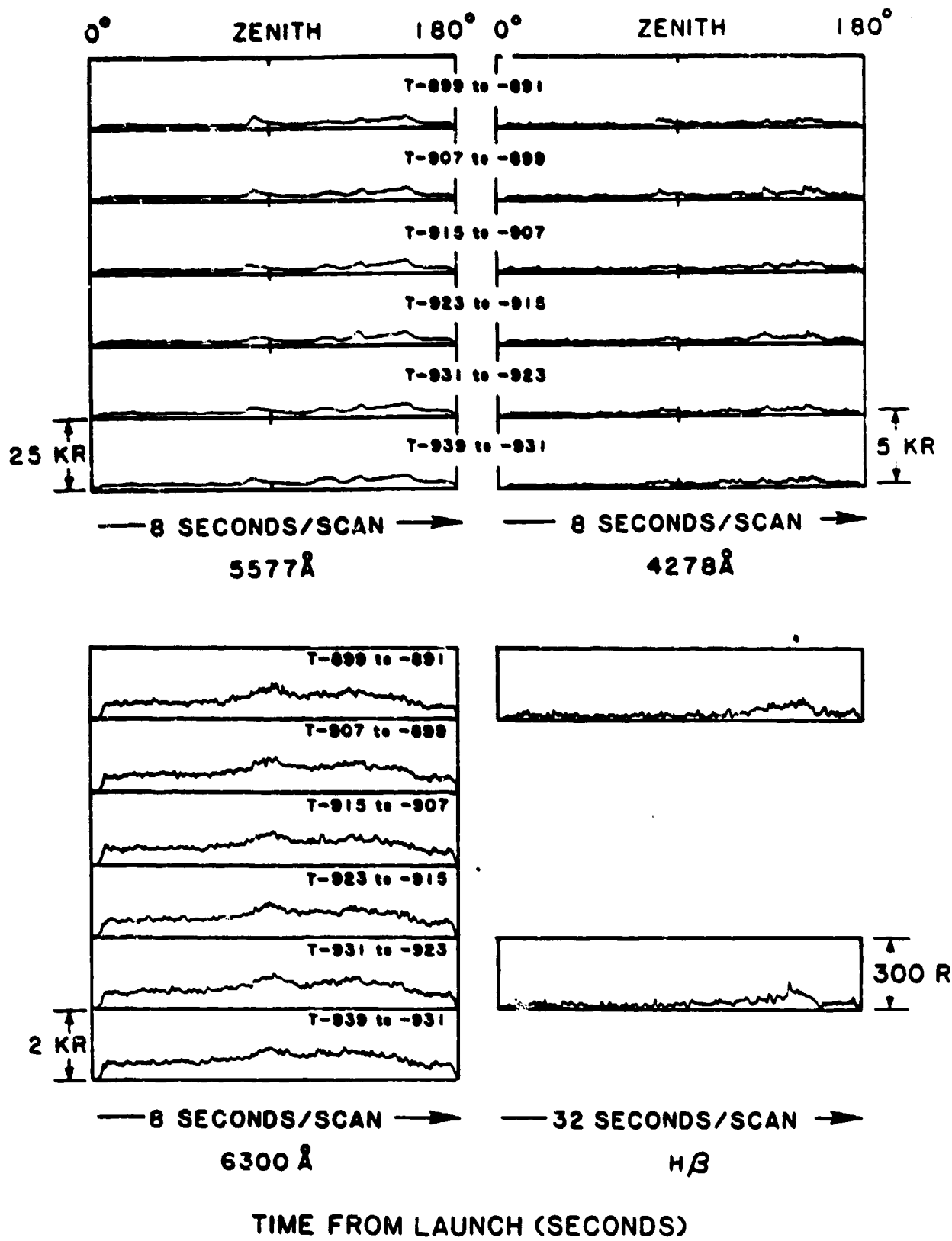


Figure 11. Meridian scanning photometers at 5577 Å, 4278 Å, 6300 Å, and H $\beta$ , for the time period T-939 seconds through T-891 seconds.

### MERIDIAN SCANNING PHOTOMETERS

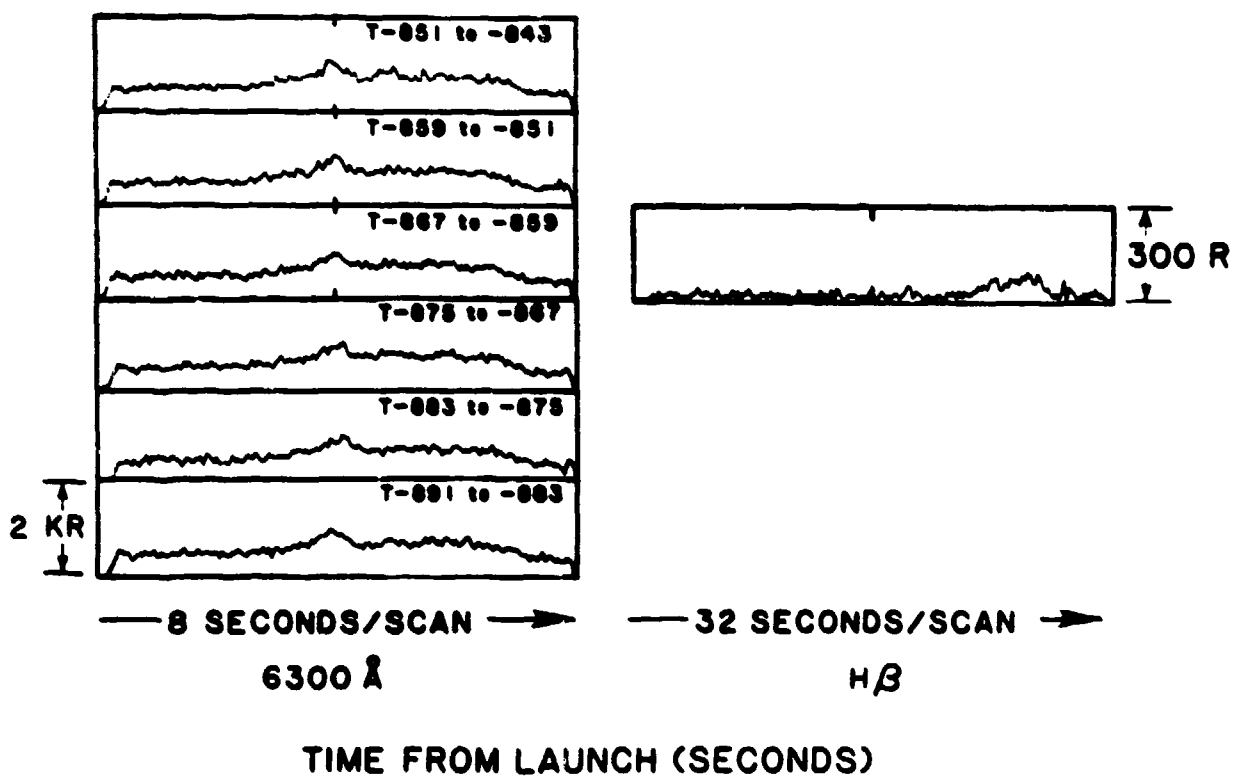
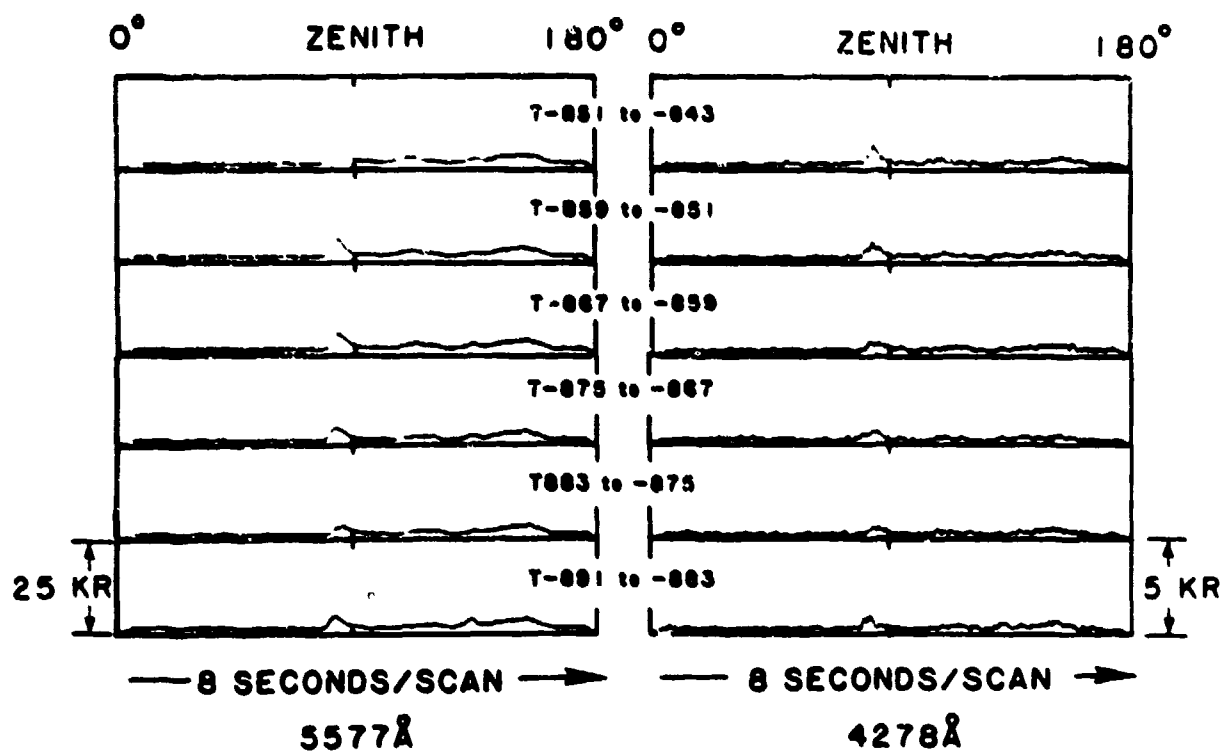


Figure 12. Meridian scanning photometers at 5577 Å, 4278 Å, 6300 Å, and H $\beta$ , for the time period T-891 seconds through T-843 seconds.

# MERIDIAN SCANNING PHOTOMETERS

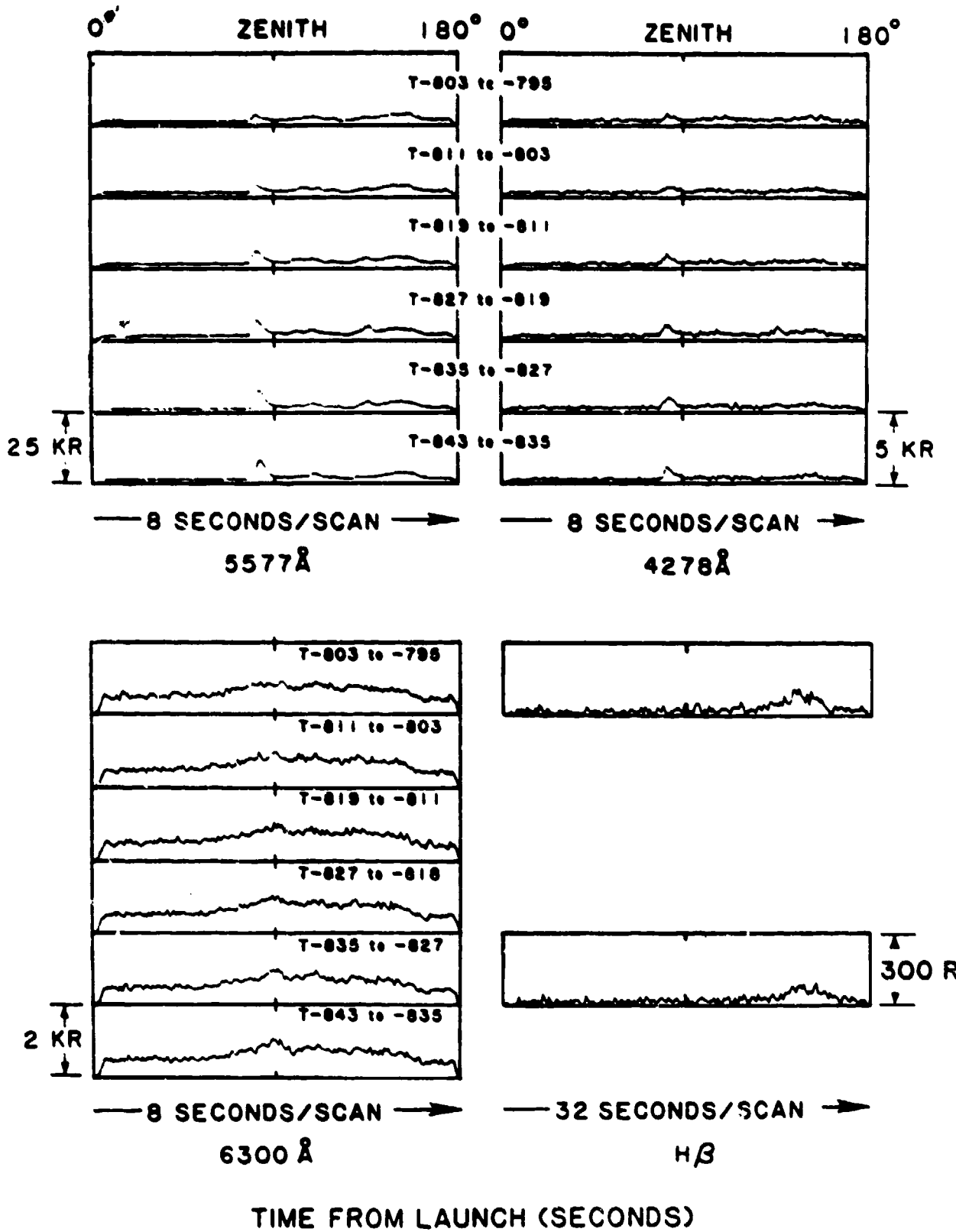


Figure 13. Meridian scanning photometers at 5577 Å, 4278 Å, 6300 Å, and H $\beta$ , for the time period T-843 seconds through T-795 seconds.

### MERIDIAN SCANNING PHOTOMETERS

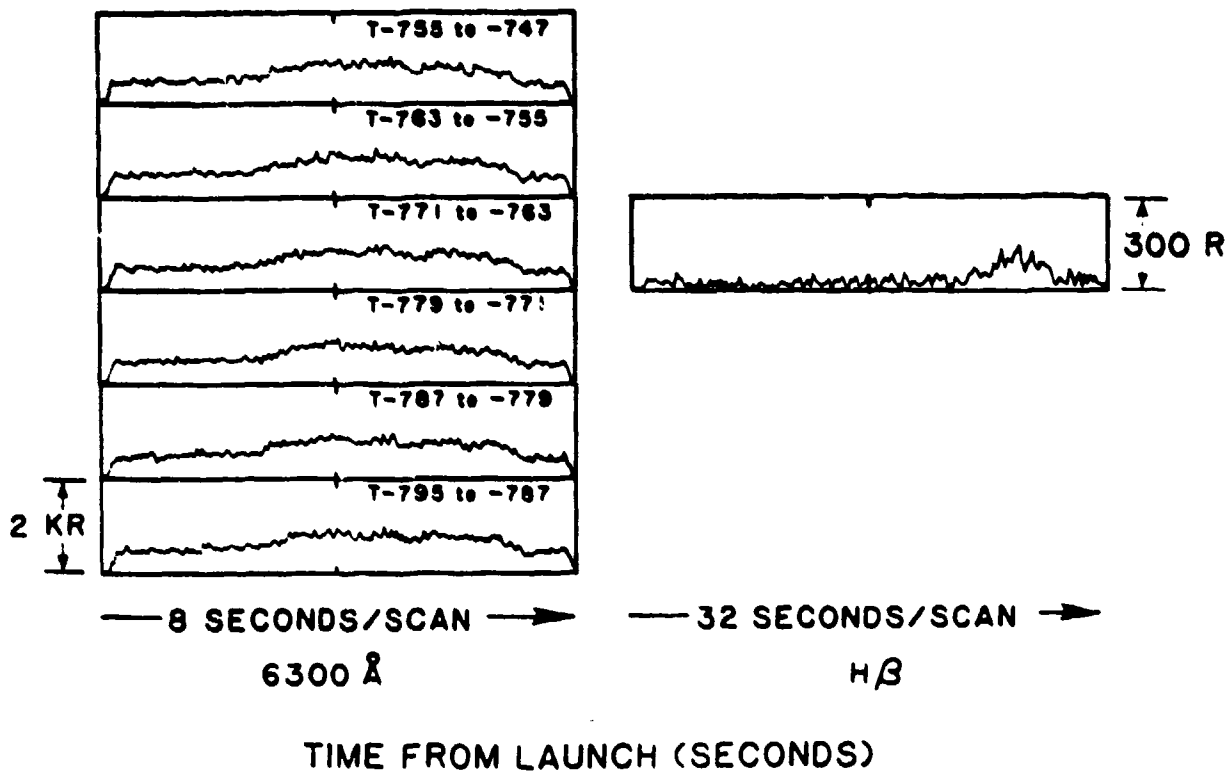
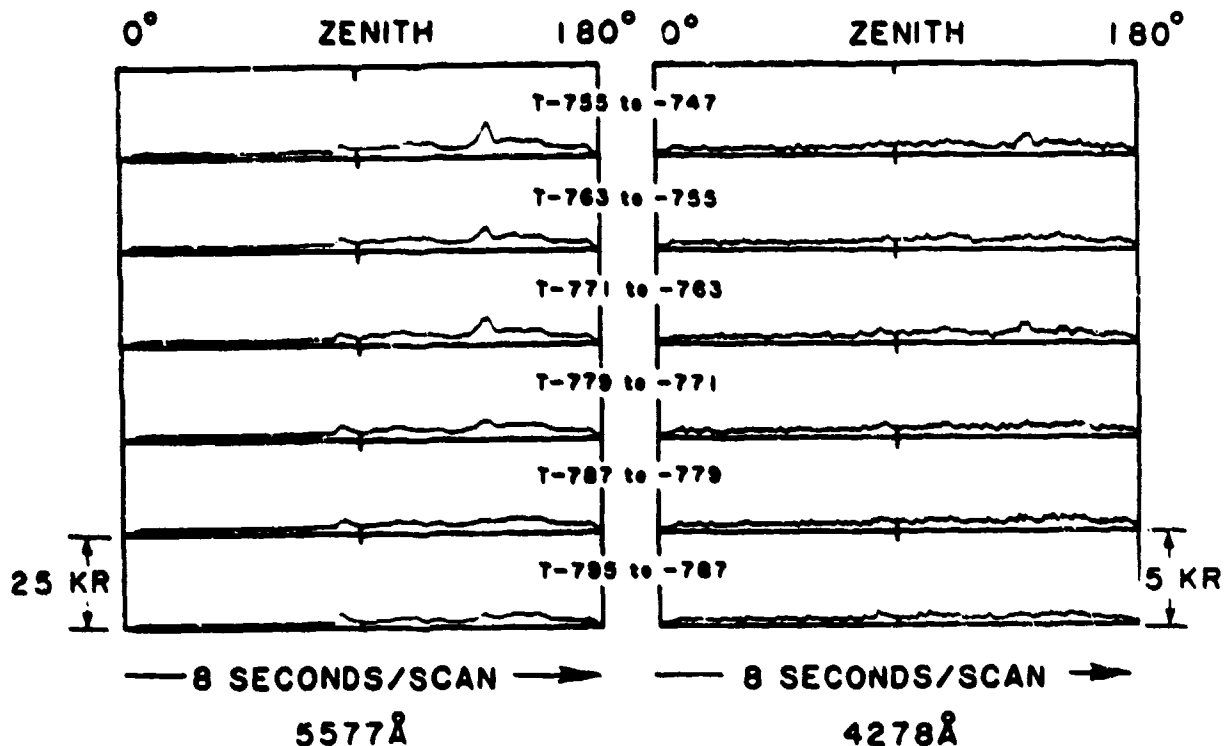


Figure 14. Meridian scanning photometers at 5577 Å, 4278 Å, 6300 Å, and H $\beta$ , for the time period T-795 seconds through T-747 seconds.

### MERIDIAN SCANNING PHOTOMETERS

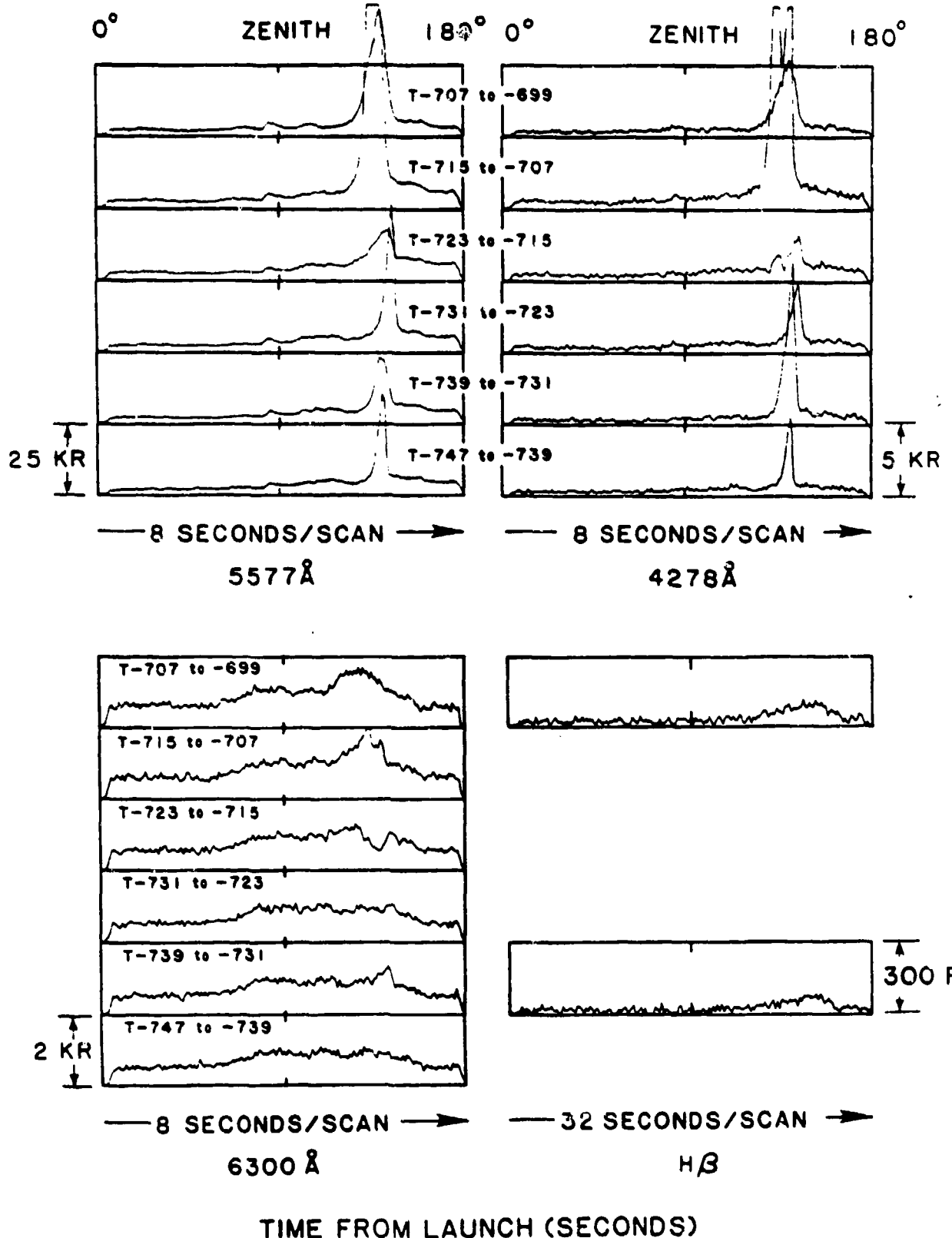


Figure 15. Meridian scanning photometers at 5577 Å, 4278 Å, 6300 Å, and H $\beta$ , for the time period T-747 seconds through T-699 seconds.

MERIDIAN SCANNING PHOTOMETERS

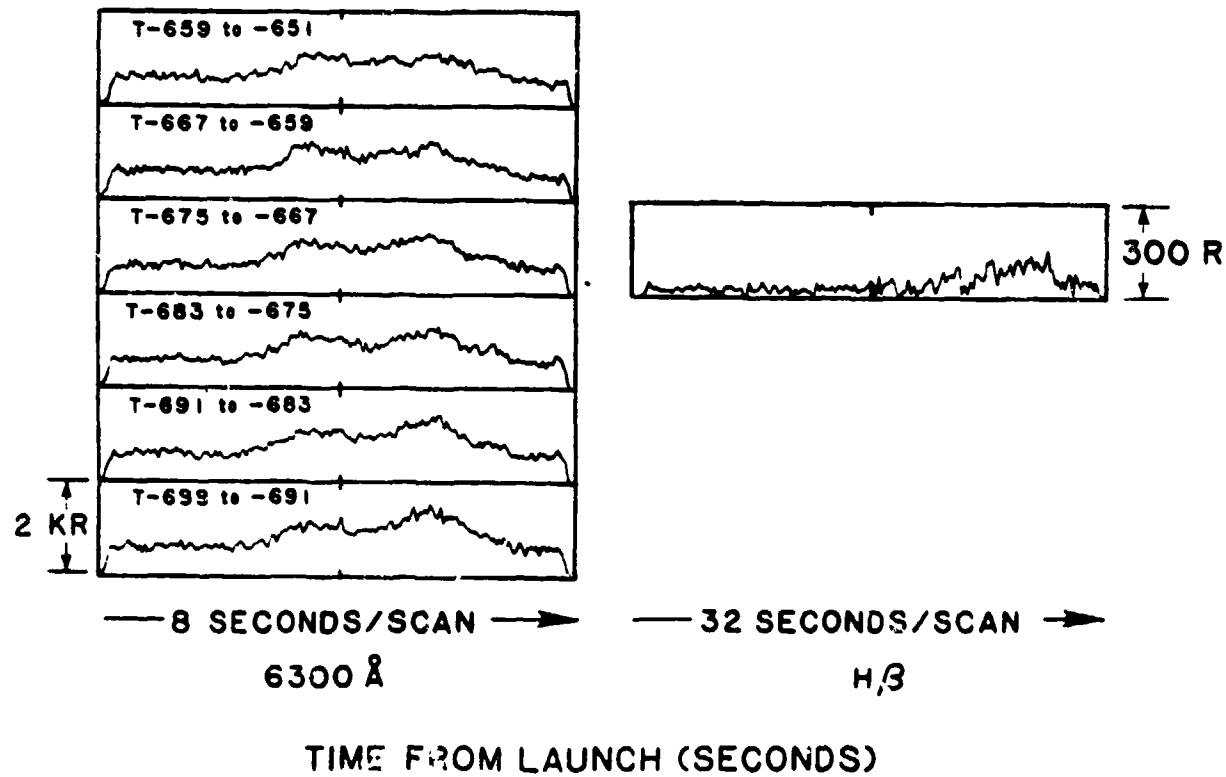
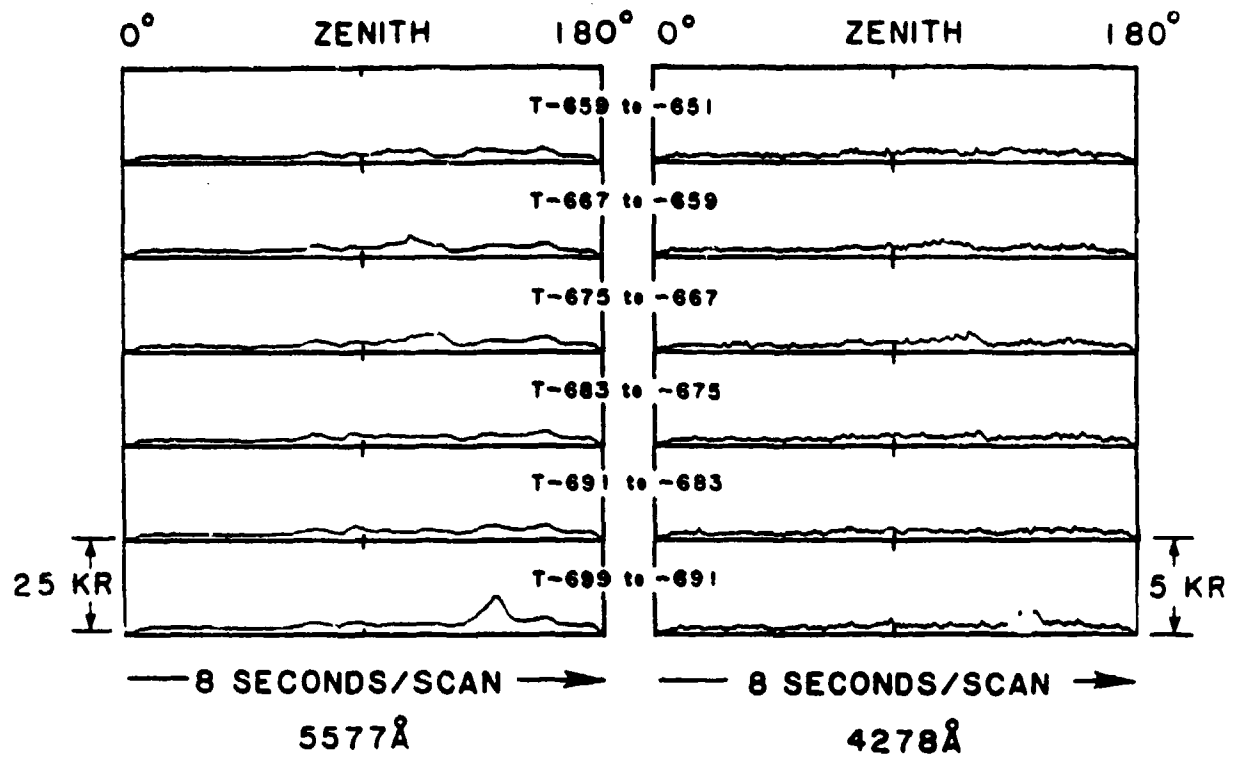


Figure 16. Meridian scanning photometers at 5577 Å, 4278 Å, 6300 Å, and H $\beta$ , for the time period T-699 seconds through T-651 seconds.

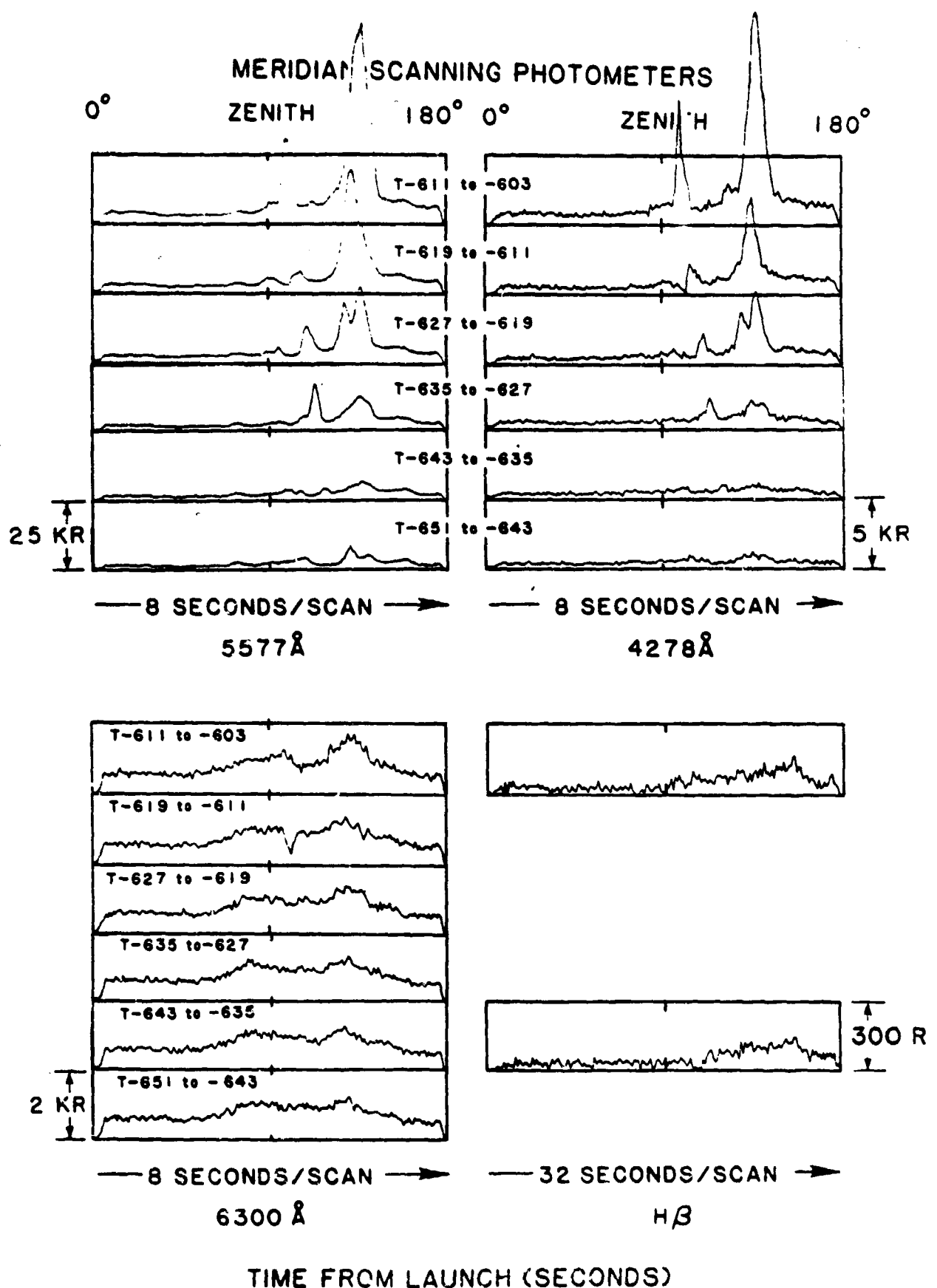


Figure 17. Meridian scanning photometers at 5577 Å, 4278 Å, 6300 Å, and H $\beta$ , for the time period T-651 seconds through T-603 seconds.

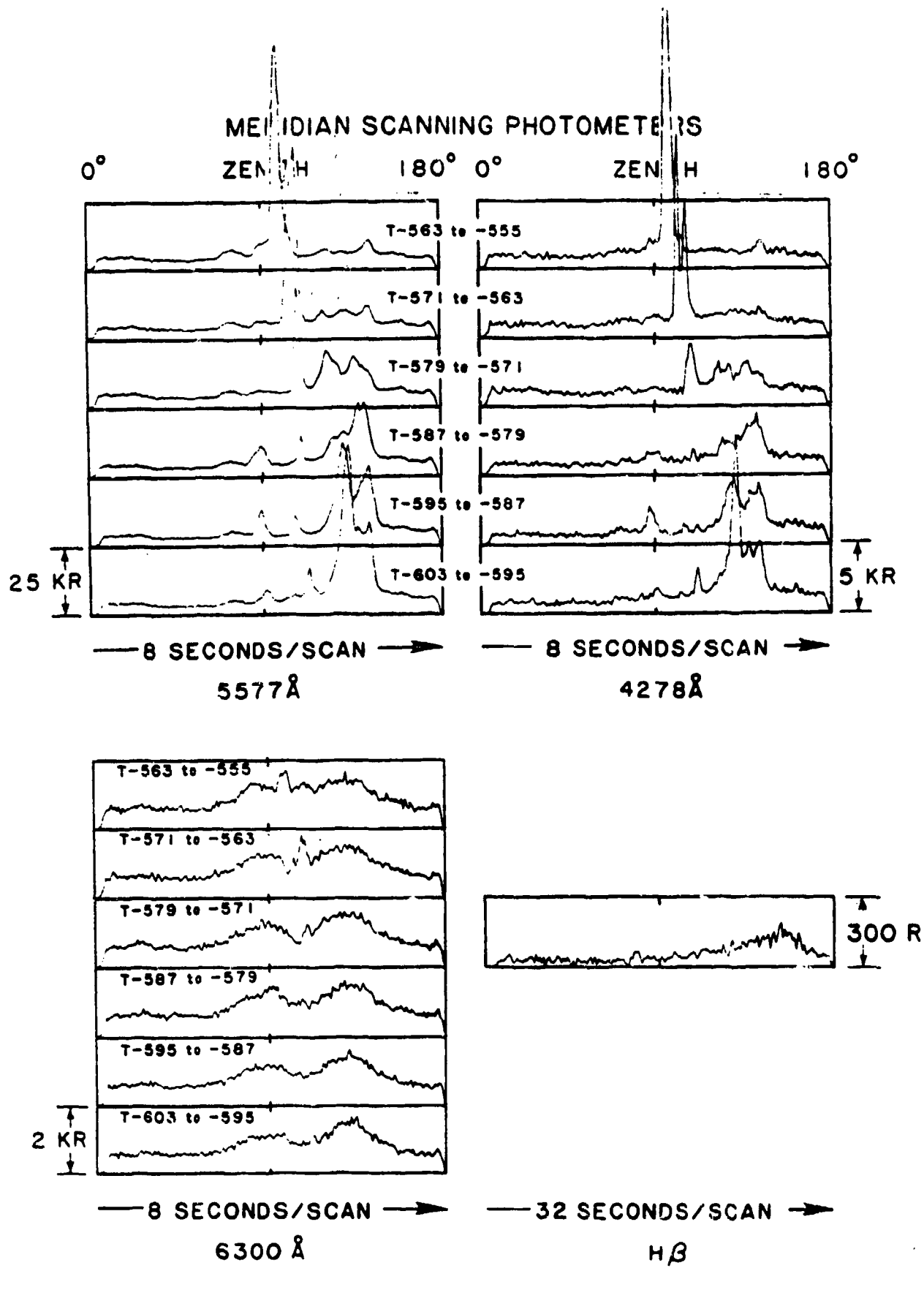


Figure 18. Meridian scanning photometers at 5577 Å, 4278 Å, 6300 Å, and H $\beta$ , for the time period T-603 seconds through T-555 seconds.

### MERIDIAN SCANNING PHOTOMETERS

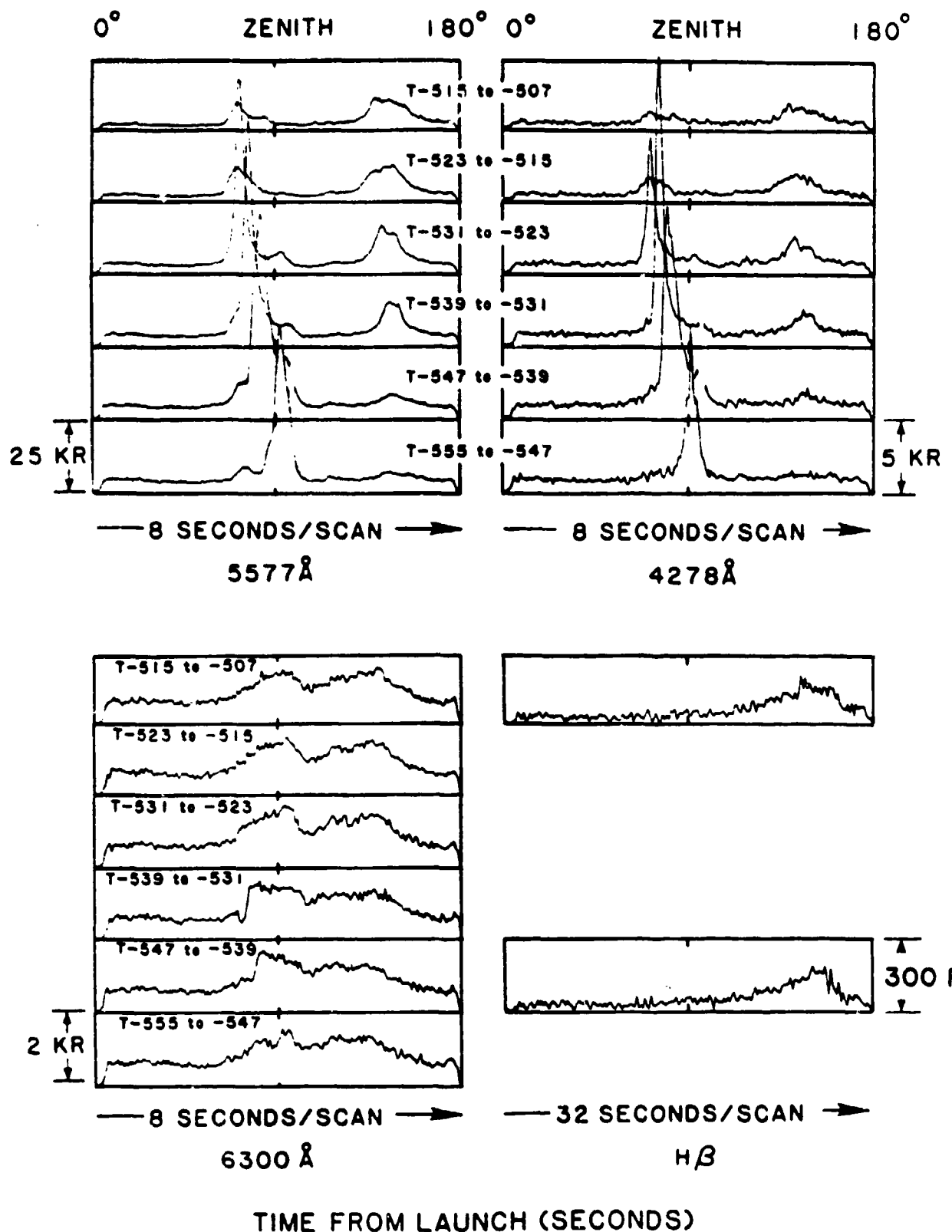


Figure 19. Meridian scanning photometers at 5577 Å, 4278 Å, 6300 Å, and H $\beta$ , for the time period T-555 seconds through T-507 seconds.

### MERIDIAN SCANNING PHOTOMETERS

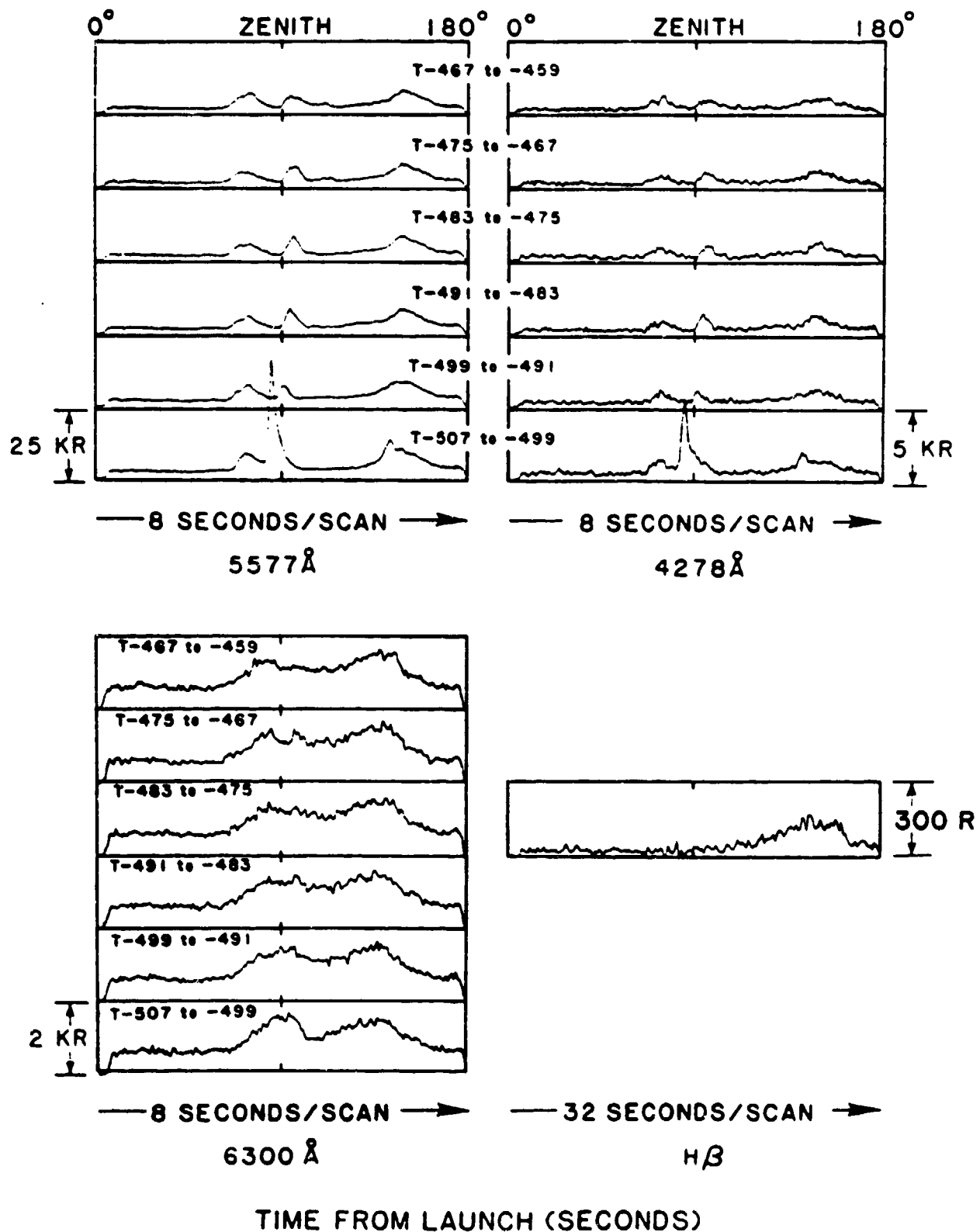


Figure 20. Meridian scanning photometers at 5577 Å, 4278 Å, 6300 Å, and H $\beta$ , for the time period T-507 seconds through T-459 seconds.

### MERIDIAN SCANNING PHOTOMETERS

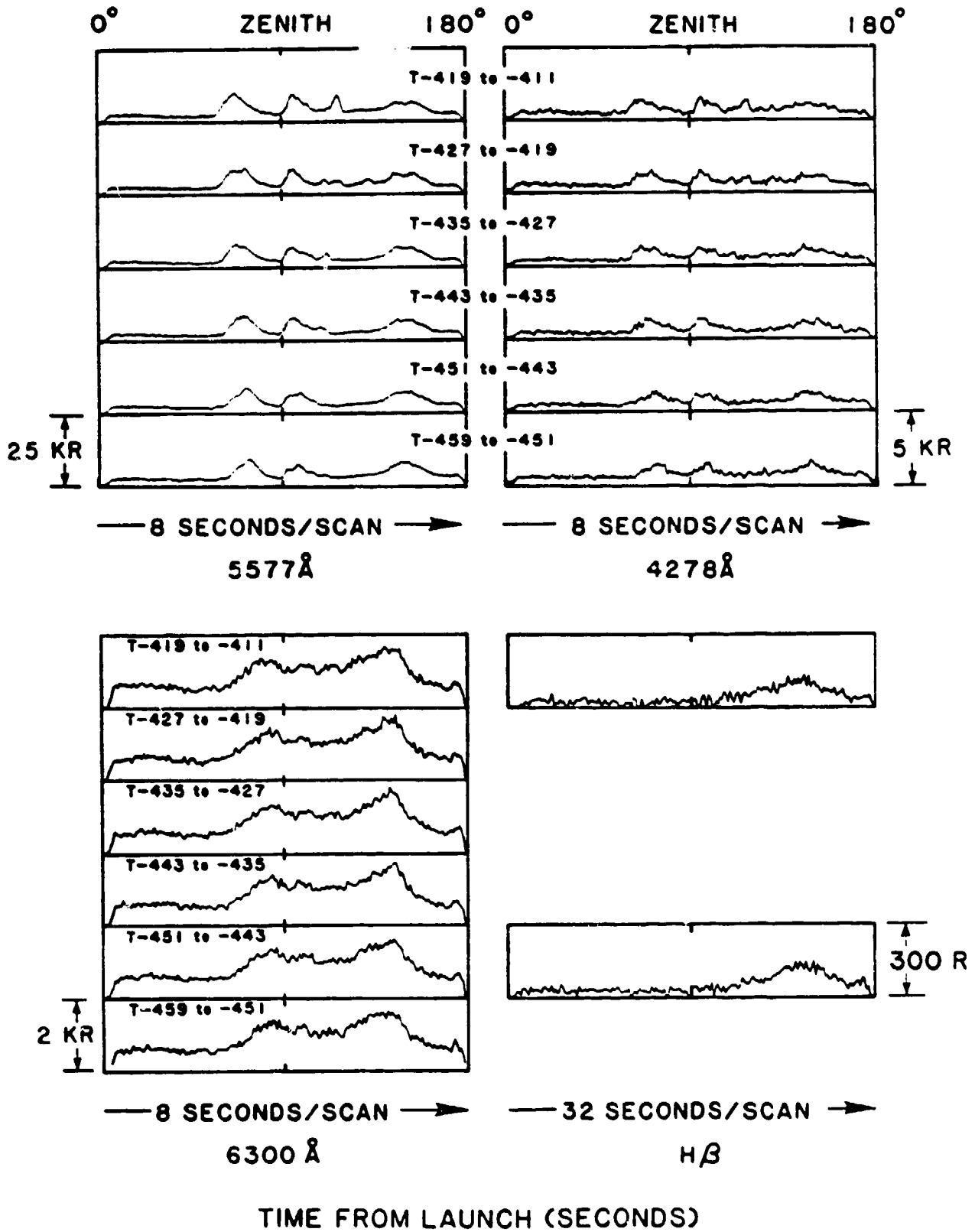


Figure 21. Meridian scanning photometers at 5577 Å, 4278 Å, 6300 Å, and H $\beta$ , for the time period T-459 seconds through T-411 seconds.

### MERIDIAN SCANNING PHOTOMETERS

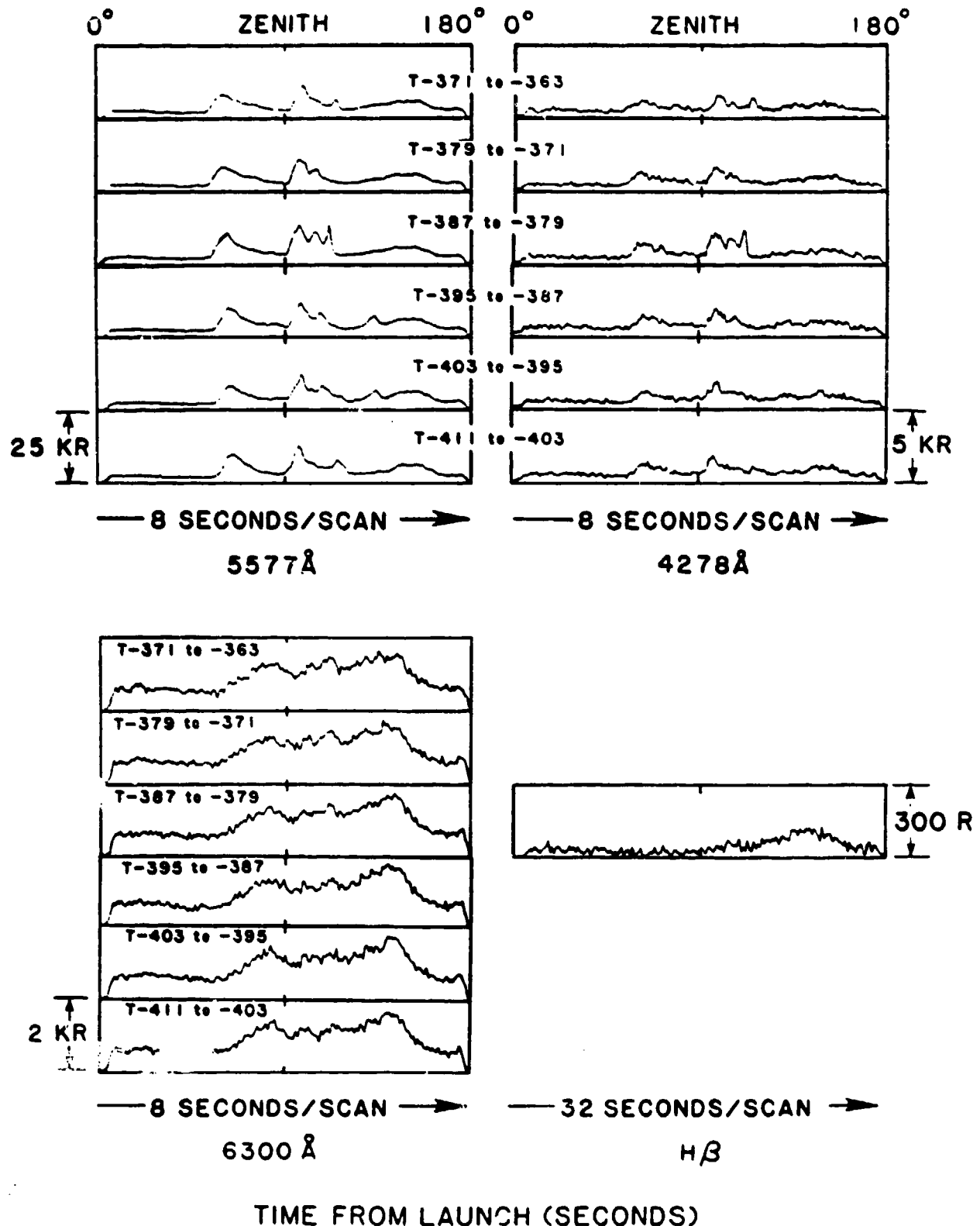


Figure 22. Meridian scanning photometers at 5577 Å, 4278 Å, 6300 Å, and H $\beta$ , for the time period T-411 seconds through T-363 seconds.

# MERIDIAN SCANNING PHOTOMETERS

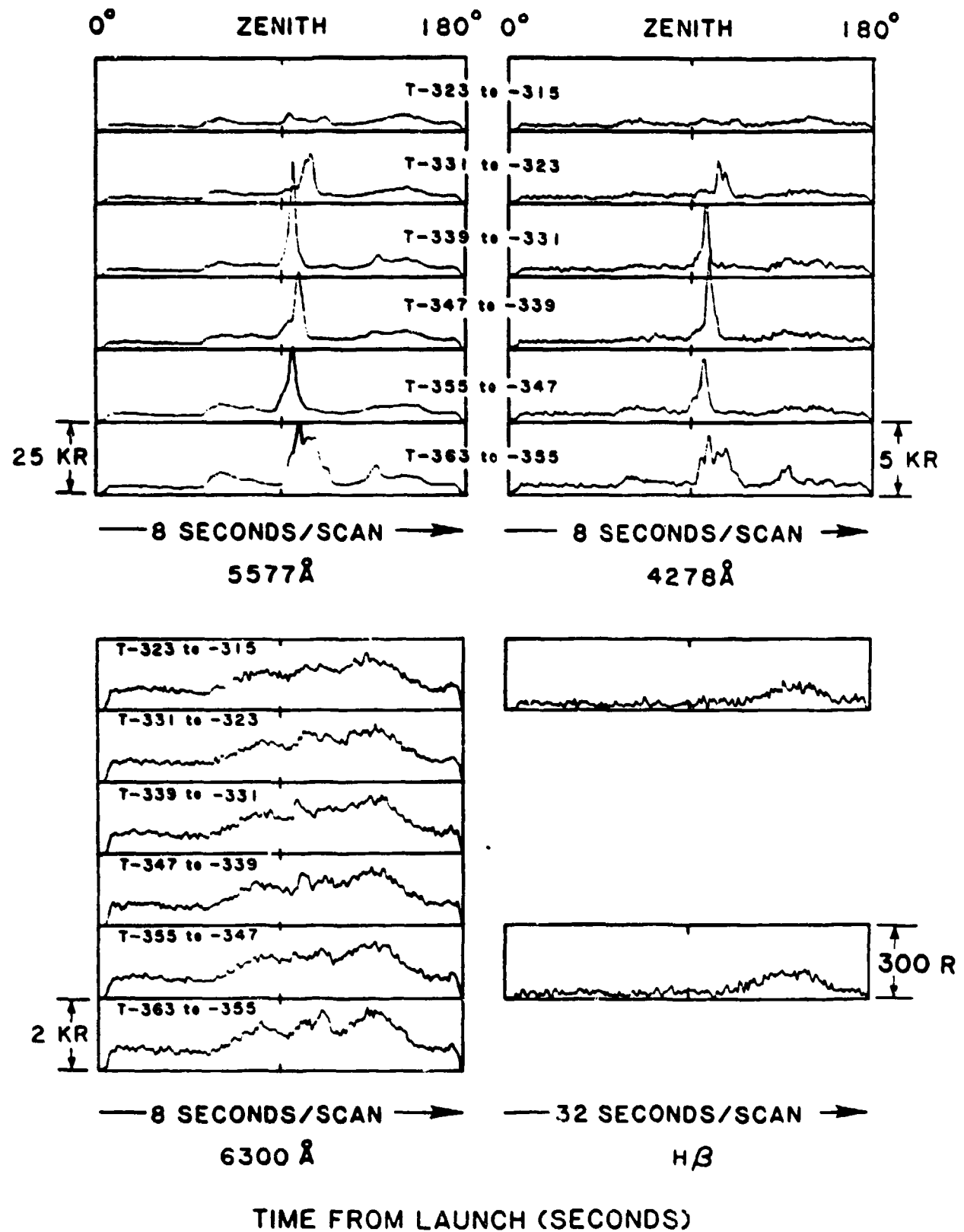


Figure 23. Meridian scanning photometers at 5577 Å, 4278 Å, 6300 Å, and H $\beta$ , for the time period T-363 seconds through T-315 seconds.

### MERIDIAN SCANNING PHOTOMETERS

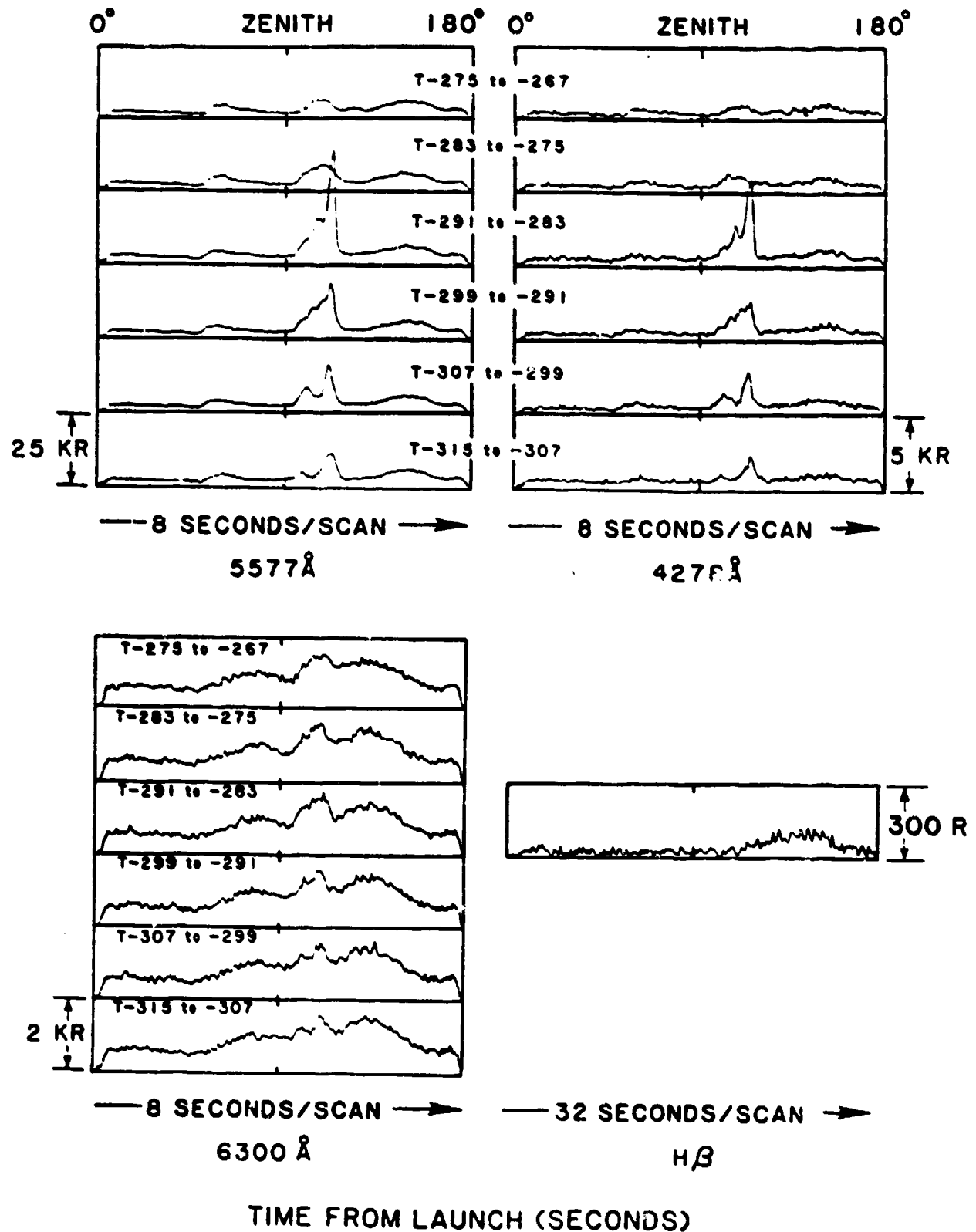


Figure 24. Meridian scanning photometers at 5577 Å, 4278 Å, 6300 Å, and H $\beta$ , for the time period T-315 seconds through T-267 seconds.

### MERIDIAN SCANNING PHOTOMETERS

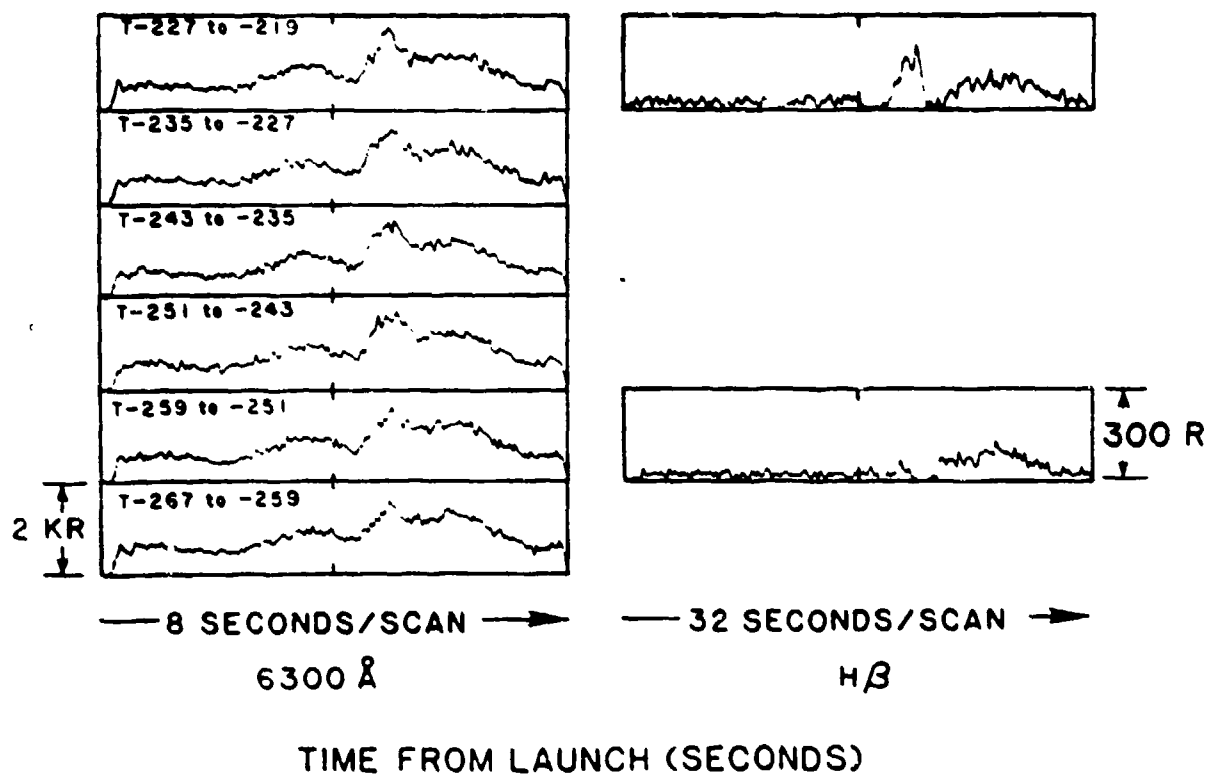
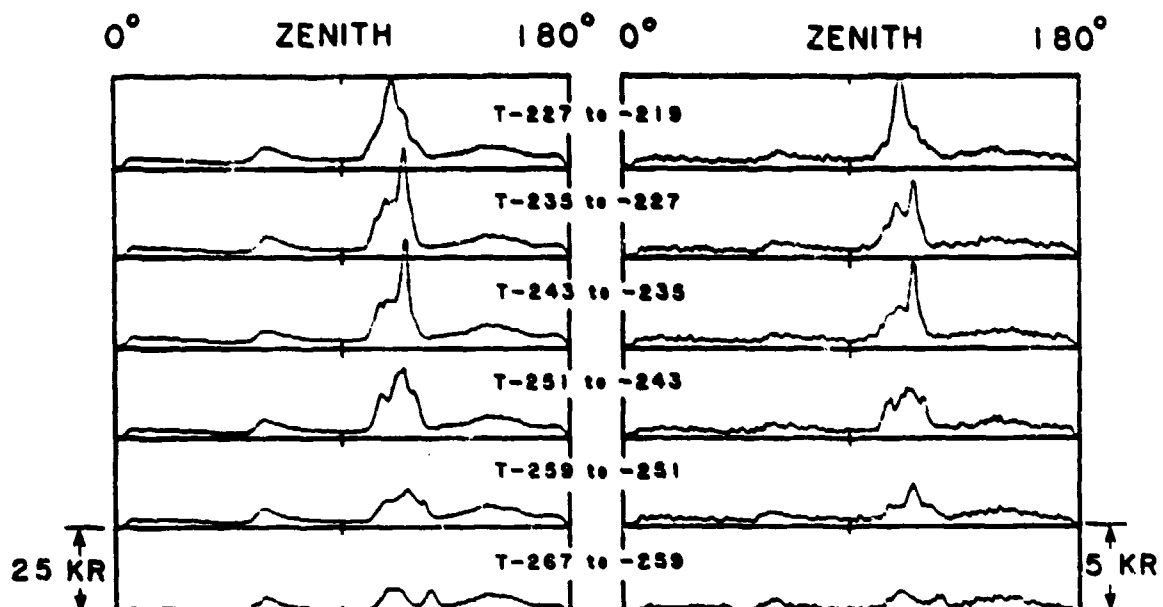


Figure 25. Meridian scanning photometers at 5577 Å, 4278 Å, 6300 Å, and H $\beta$ , for the time period T-267 seconds through T-219 seconds.

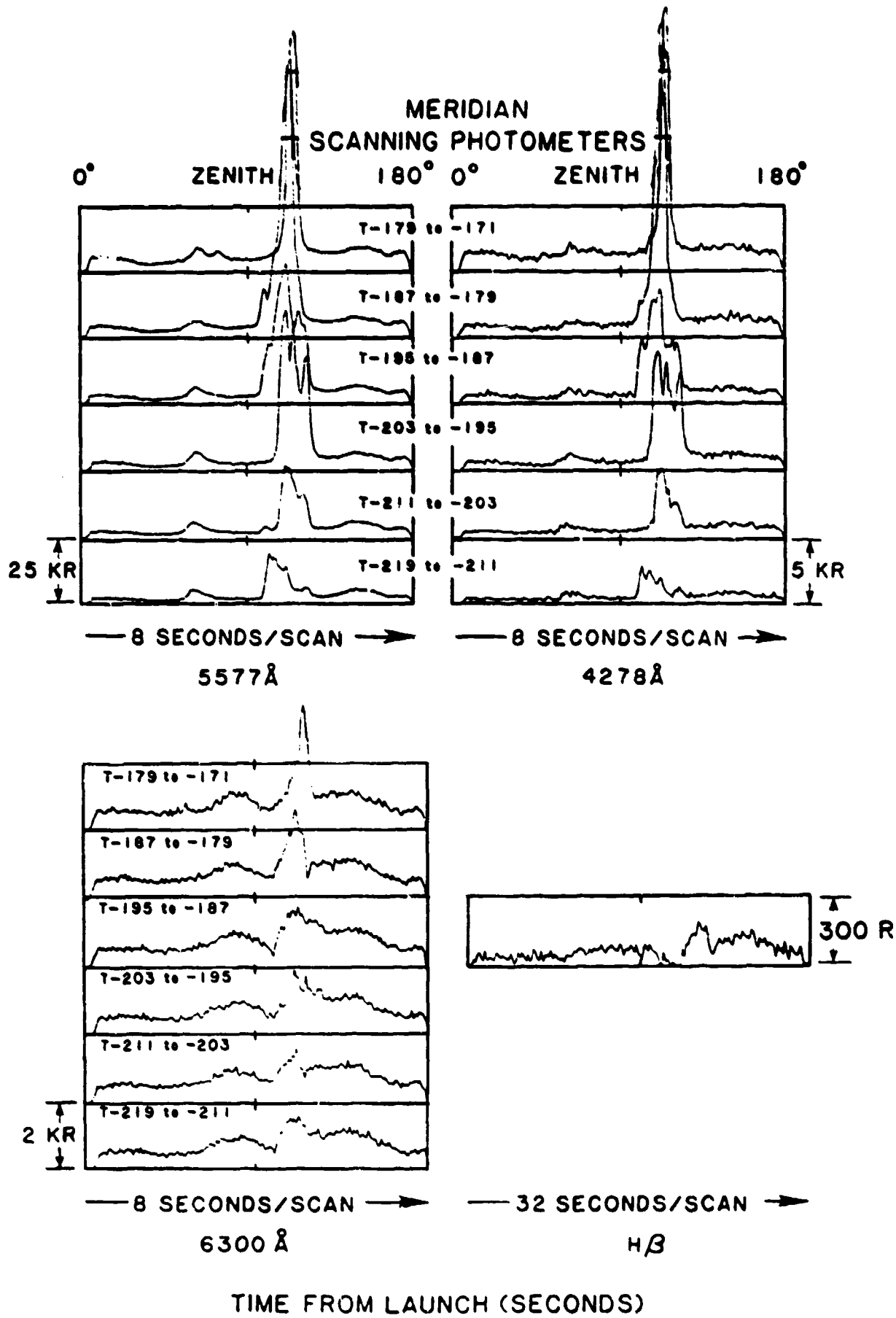


Figure 26. Meridian scanning photometers at 5577 Å, 4278 Å, 6300 Å, and H $\beta$ , for the time period T-219 seconds through T-171 seconds.

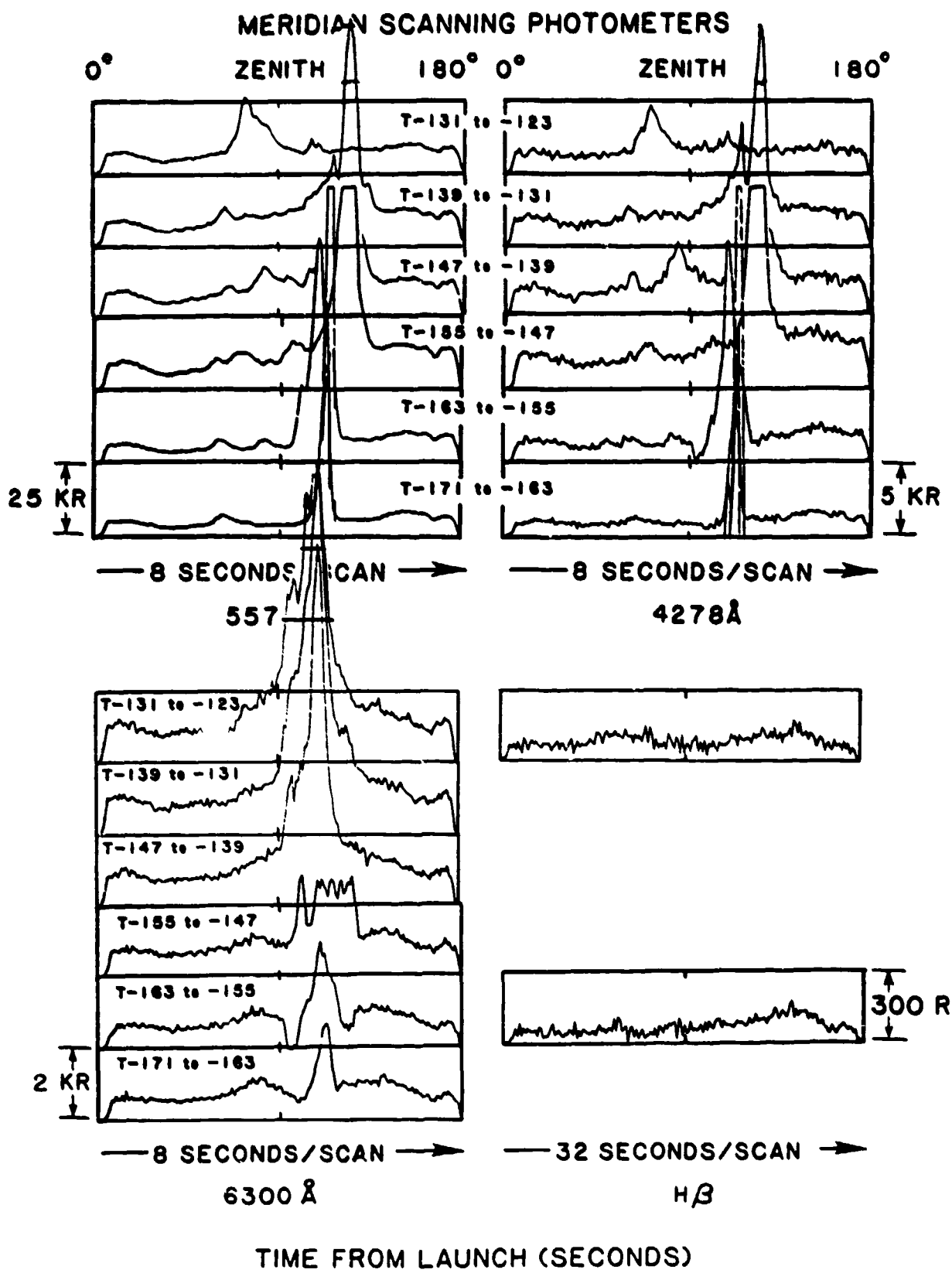
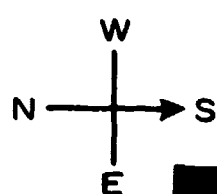
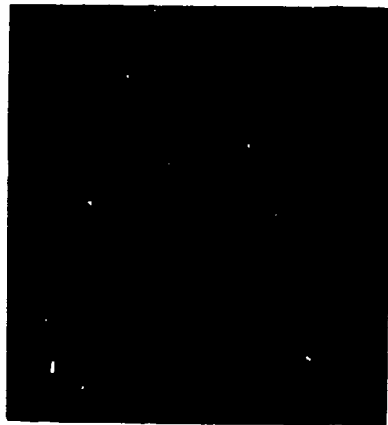


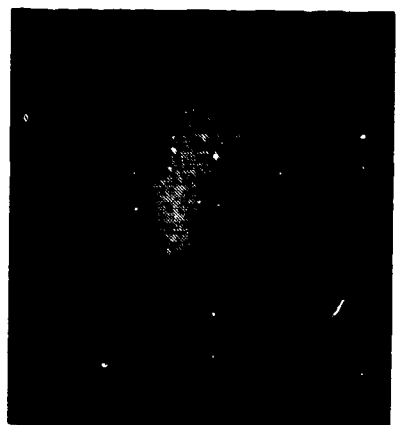
Figure 27. Meridian scanning photometers at  $5577\text{ Å}$ ,  $4278\text{ Å}$ ,  $6300\text{ Å}$ , and  $\text{H}\beta$ , for the time period T-171 seconds through T-123 seconds.



T-95 seconds



T-87



T-79

Figure 28. All-sky TV frames at eight-second intervals from T-95 seconds through T-79 seconds.

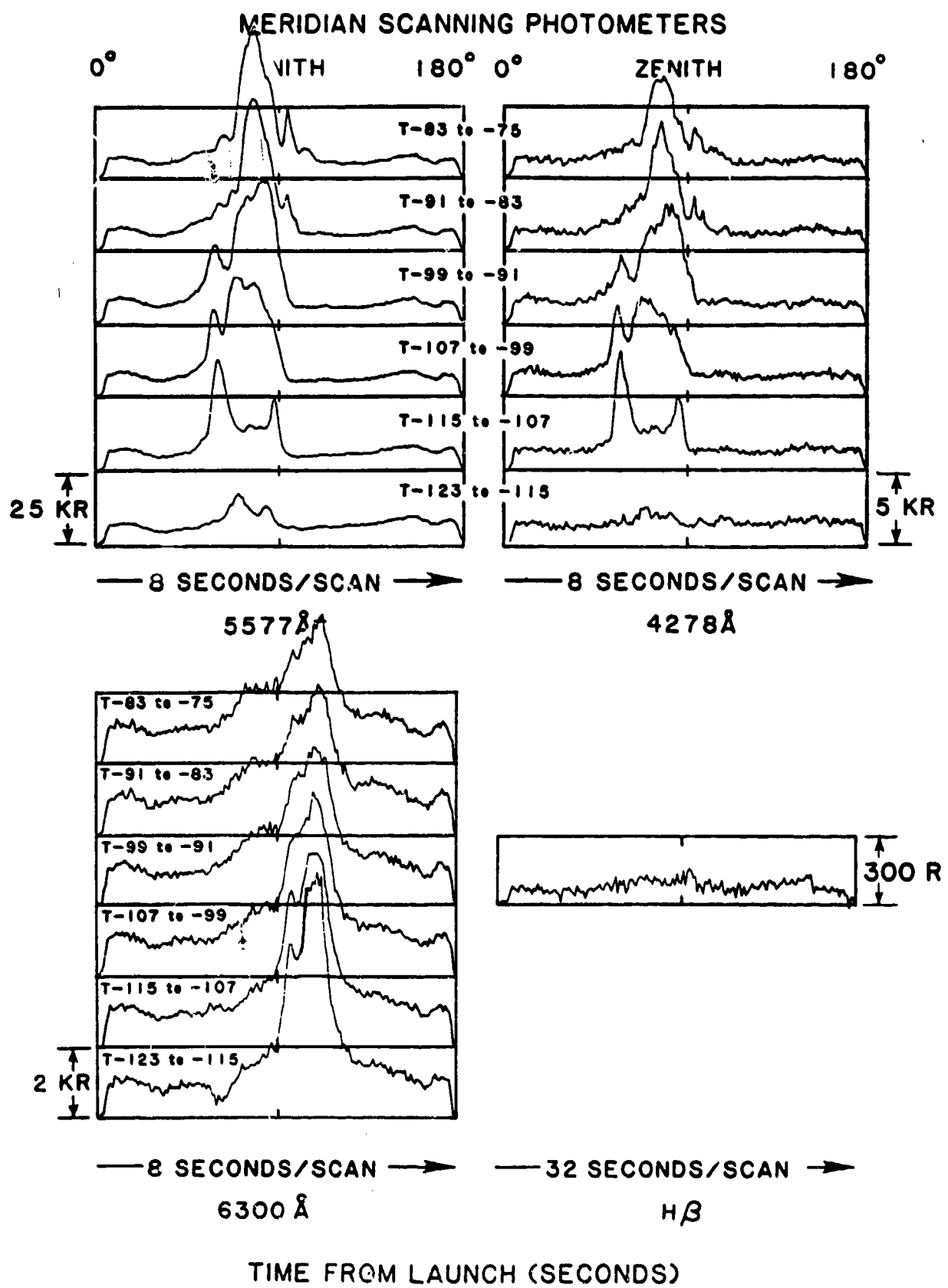
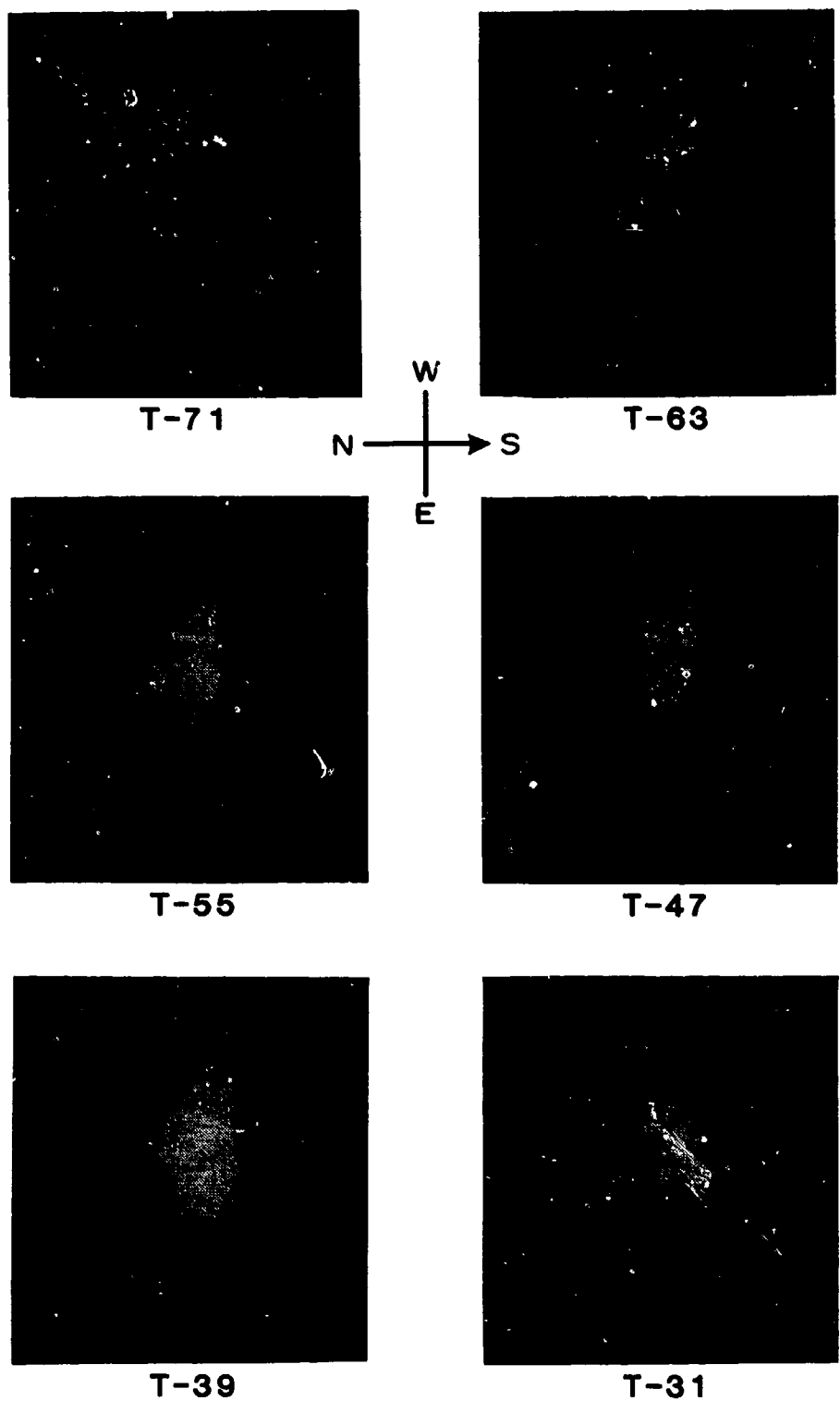


Figure 29. Meridian scanning photometers at 5577 Å, 4278 Å, 6300 Å, and H $\beta$ , for the time period T-123 seconds through T-75 seconds.



**Figure 30.** All-sky TV frames at eight-second intervals from T-71 seconds through T-31 seconds.

### MERIDIAN SCANNING PHOTOMETERS

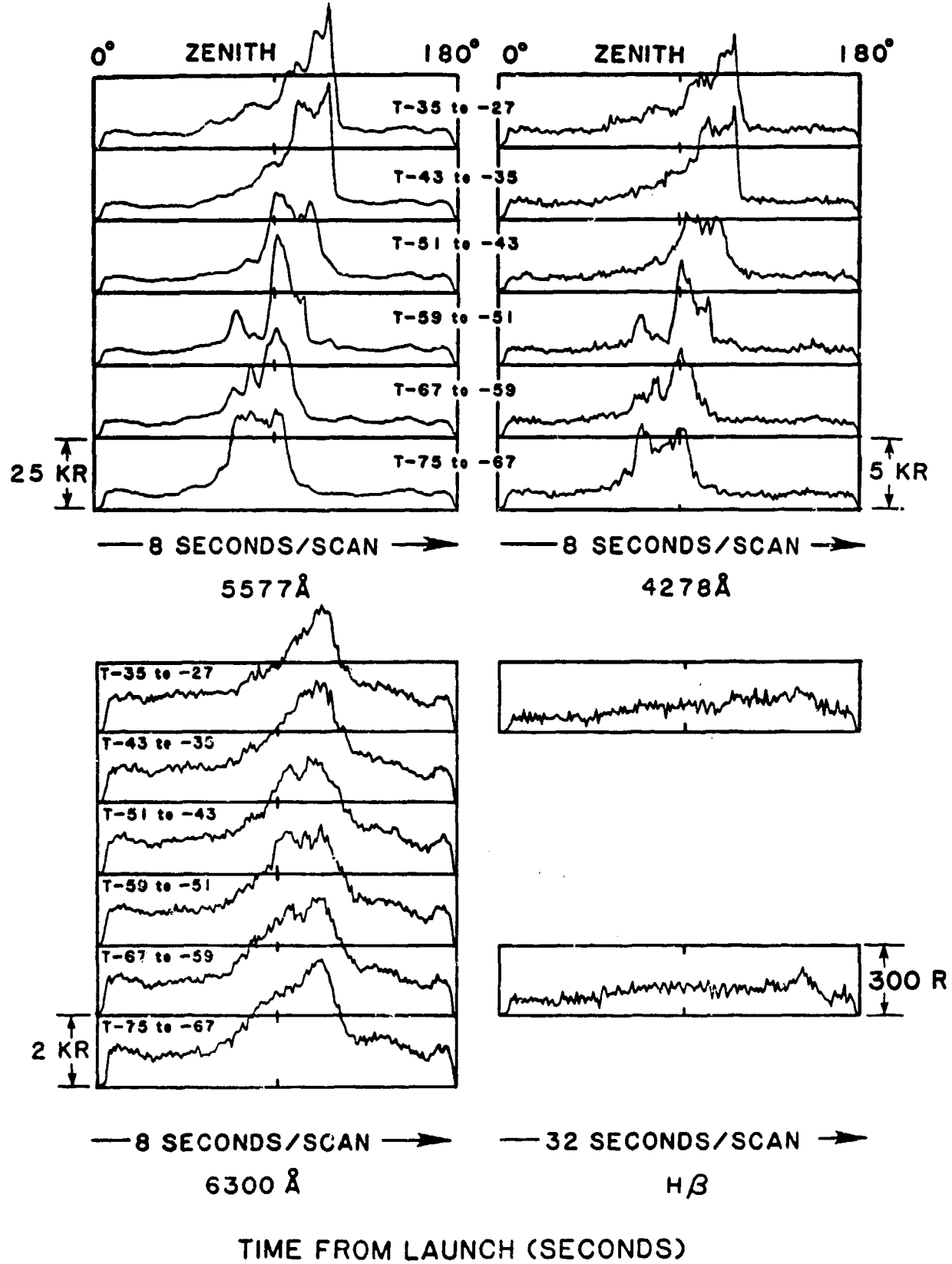


Figure 31. Meridian scanning photometers at 5577 Å, 4278 Å, 6300 Å, and H $\beta$ , for the time period T-75 seconds through T-27 seconds.

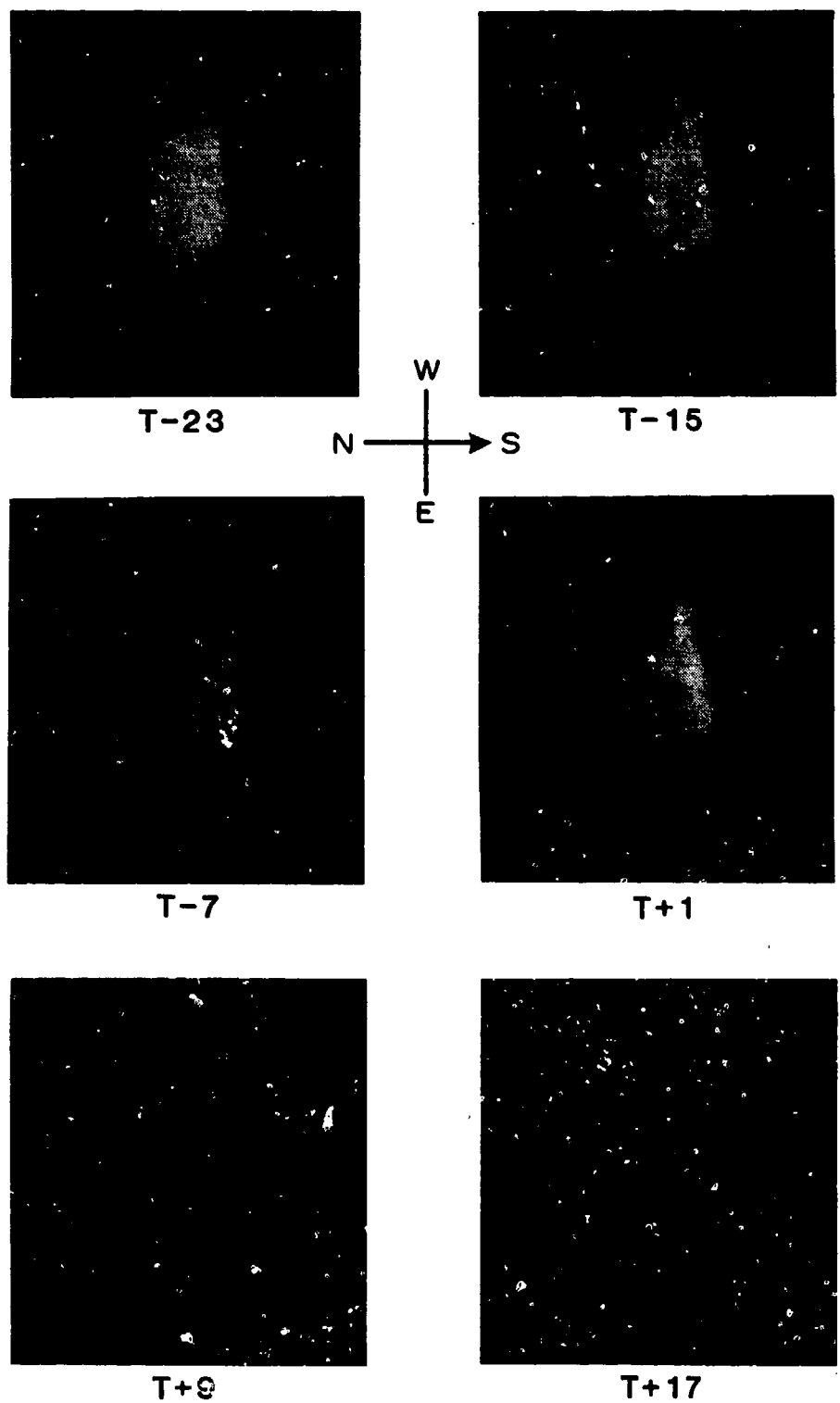


Figure 32. All-sky TV frames at eight-second intervals from T-23 seconds through T+17 seconds.

### MERIDIAN SCANNING PHOTOMETERS

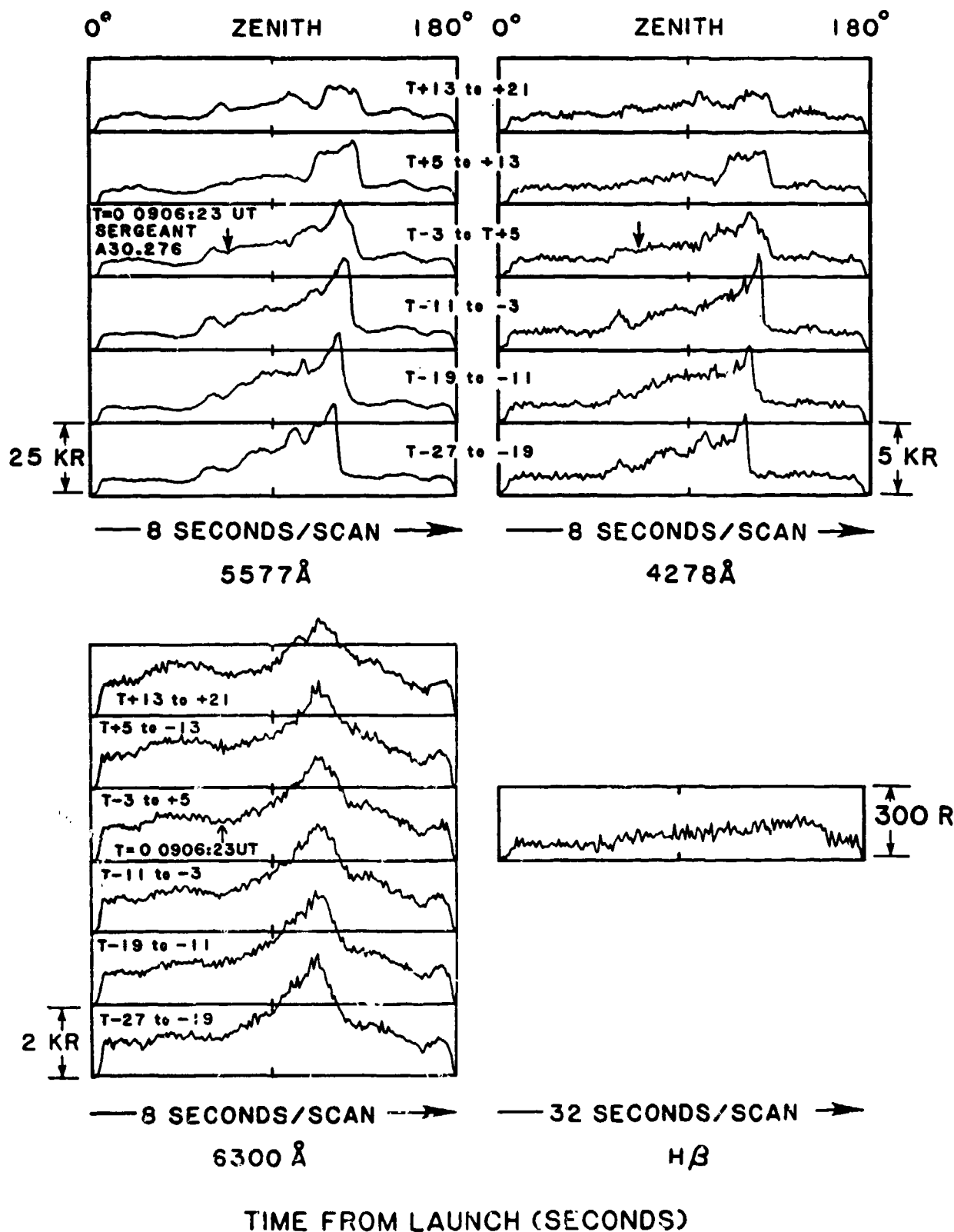


Figure 33. Meridian scanning photometers at 5577 Å, 4278 Å, 6300 Å, and H $\beta$ , for the time period T-27 seconds through T-21 seconds.

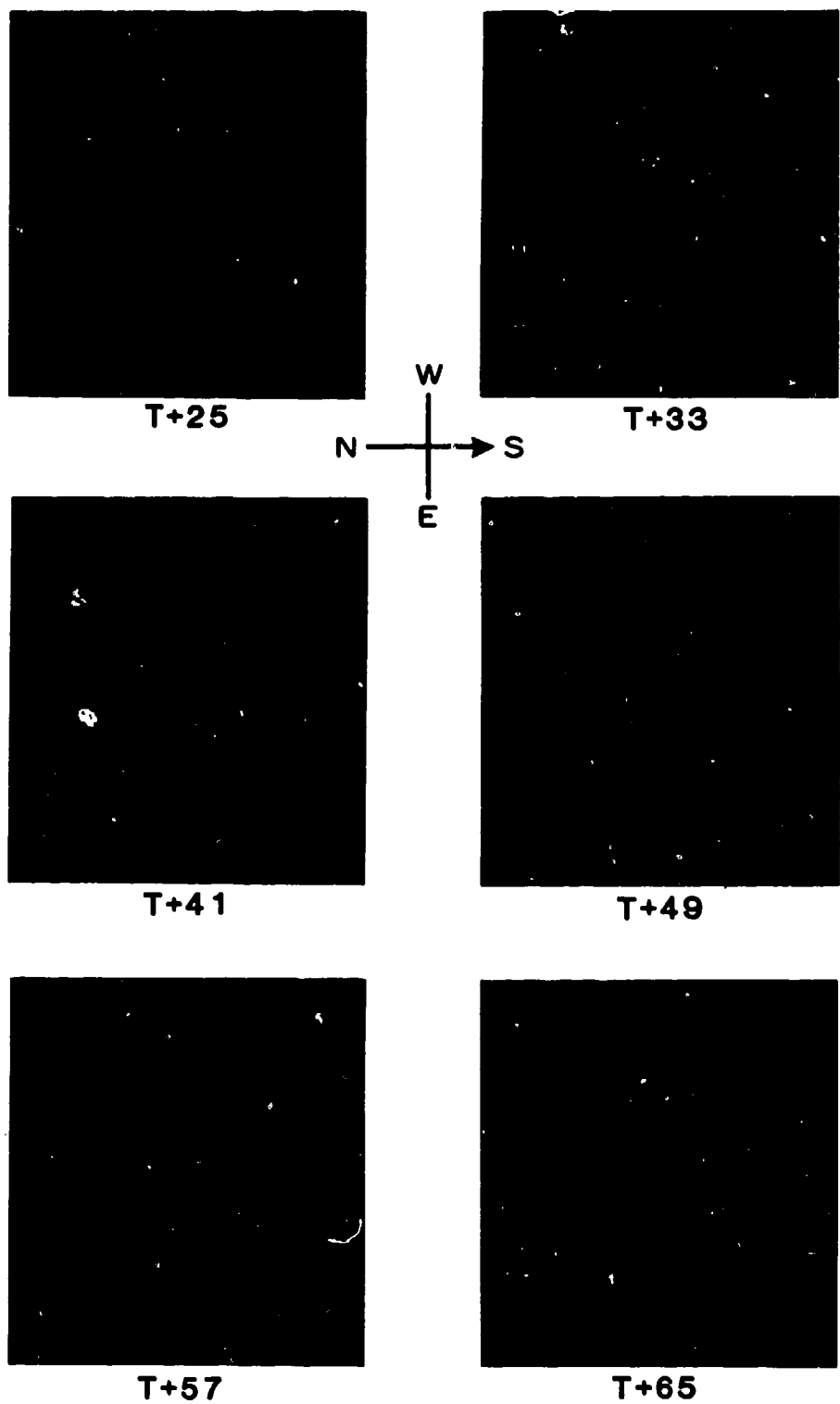


Figure 34. All-sky TV frames at eight-second intervals from T-25 seconds through T+65 seconds.

### MERIDIAN SCANNING PHOTOMETERS

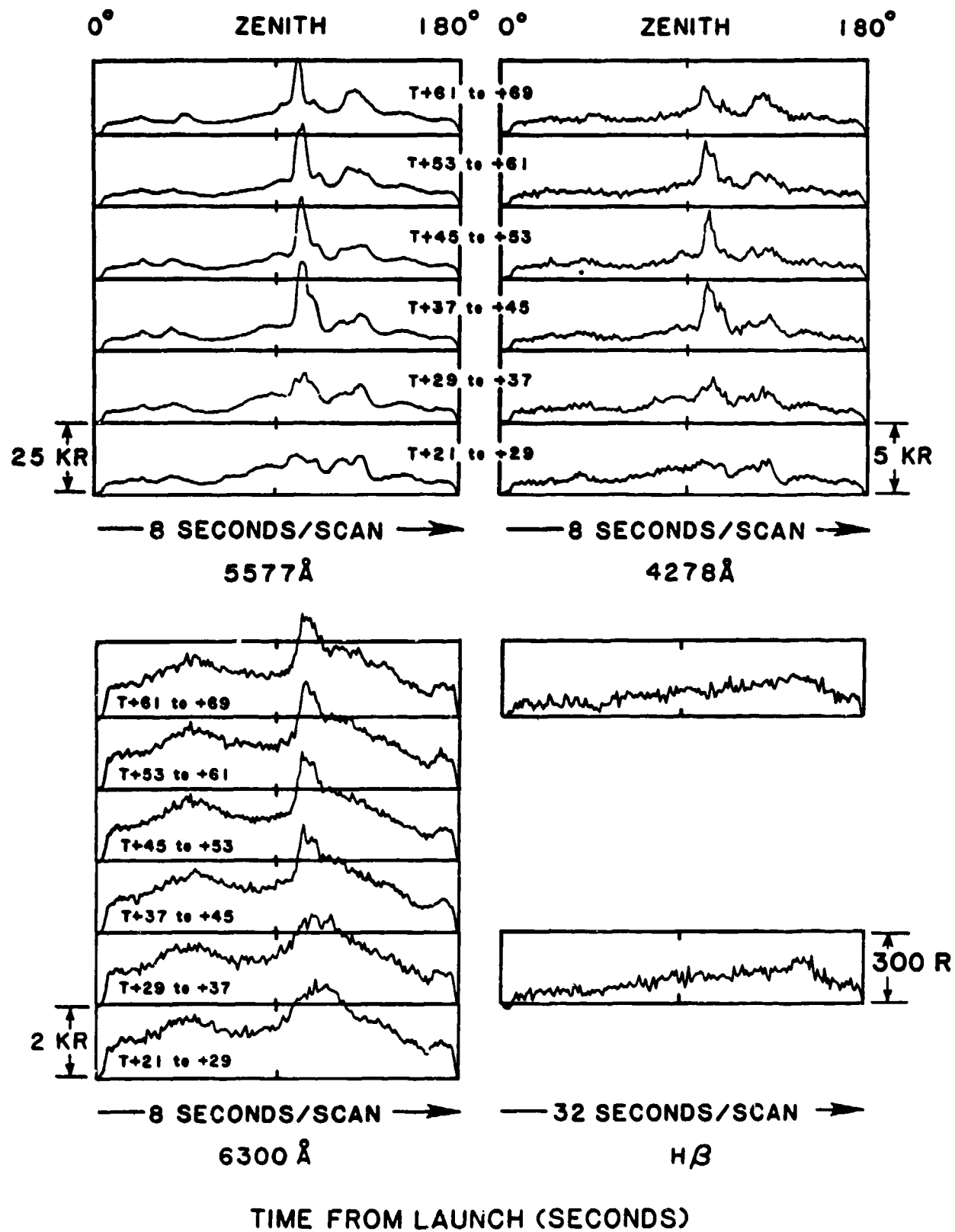
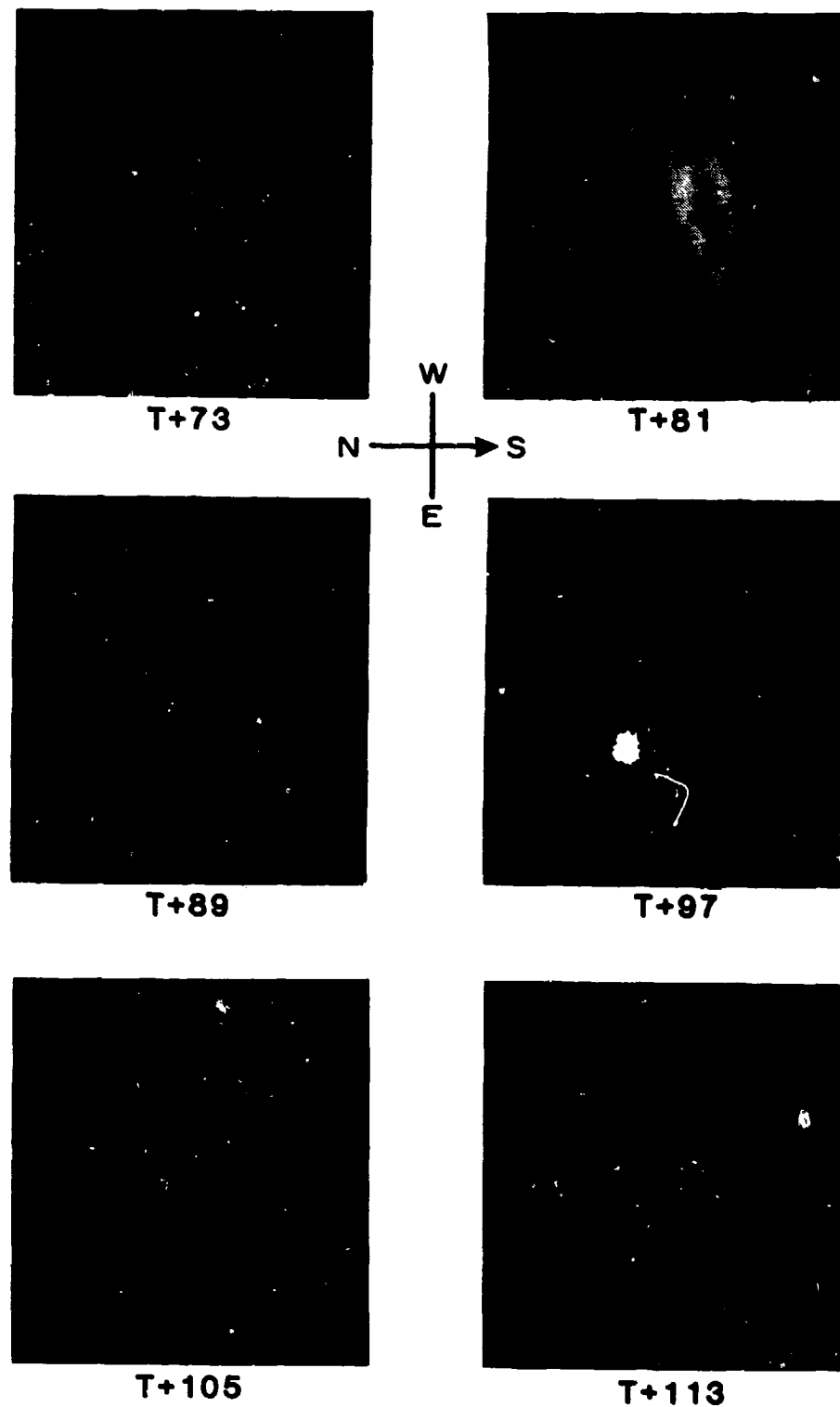


Figure 35. Meridian scanning photometers at 5577 Å, 4278 Å, 6300 Å, and H $\beta$ , for the time period T+21 seconds through T+69 seconds.



**Figure 36.** All-sky TV frames at eight-second intervals from T+73 seconds through T+113 seconds.

## MERIDIAN SCANNING PHOTOMETERS

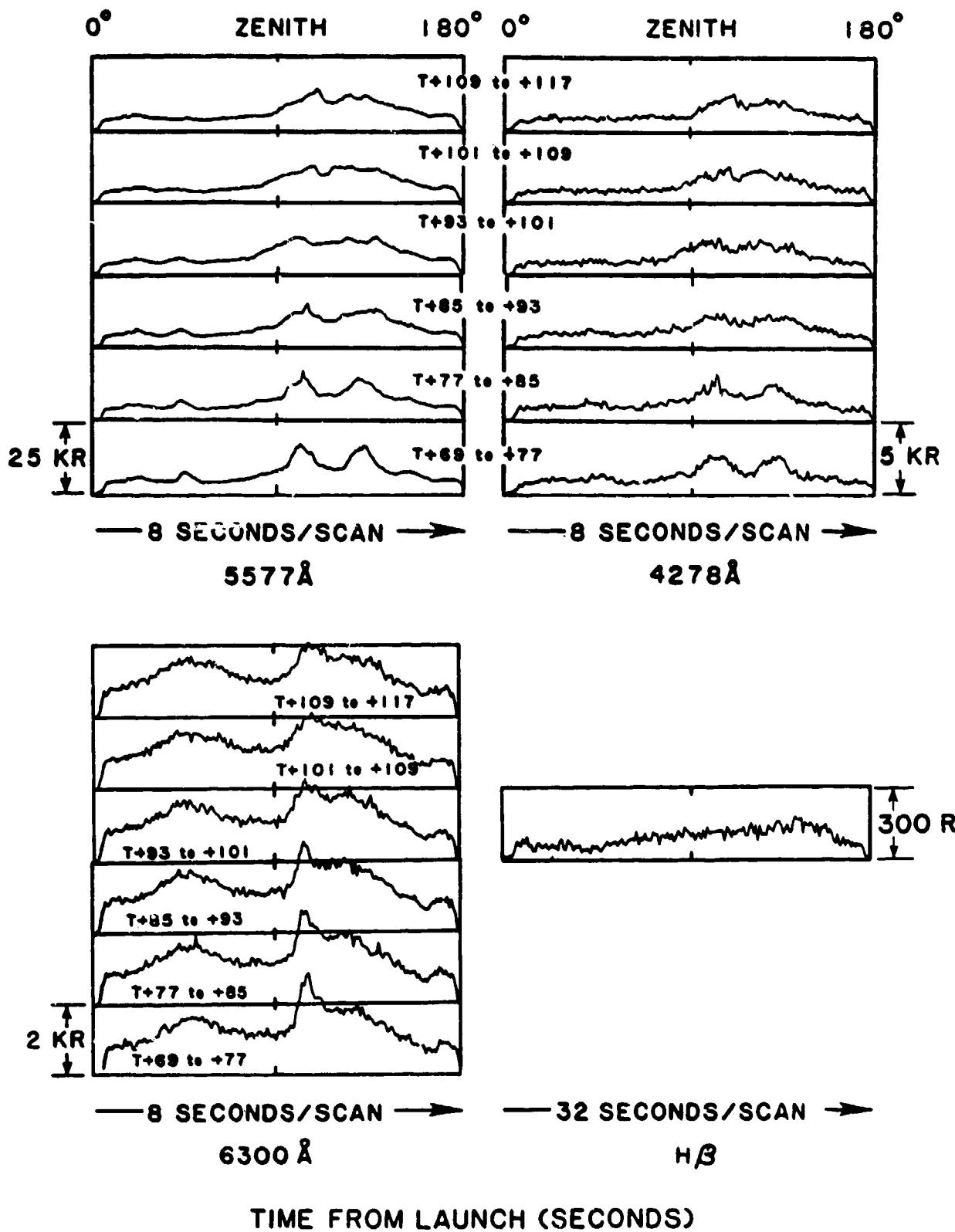


Figure 37. Meridian scanning photometers at 5577 Å, 4278 Å, 6300 Å, and HB, for the time period T+69 seconds through T+117 seconds.

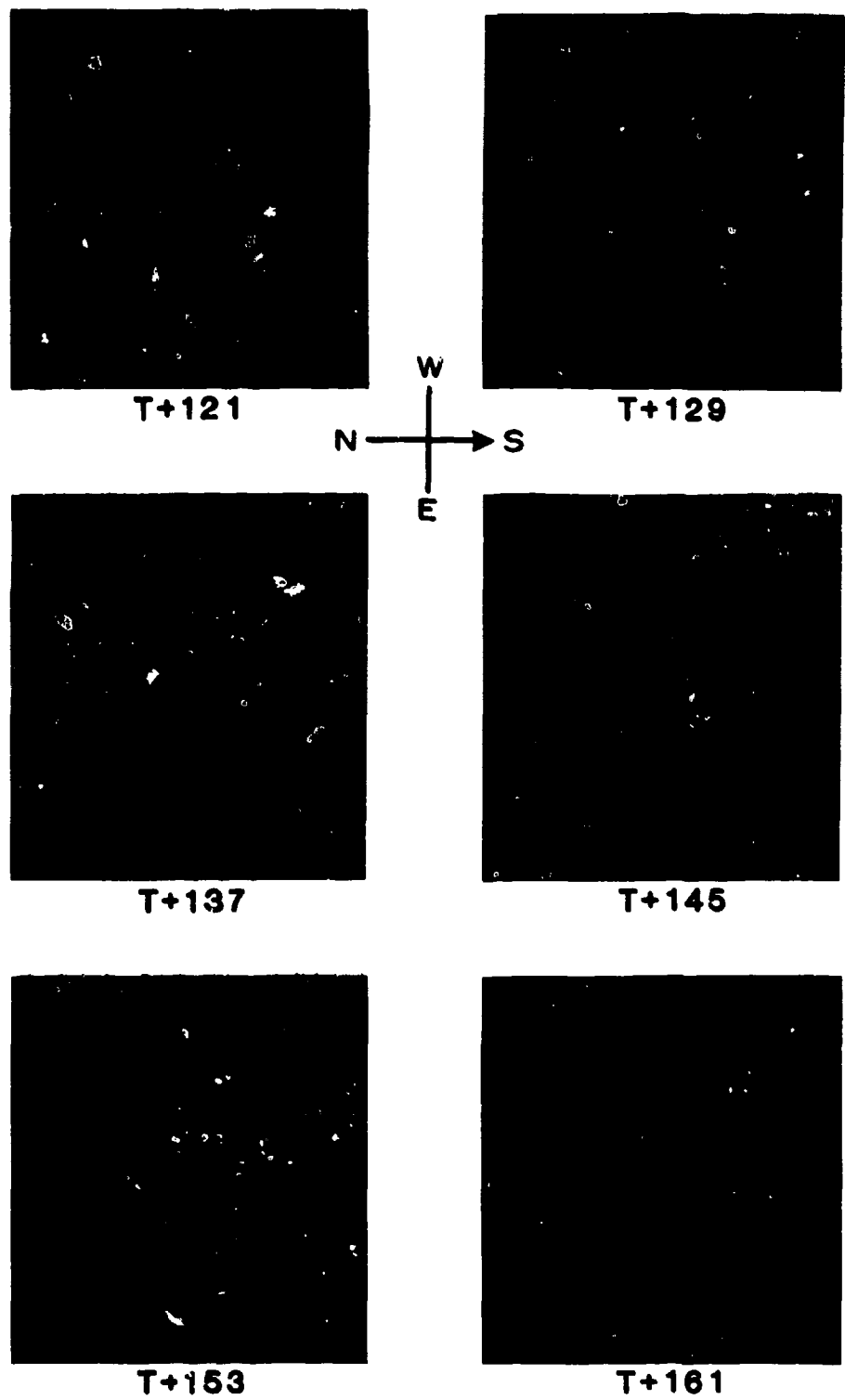


Figure 38. All-sky TV frames at eight-second intervals from T+121 seconds through T+161 seconds.

## MERIDIAN SCANNING PHOTOMETERS

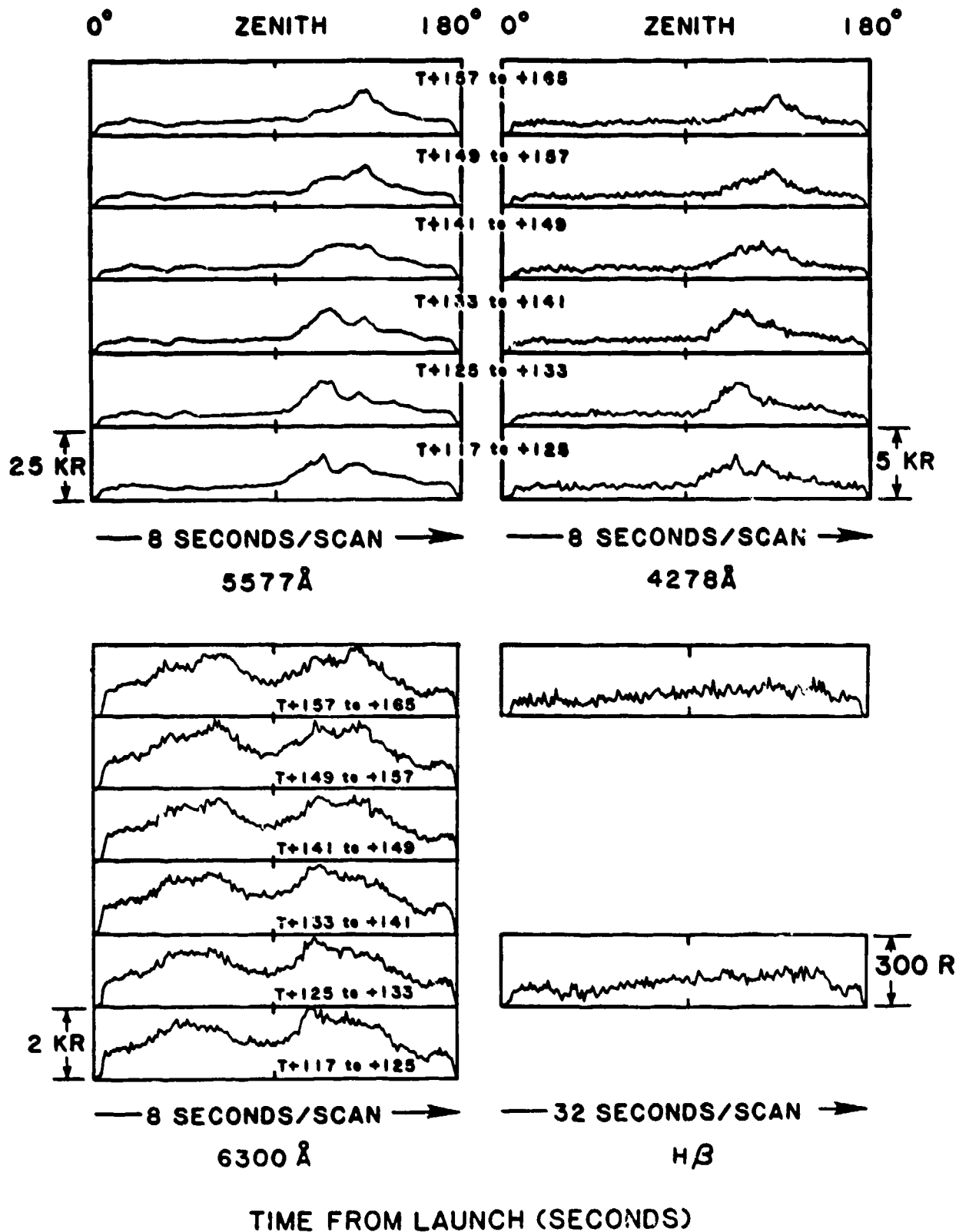


Figure 39. Meridian scanning photometers at 5577 Å, 4278 Å, 6300 Å, and HB, for the time period T+117 seconds through T+165 seconds.

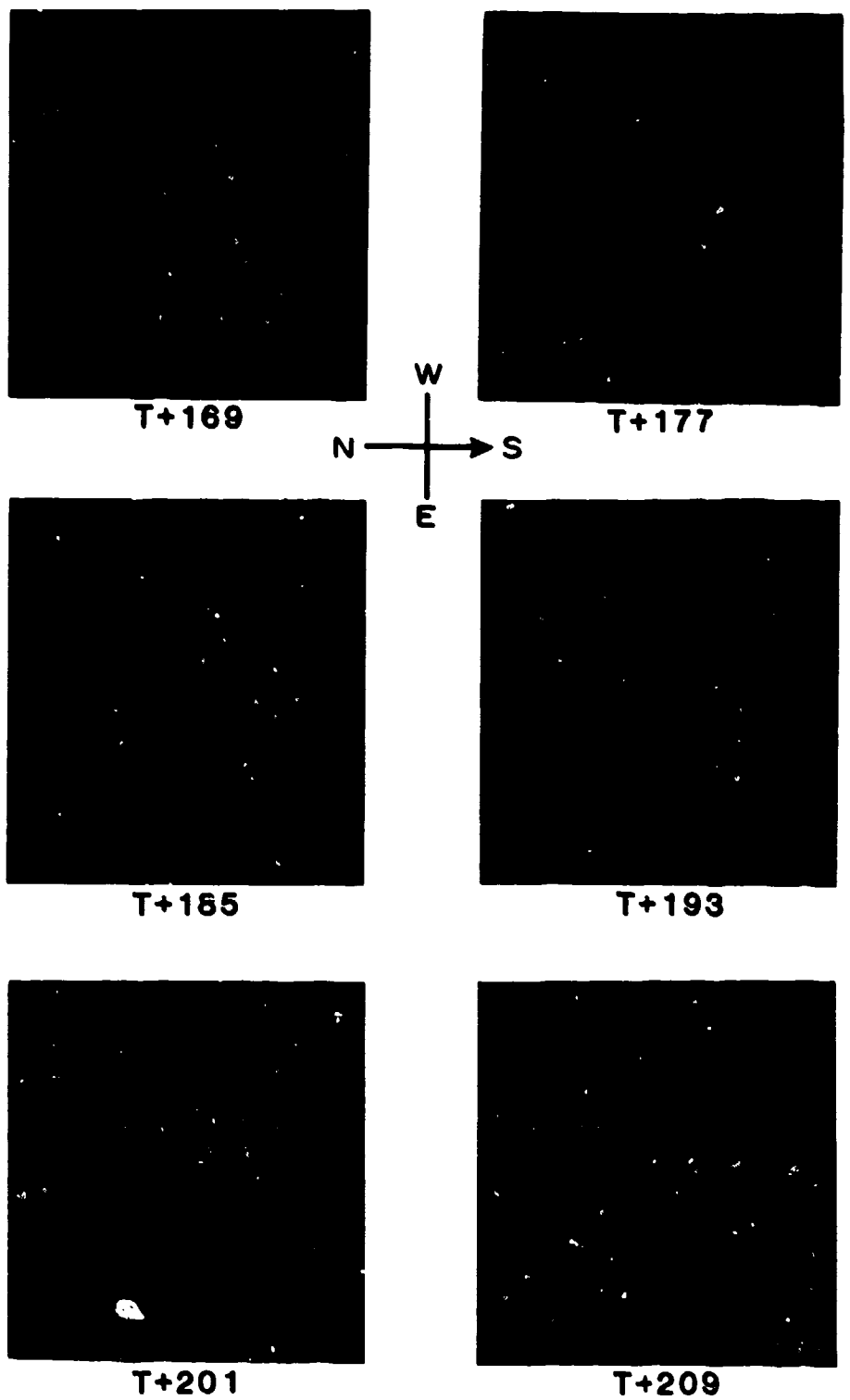


Figure 40. All-sky TV frames at eight-second intervals from T+169 seconds through T+209 seconds.

### MERIDIAN SCANNING PHOTOMETERS

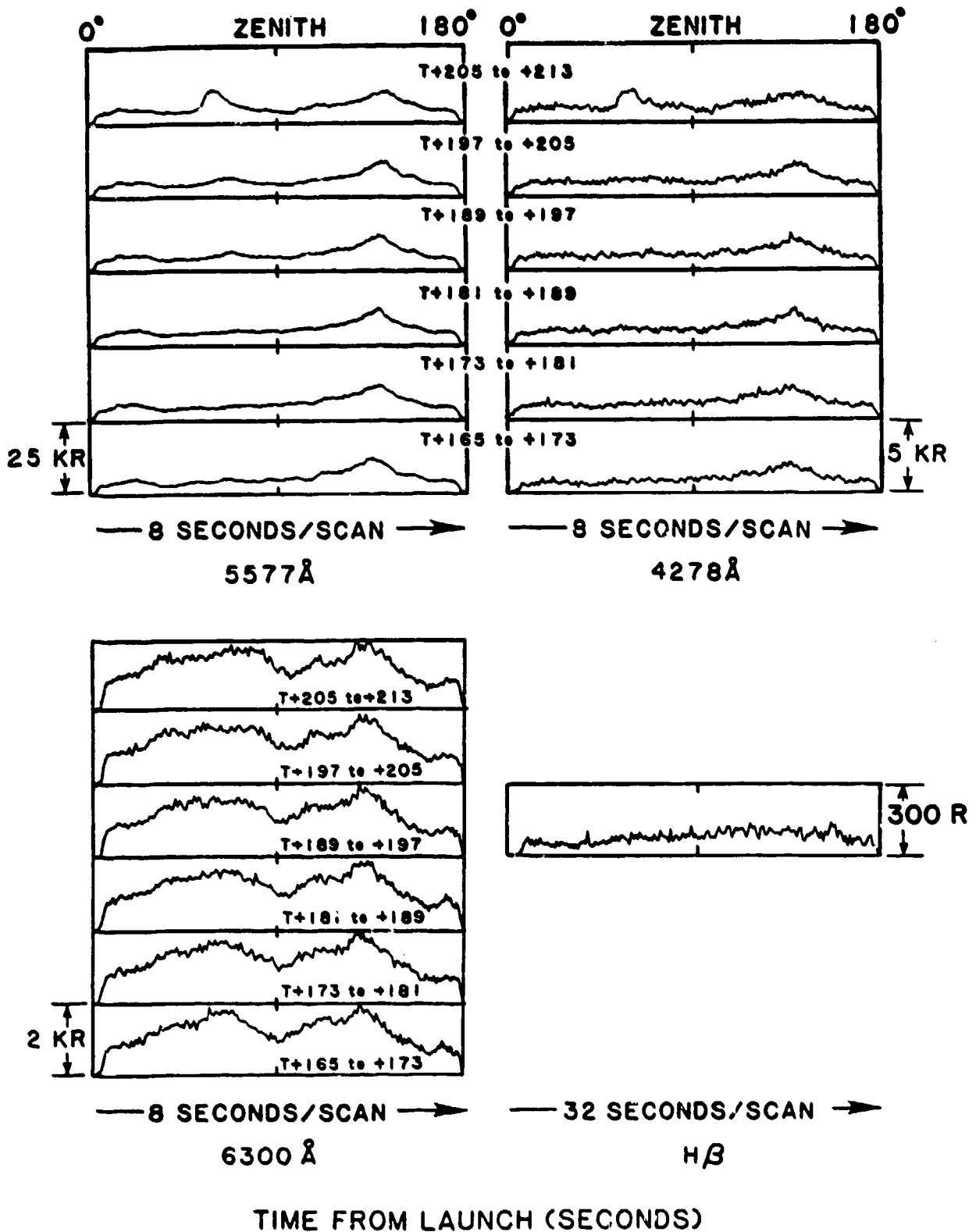
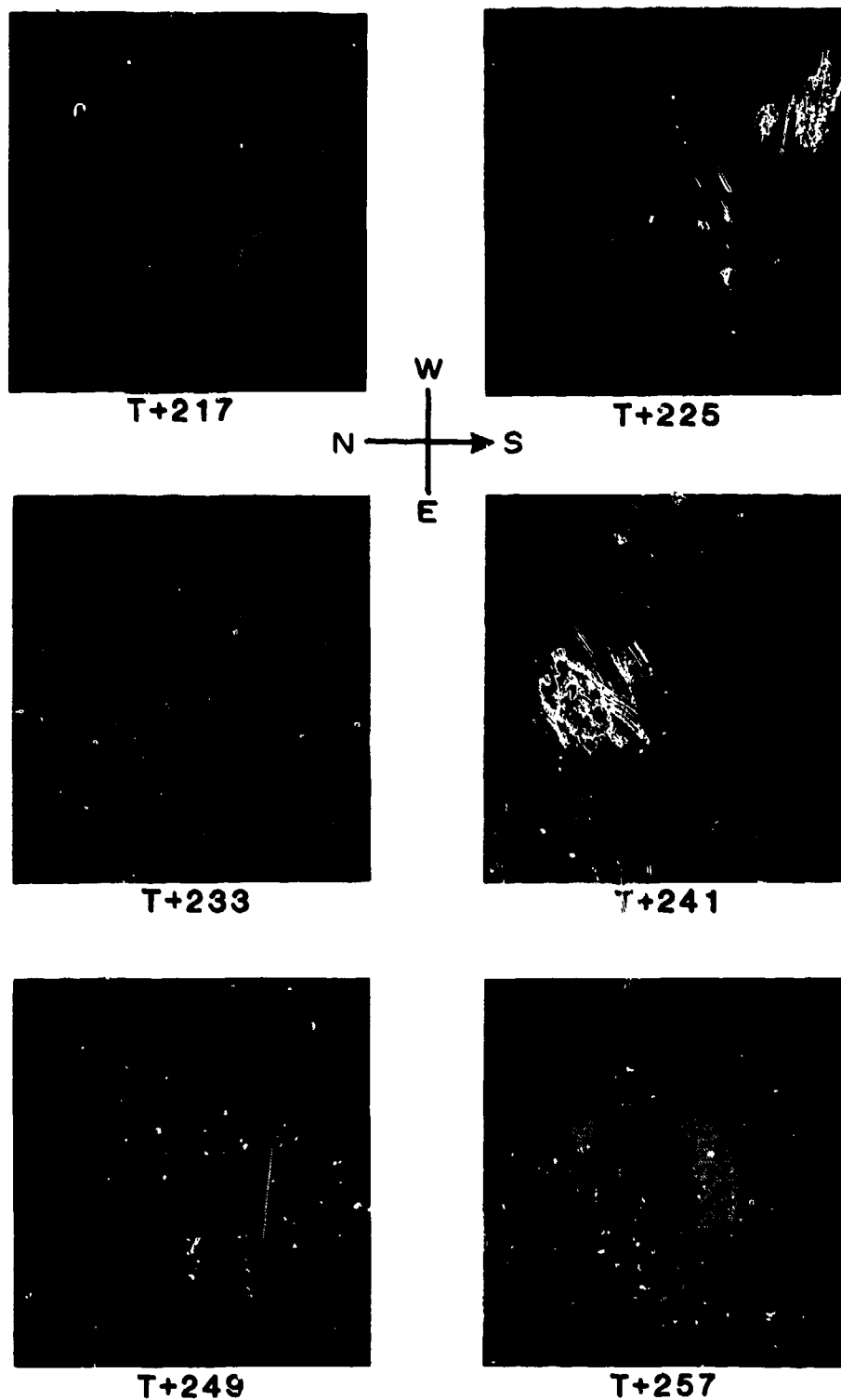


Figure 41. Meridian scanning photometers at 5577 Å, 4278 Å, 6300 Å, and H $\beta$ , for the time period T+165 seconds through T+213 seconds.



**Figure 42.** All-sky TV frames at eight-second intervals from T+217 seconds through T+257 seconds.

### MERIDIAN SCANNING PHOTOMETERS

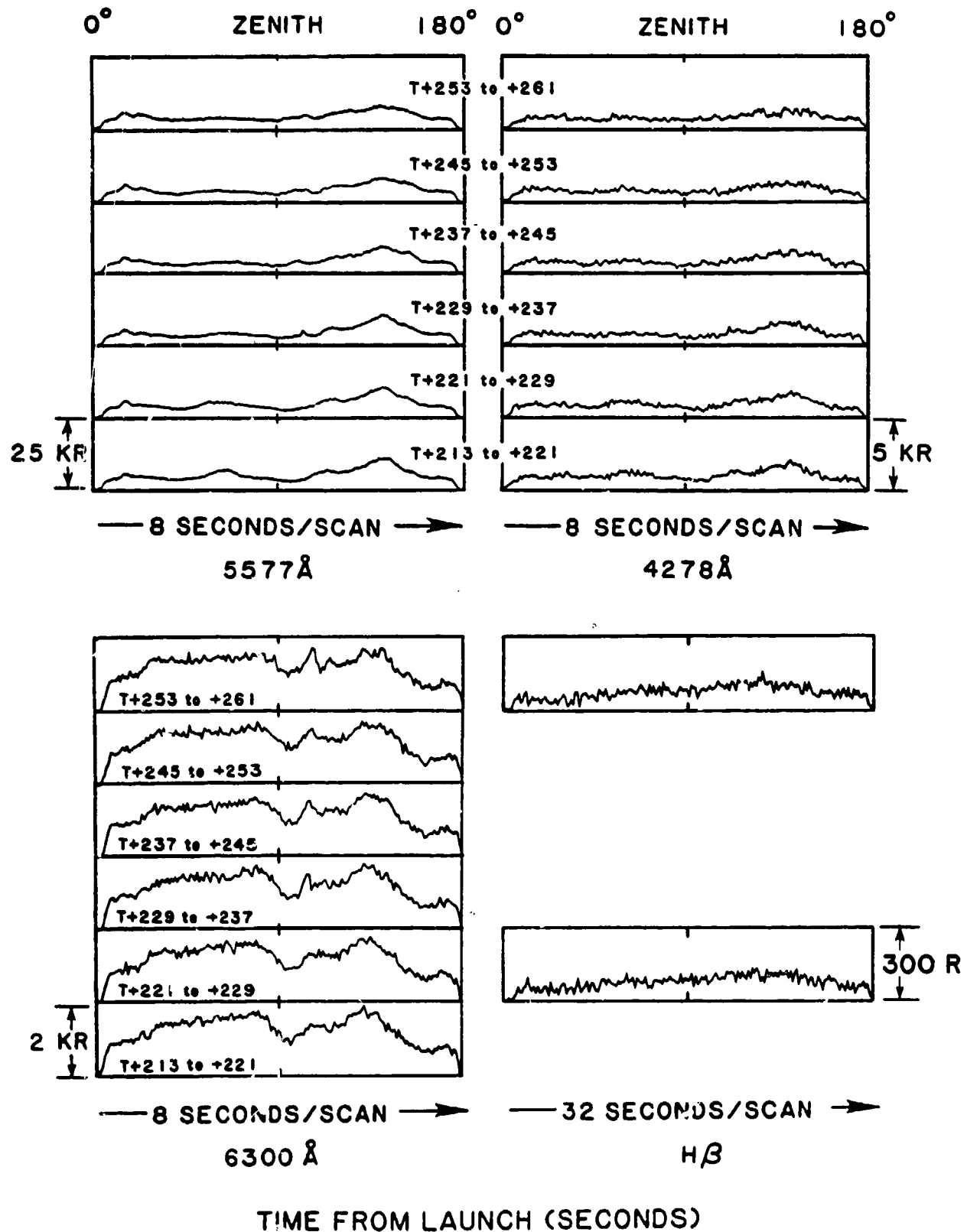


Figure 43. Meridian scanning photometers at 5577 Å, 4278 Å, 6300 Å, and H $\beta$ , for the time period T+213 seconds through T+261 seconds.

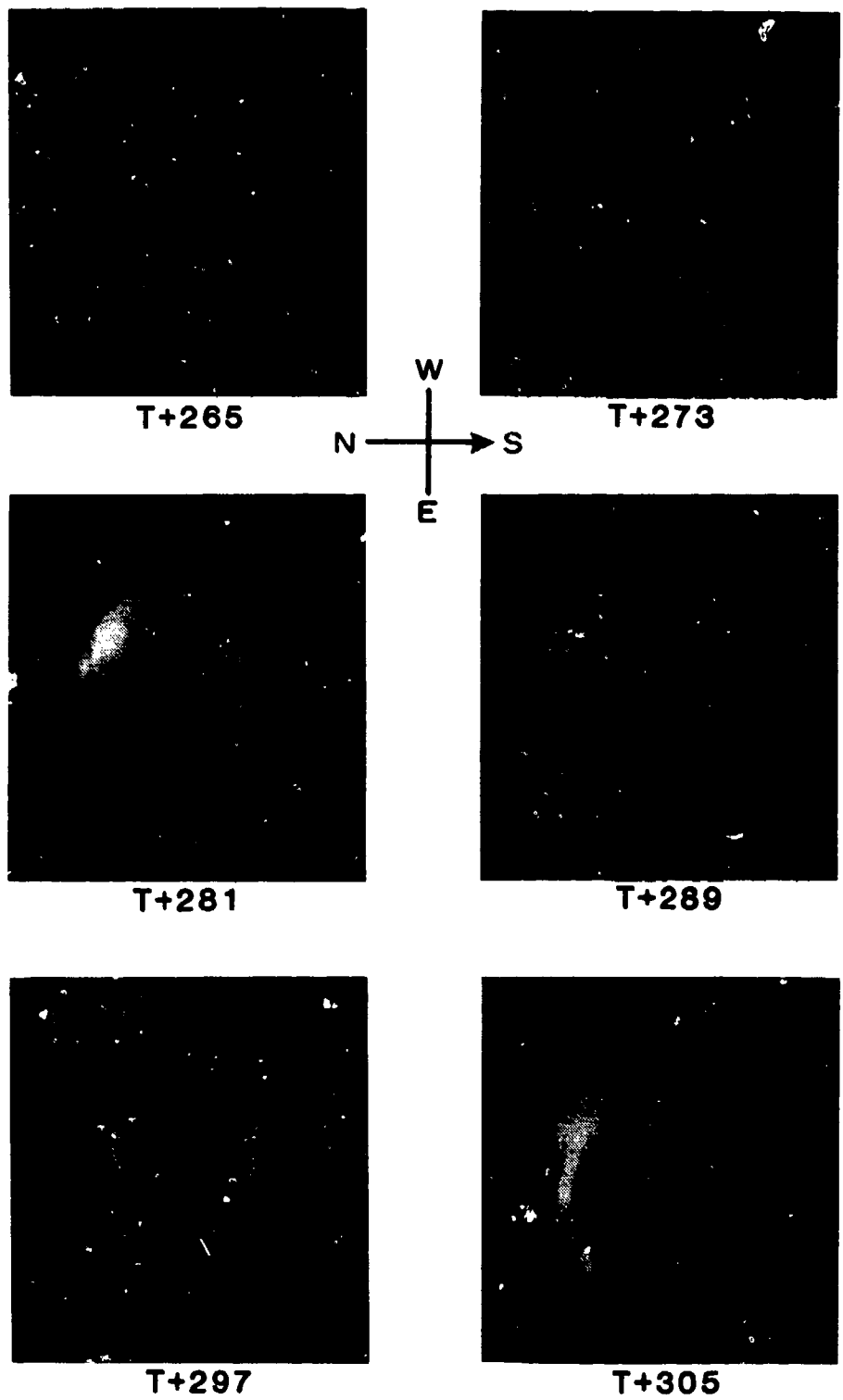


Figure 44. All-sky TV frames at eight-second intervals from T+265 seconds through T+305 seconds.

### MERIDIAN SCANNING PHOTOMETERS

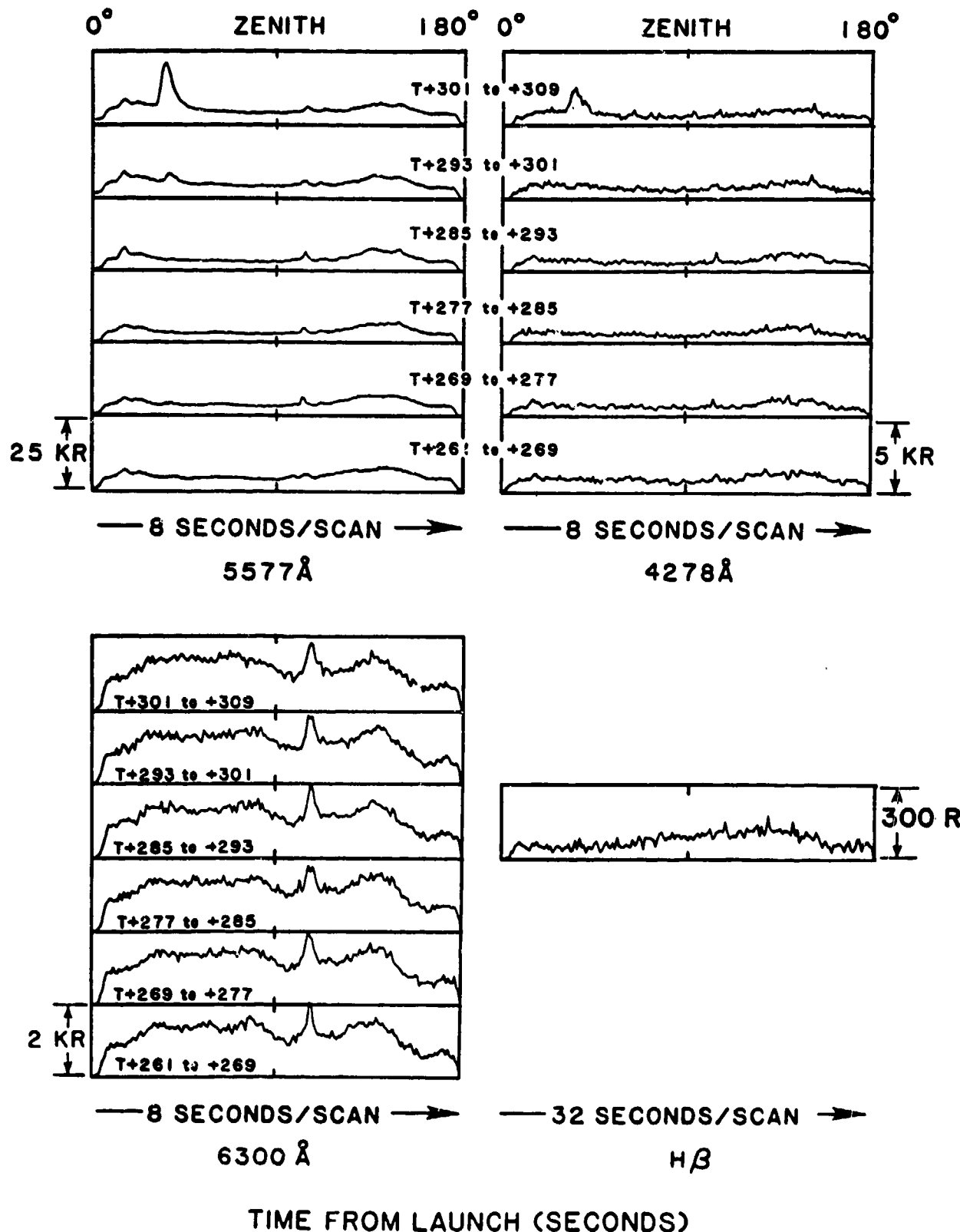


Figure 45. Meridian scanning photometers at 5577 Å, 4278 Å, 6300 Å, and H $\beta$ , for the time period T+261 seconds through T+309 seconds.

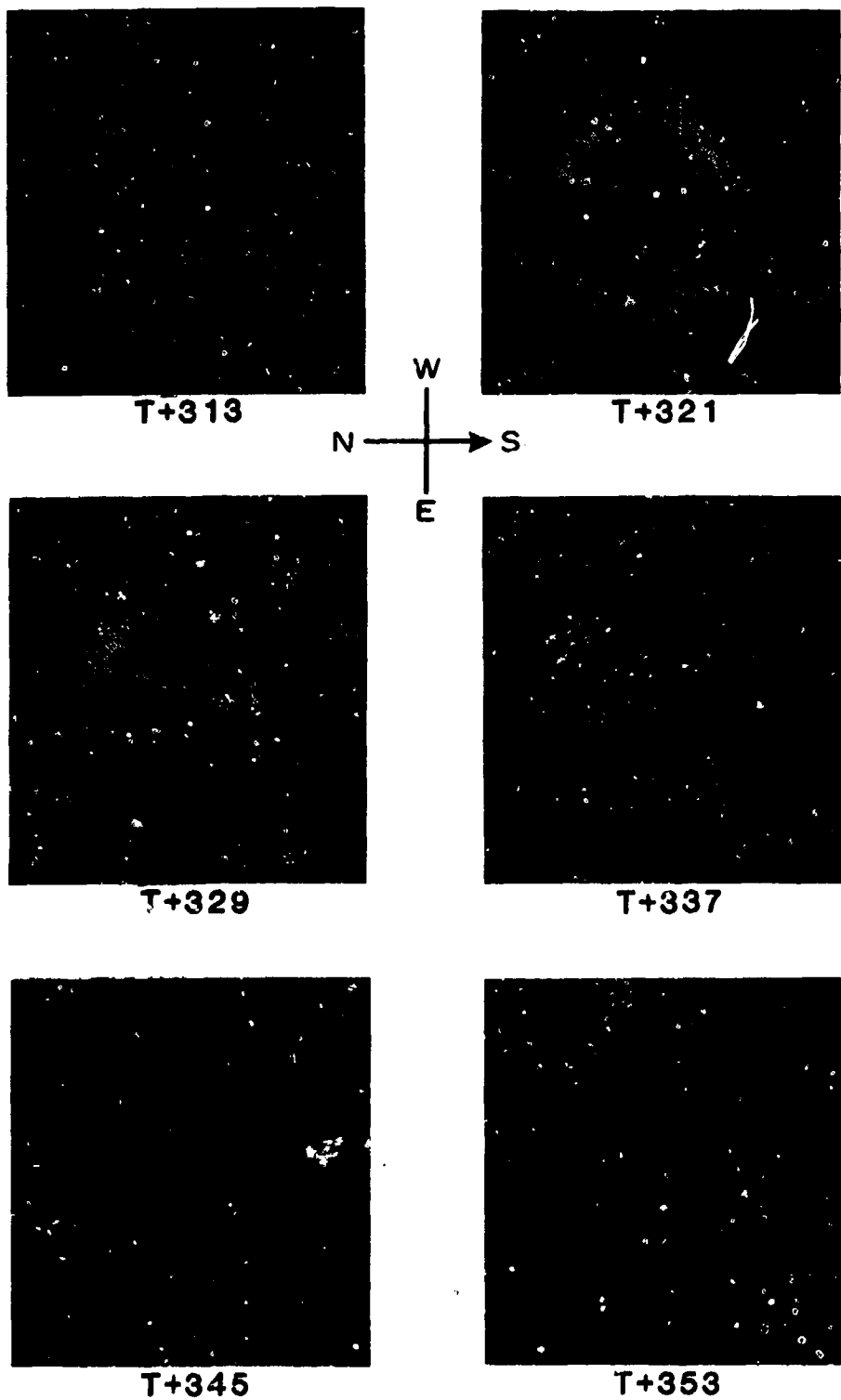


Figure 46. All-sky TV frames at eight-second intervals from T+313 seconds through T+353 seconds.

# MERIDIAN SCANNING PHOTOMETERS

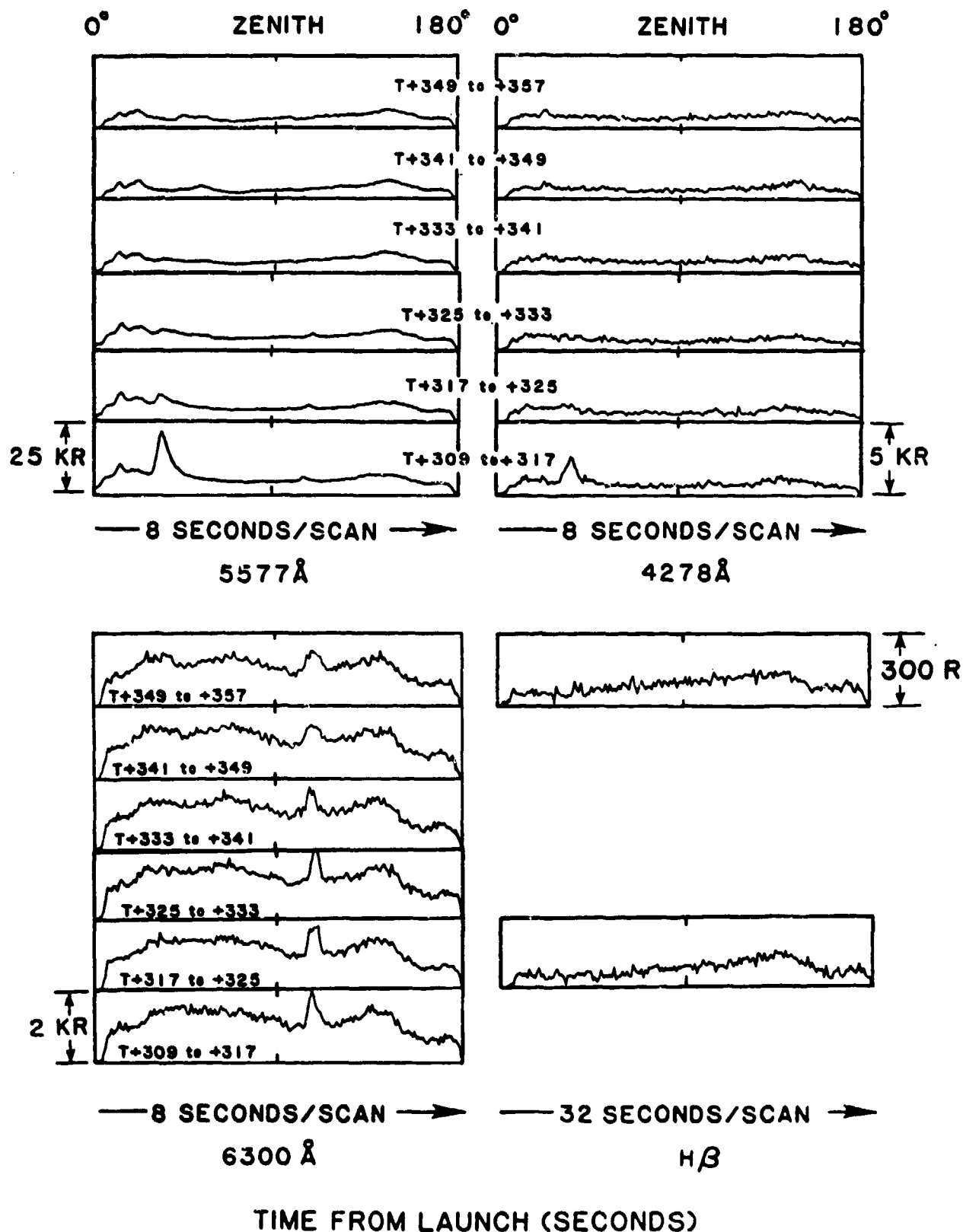


Figure 47. Meridian scanning photometers at 5577 Å, 4278 Å, 6300 Å, and H $\beta$ , for the time period T+309 seconds through T+357 seconds.

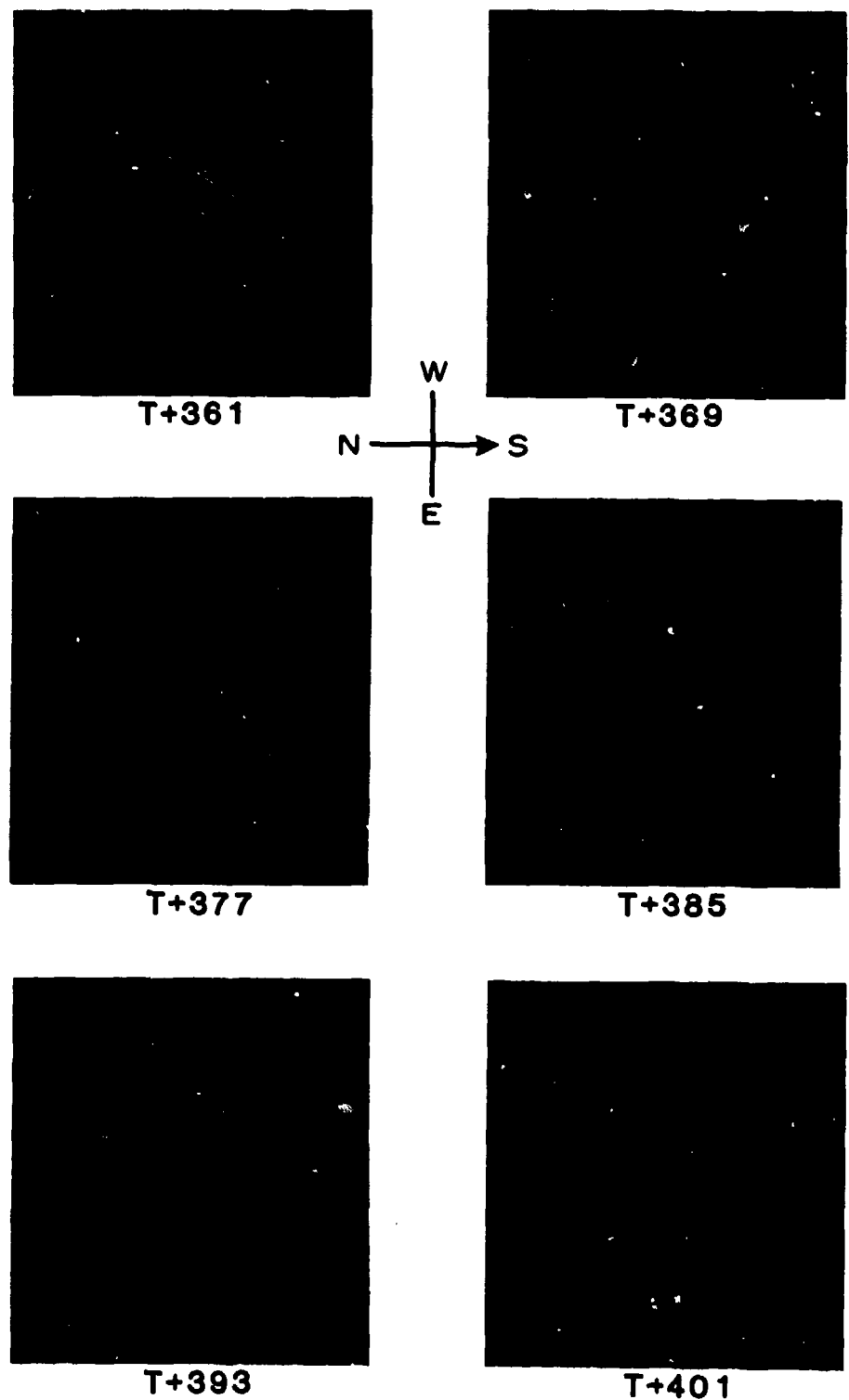


Figure 48. All-sky TV frames at eight-second intervals from T+361 seconds through T+401 seconds.

### MERIDIAN SCANNING PHOTOMETERS

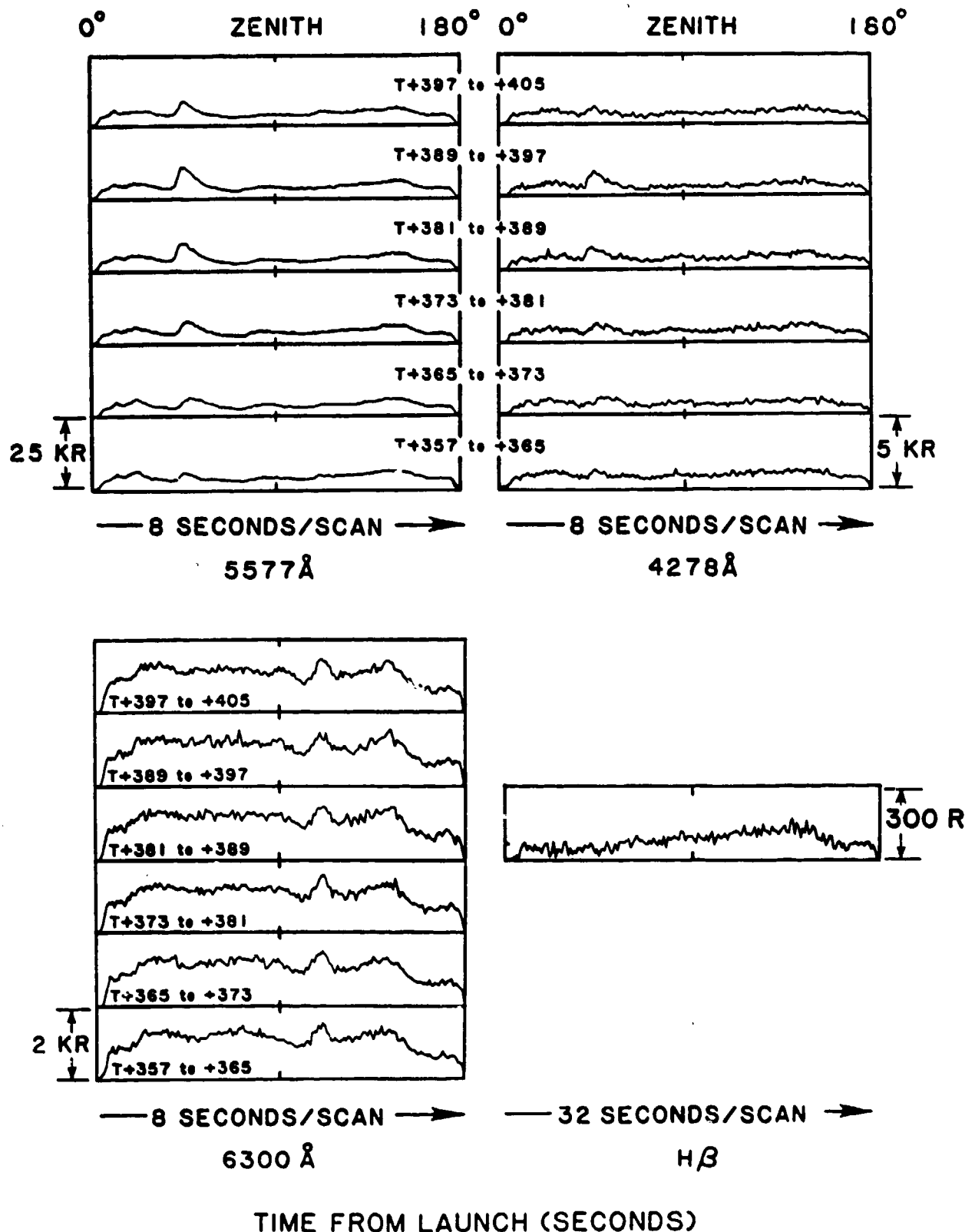
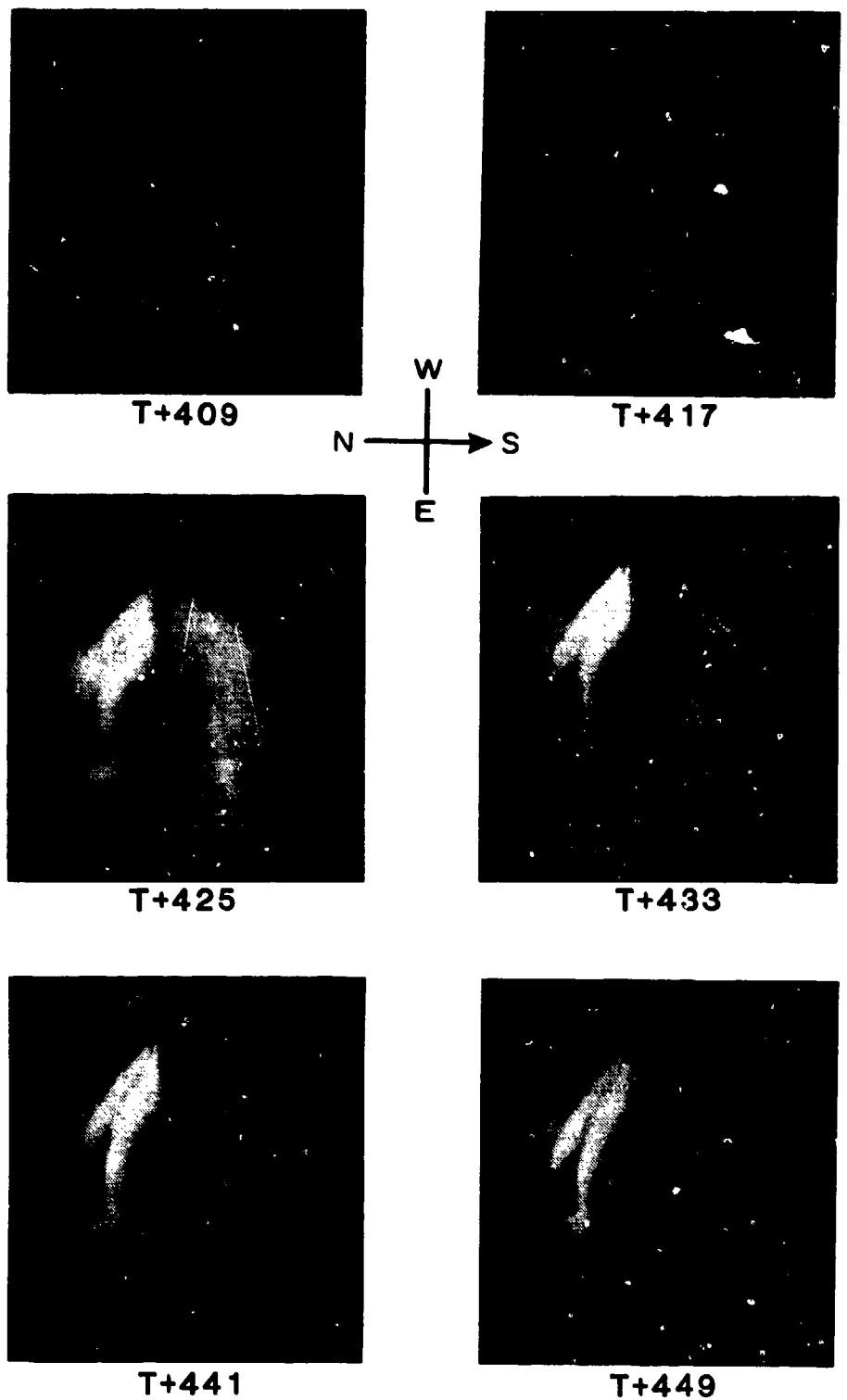


Figure 49. Meridian scanning photometers at 5577 Å, 4278 Å, 6300 Å, and H $\beta$ , for the time period T+357 seconds through T+405 seconds.



**Figure 50.** All-sky TV frames at eight-second intervals from T+409 seconds through T+449 seconds.

### MERIDIAN SCANNING PHOTOMETERS

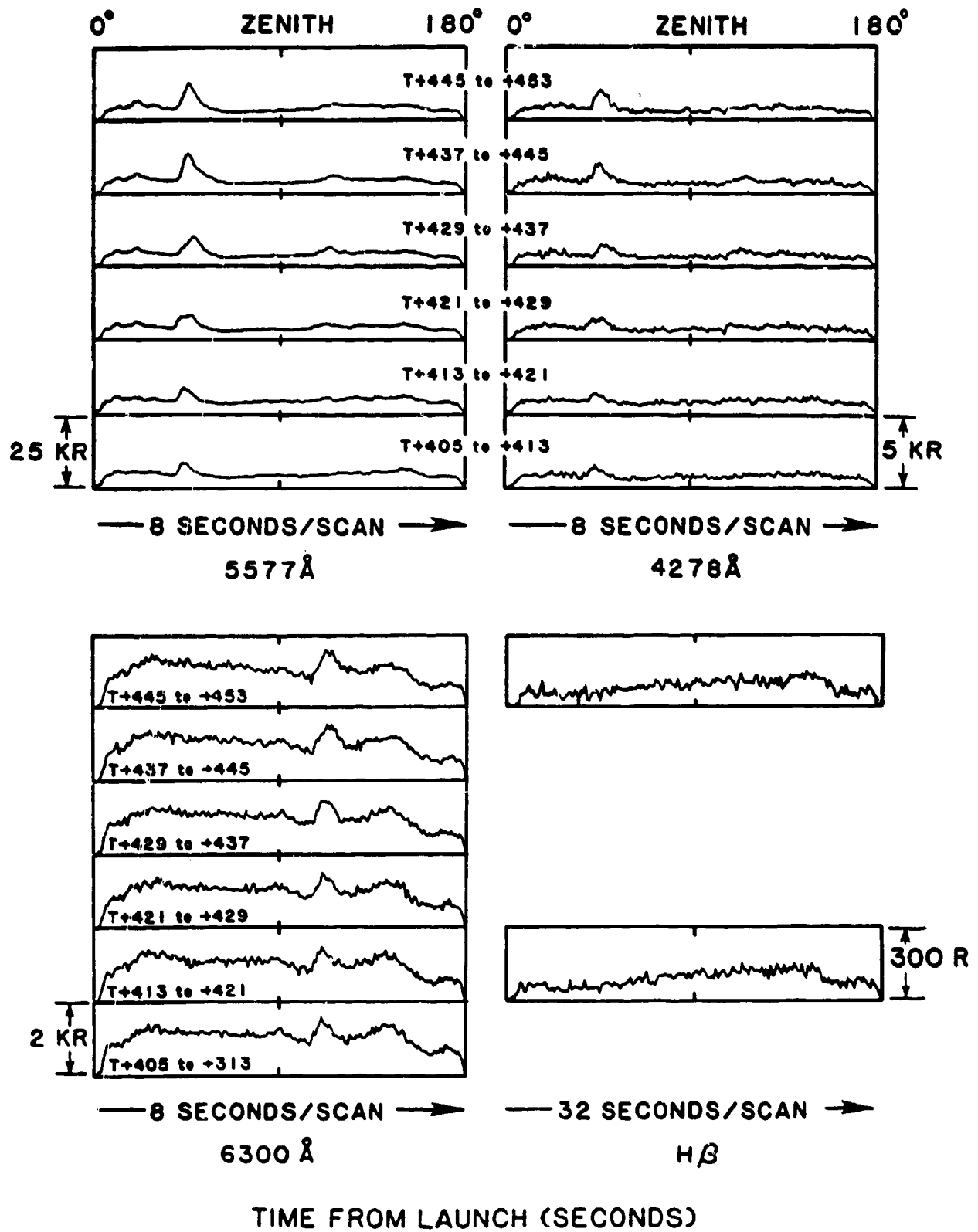


Figure 51. Meridian scanning photometers at 5577 Å, 4278 Å, 6300 Å, and H $\beta$ , for the time period T+405 seconds through T+453 seconds.

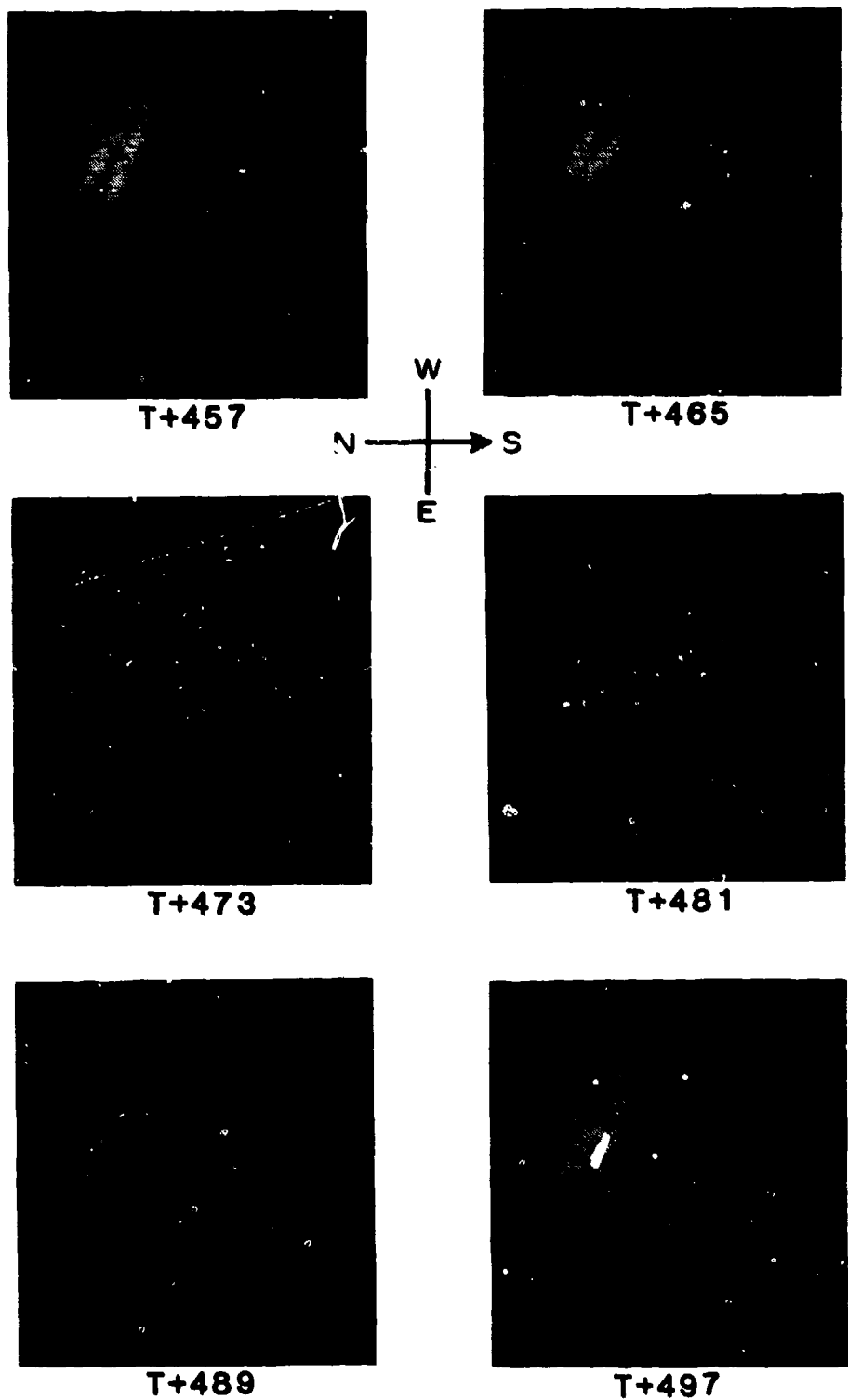


Figure 52. All-sky TV frames at eight-second intervals from T+457 seconds through T+497 seconds.

### MERIDIAN SCANNING PHOTOMETERS

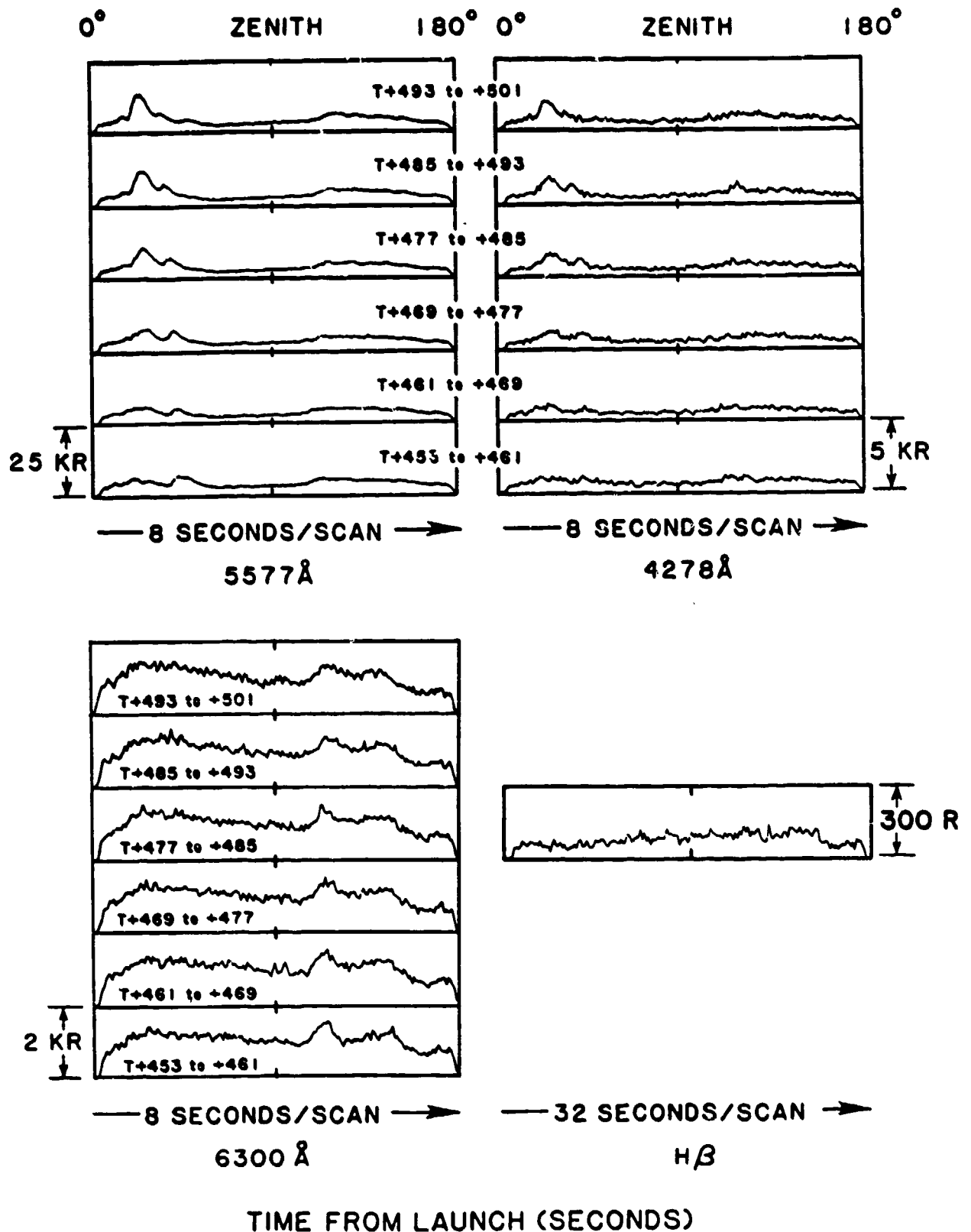


Figure 53. Meridian scanning photometers at 5577 Å, 4278 Å, 6300 Å, and H $\beta$ , for the time period T+453 seconds through T+501 seconds.

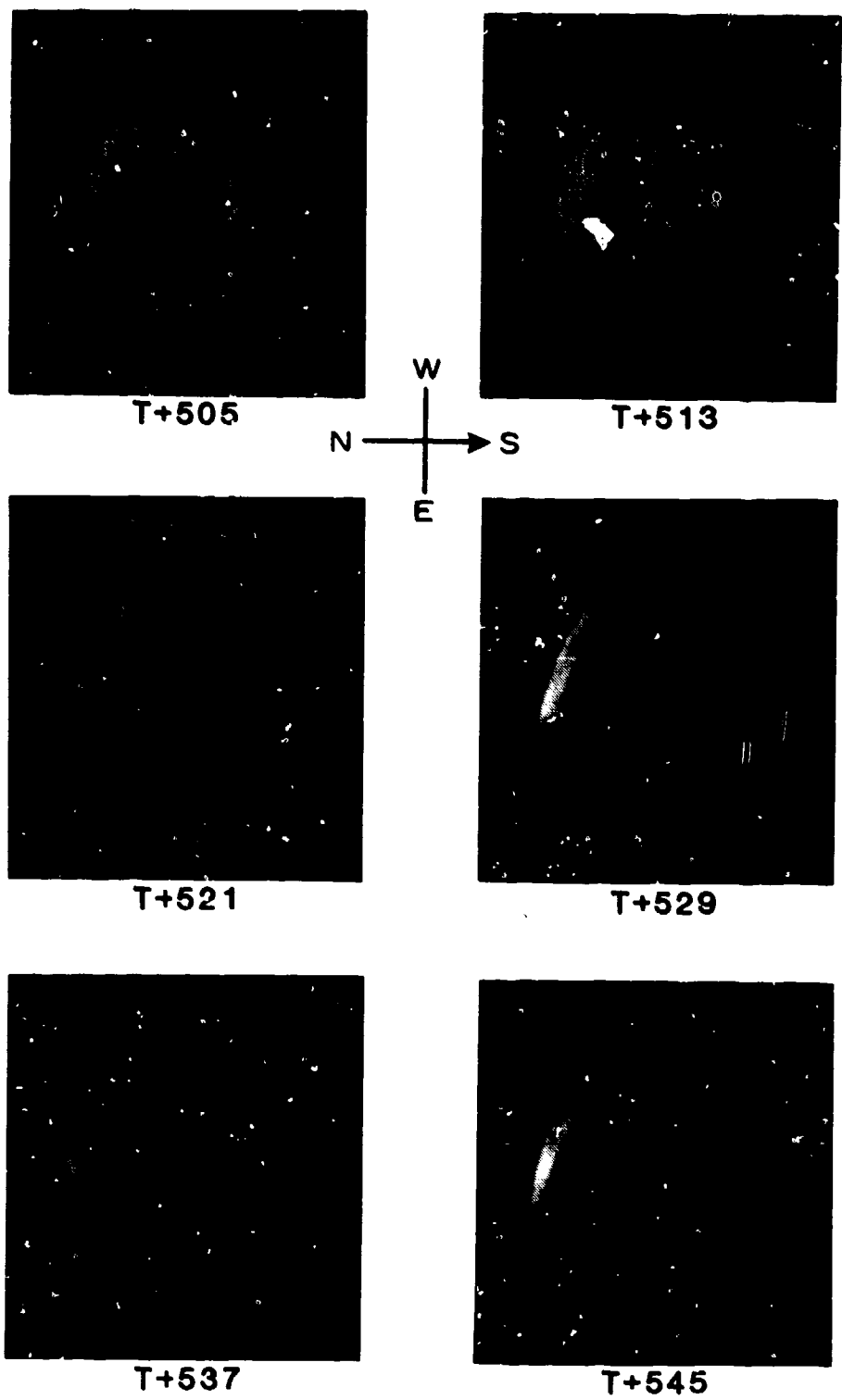


Figure 54. All-sky TV frames at eight-second intervals from T+505 seconds through T+545 seconds.

### MERIDIAN SCANNING PHOTOMETERS

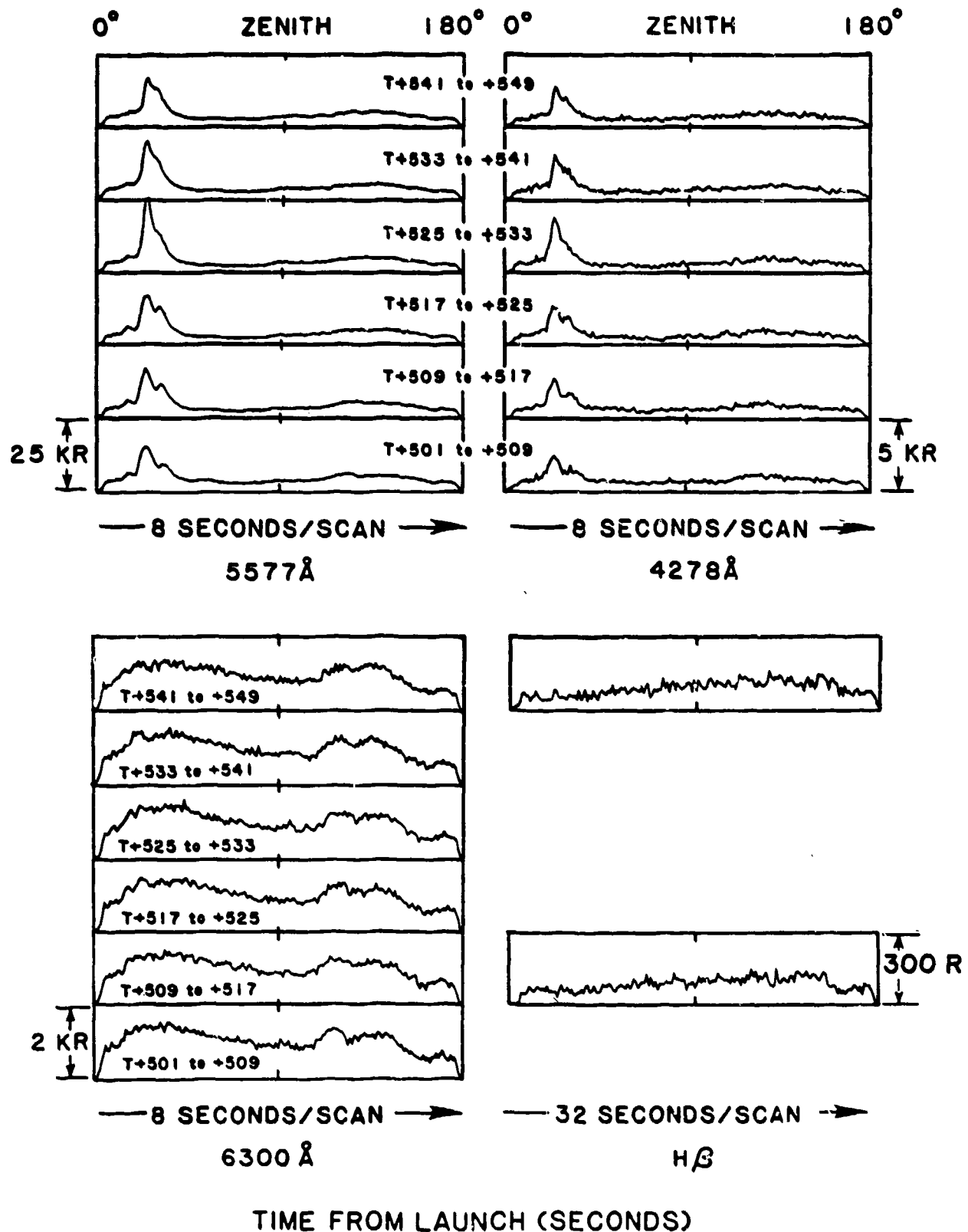
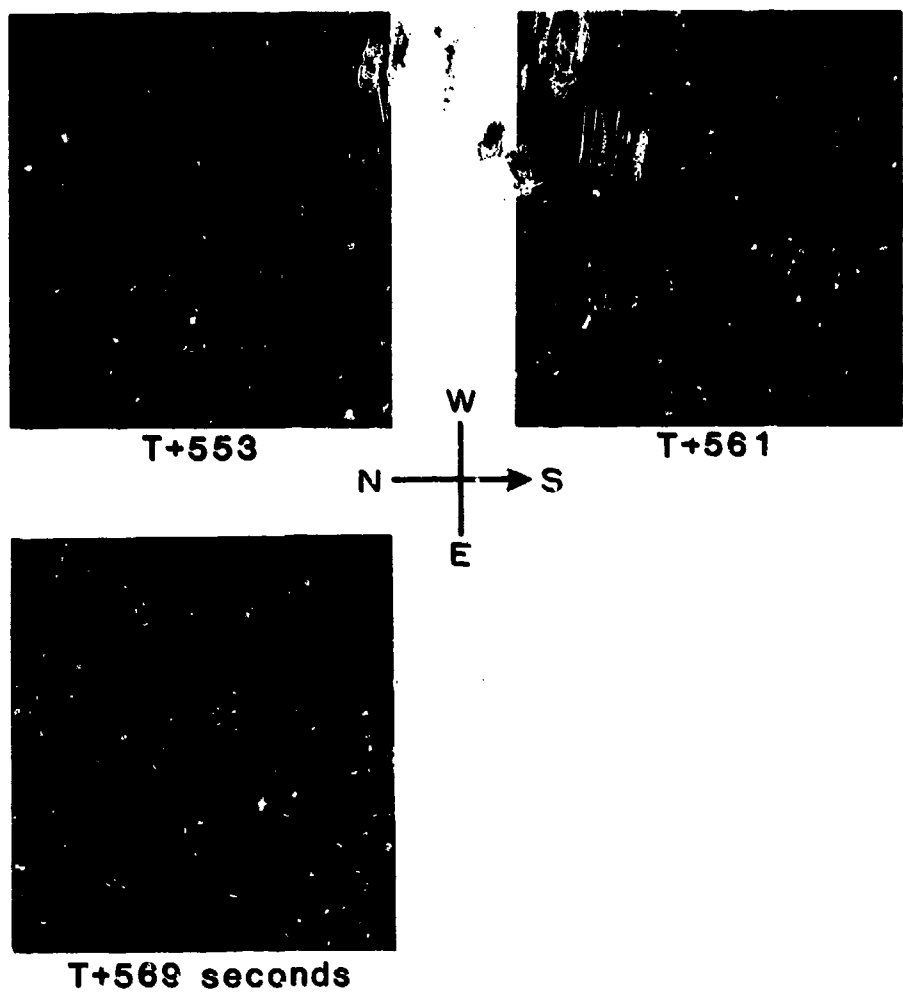


Figure 55. Meridian scanning photometers at 5577 Å, 4278 Å, 6300 Å, and H $\beta$ , for the time period T+501 seconds through T+549 seconds.



**Figure 56.** All-sky TV frames at eight-second intervals from T+553 seconds through T+569 seconds.

### MERIDIAN SCANNING PHOTOMETERS

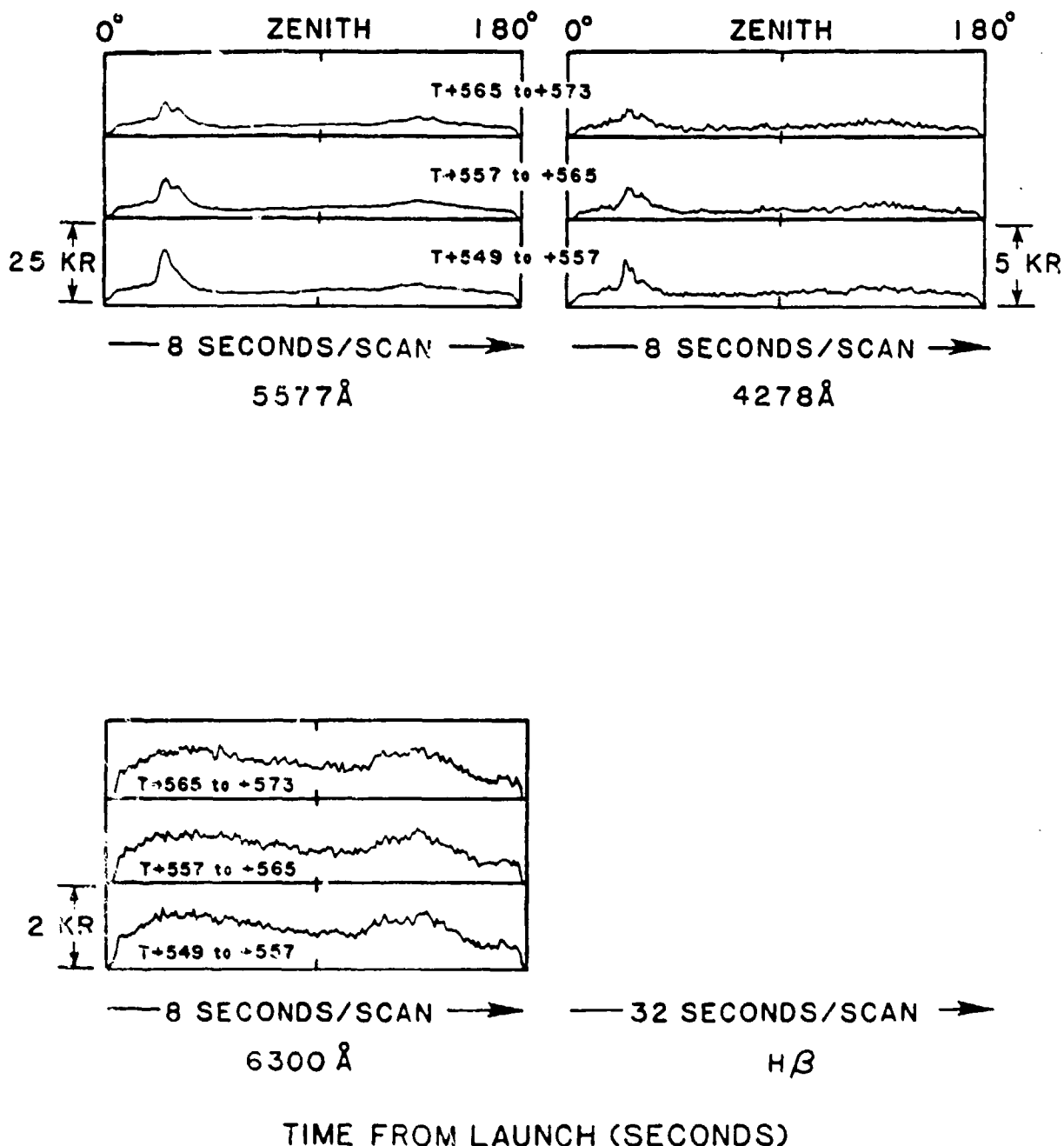


Figure 57. Meridian scanning photometers at 5577 Å, 4278 Å, 6300 Å, and H $\beta$ , for the time period T+549 seconds through T+573 seconds.

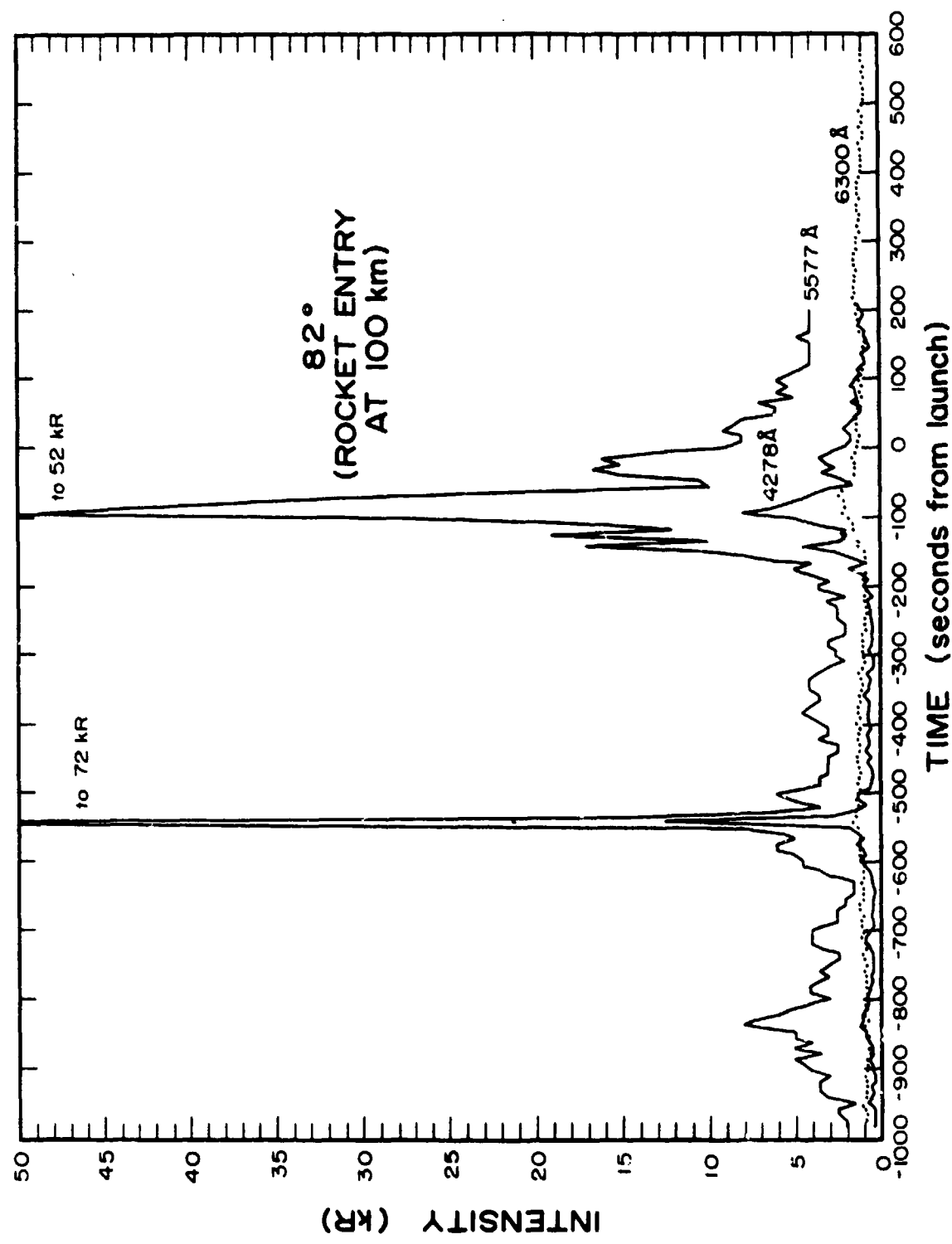


Figure 58. Time history of emission intensity at  $82^\circ$ , the point of rocket entry at 100 km, for 5577 Å, 6300 Å, and 4278 Å.

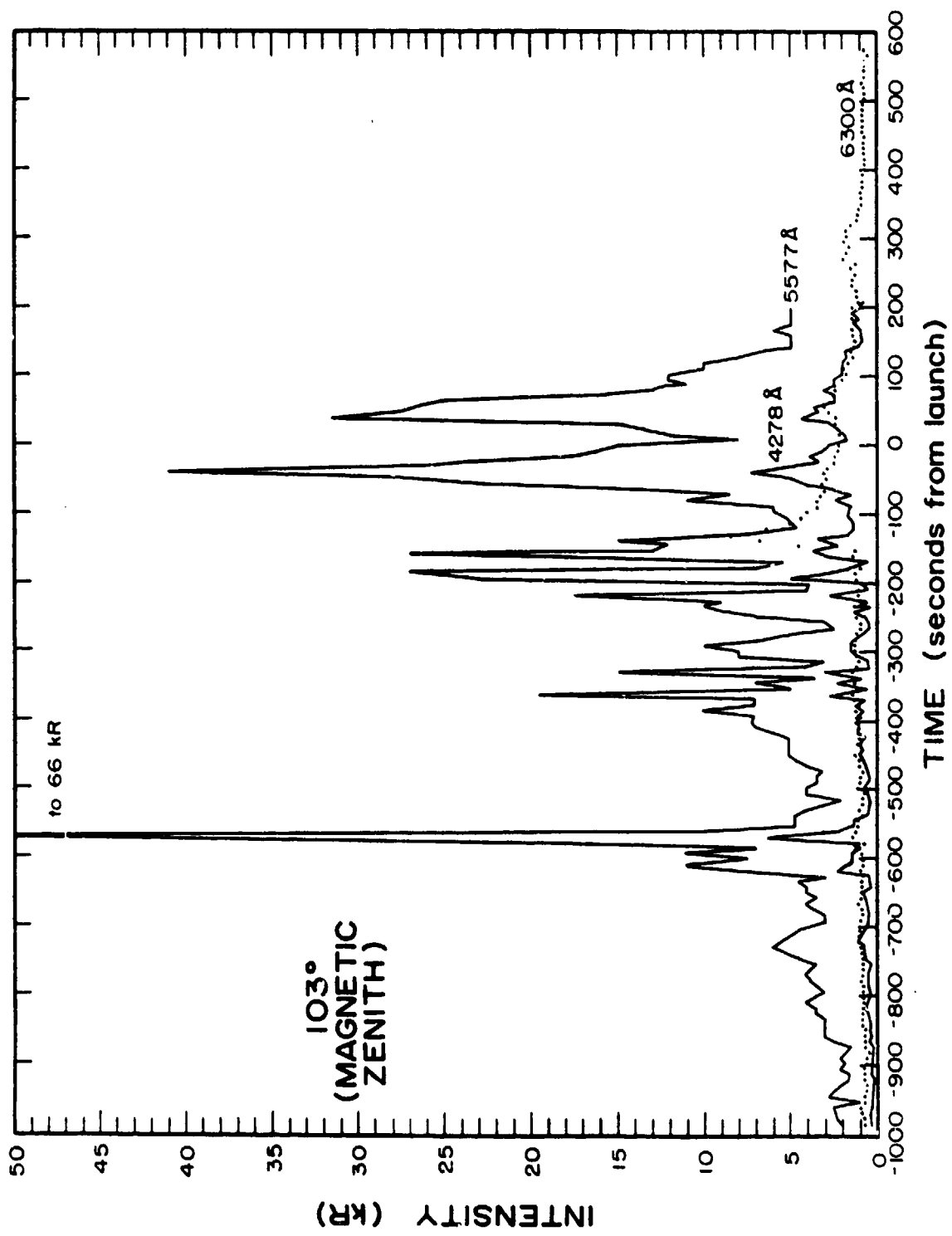


Figure 59. Time history of emission intensity at 103°, the magnetic zenith, for 5577 Å, 6300 Å, and 4278 Å.

This page intentionally left blank.

APPENDIX A  
Atomic Oxygen Detector  
ATOX 83-1

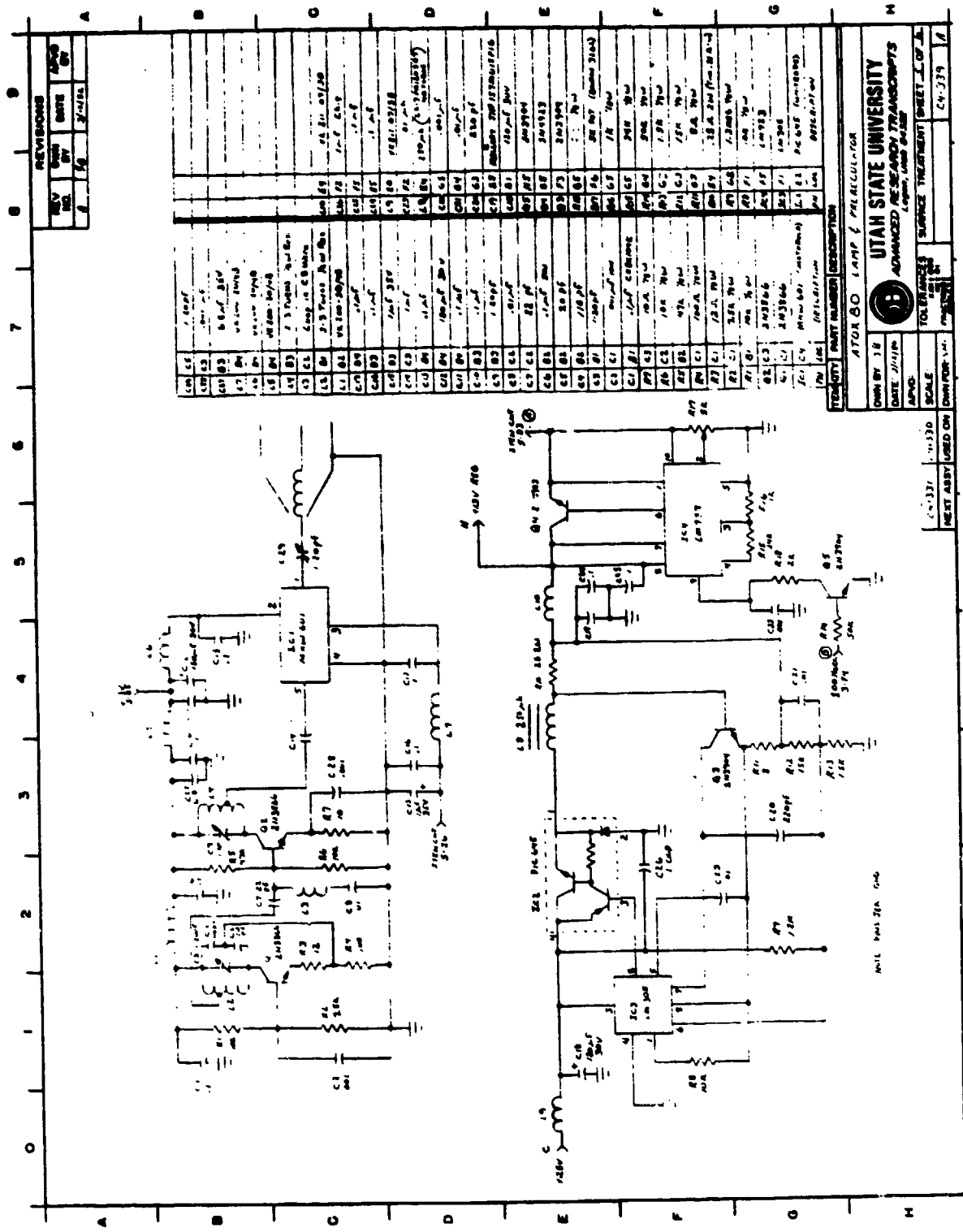


Figure A-1. Atomic Oxygen Detector lamp and preregulator schematic diagram.

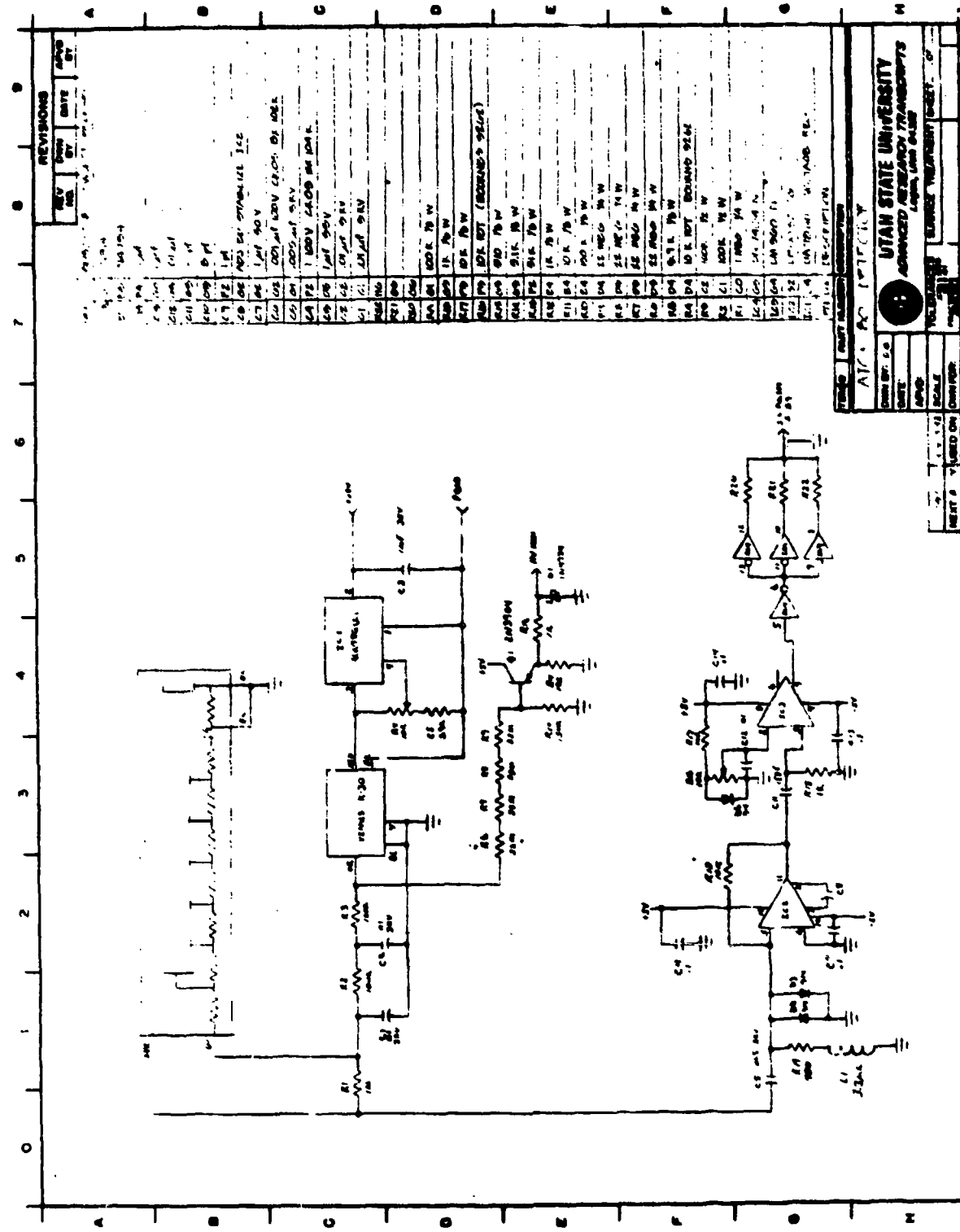


Figure A-2. Atomic Oxygen Detector detector schematic diagram.

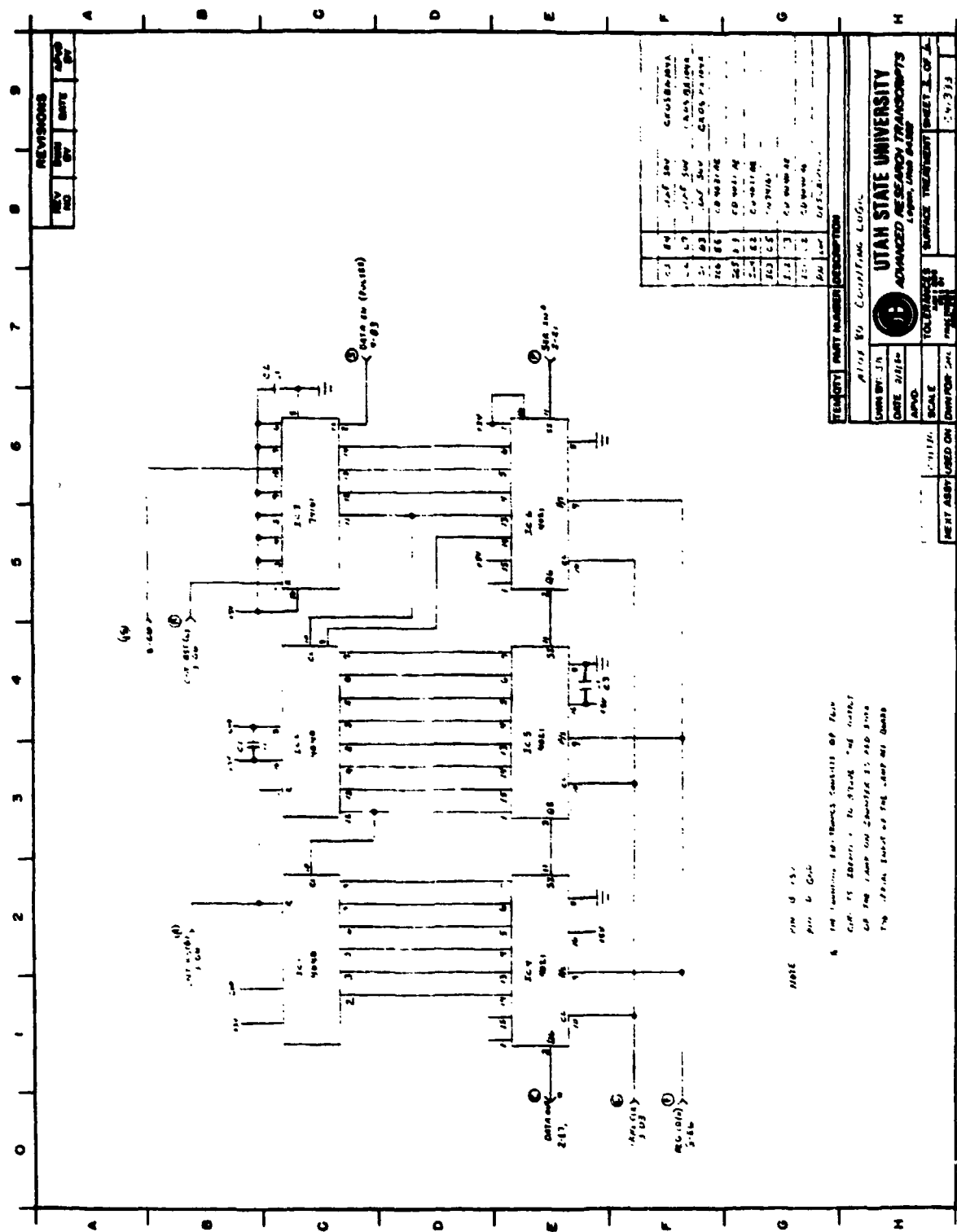


Figure A-3. Atomic Oxygen Detector counting logic schematic diagram.

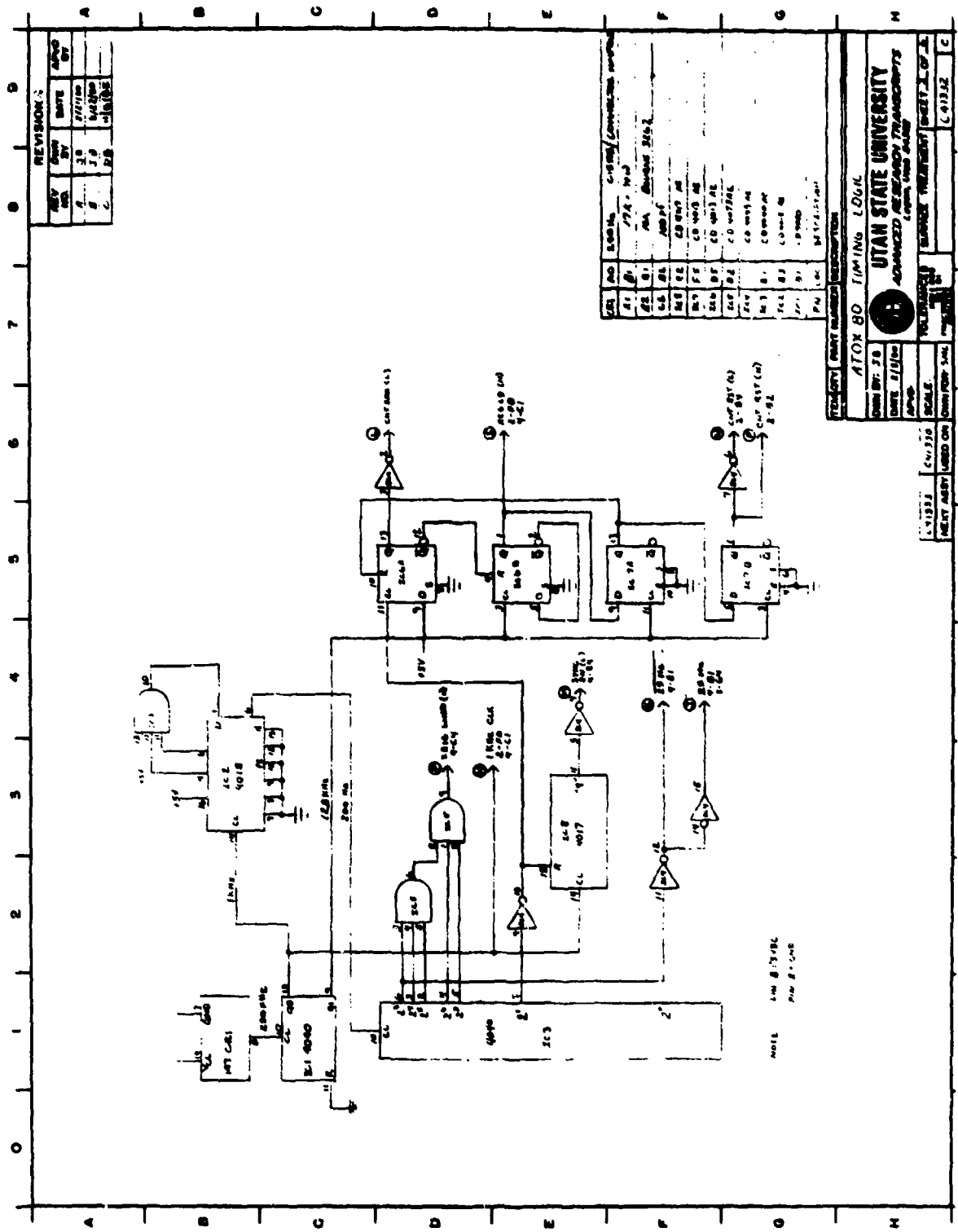
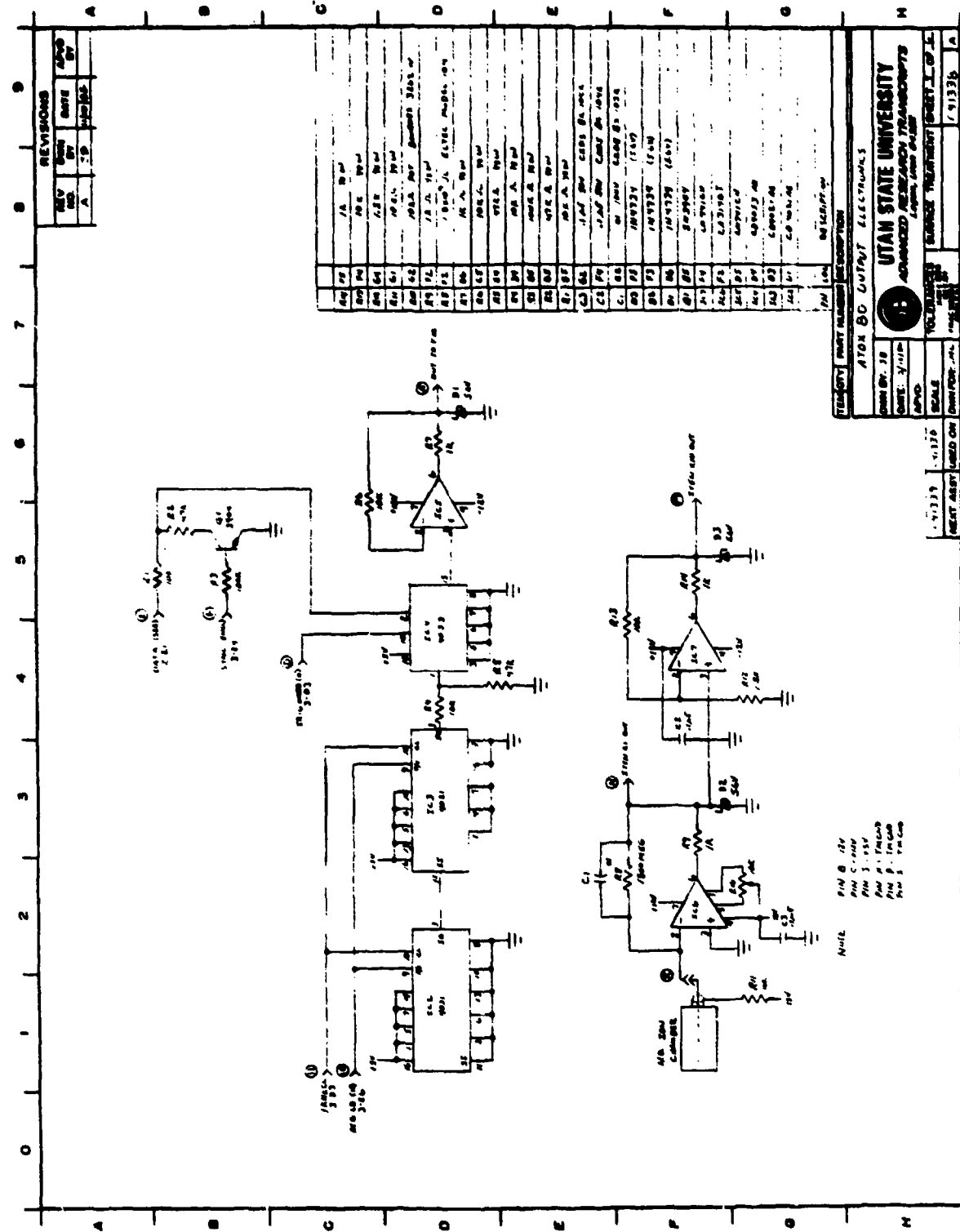
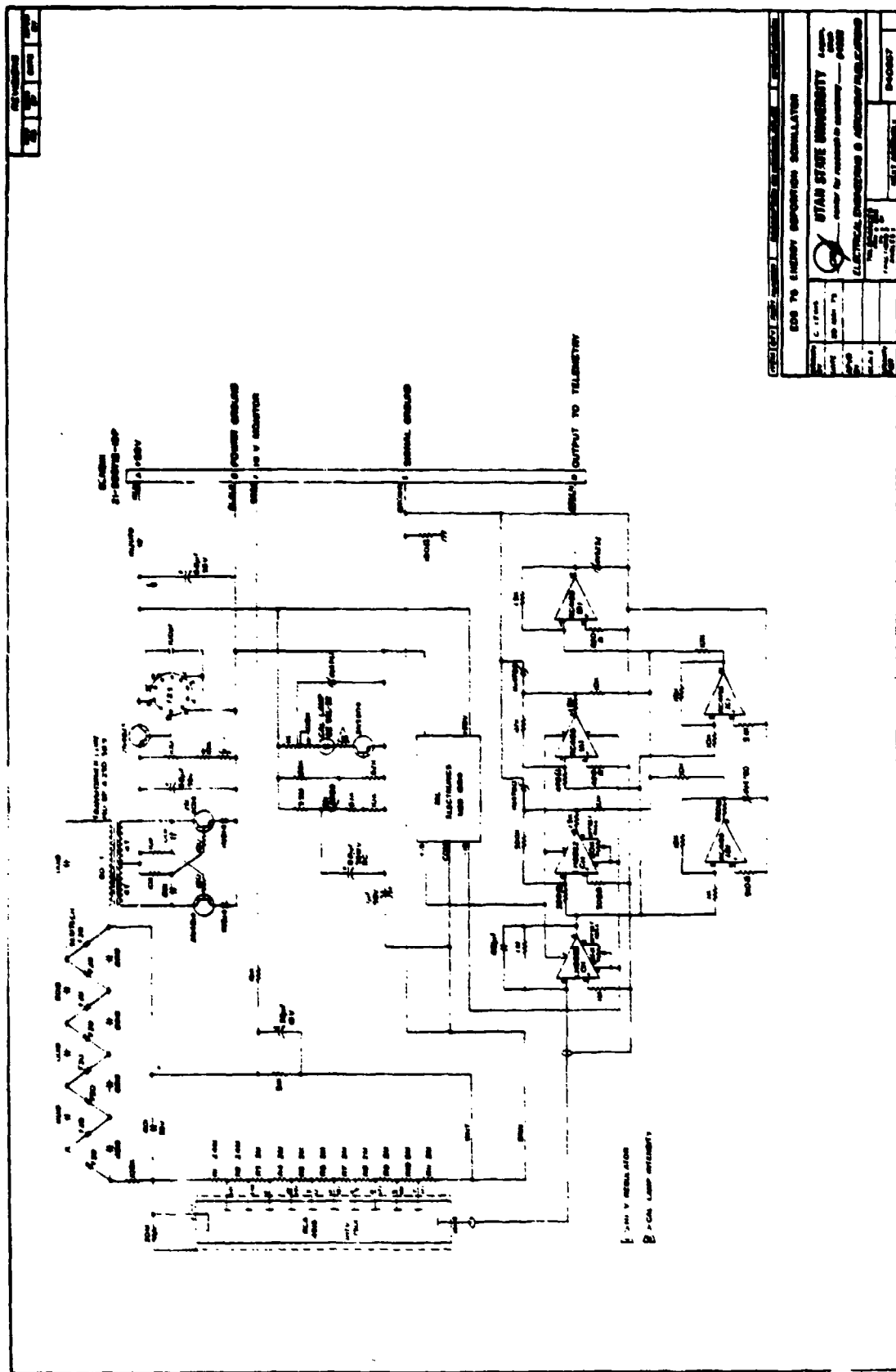


Figure A-4. Atomic Oxygen Detector timing logic schematic diagram.



APPENDIX B  
Energy Deposition Scintillator  
EDS 75-7



**Figure B-1.** Schematic diagram of the Energy Deposition Scintillator.

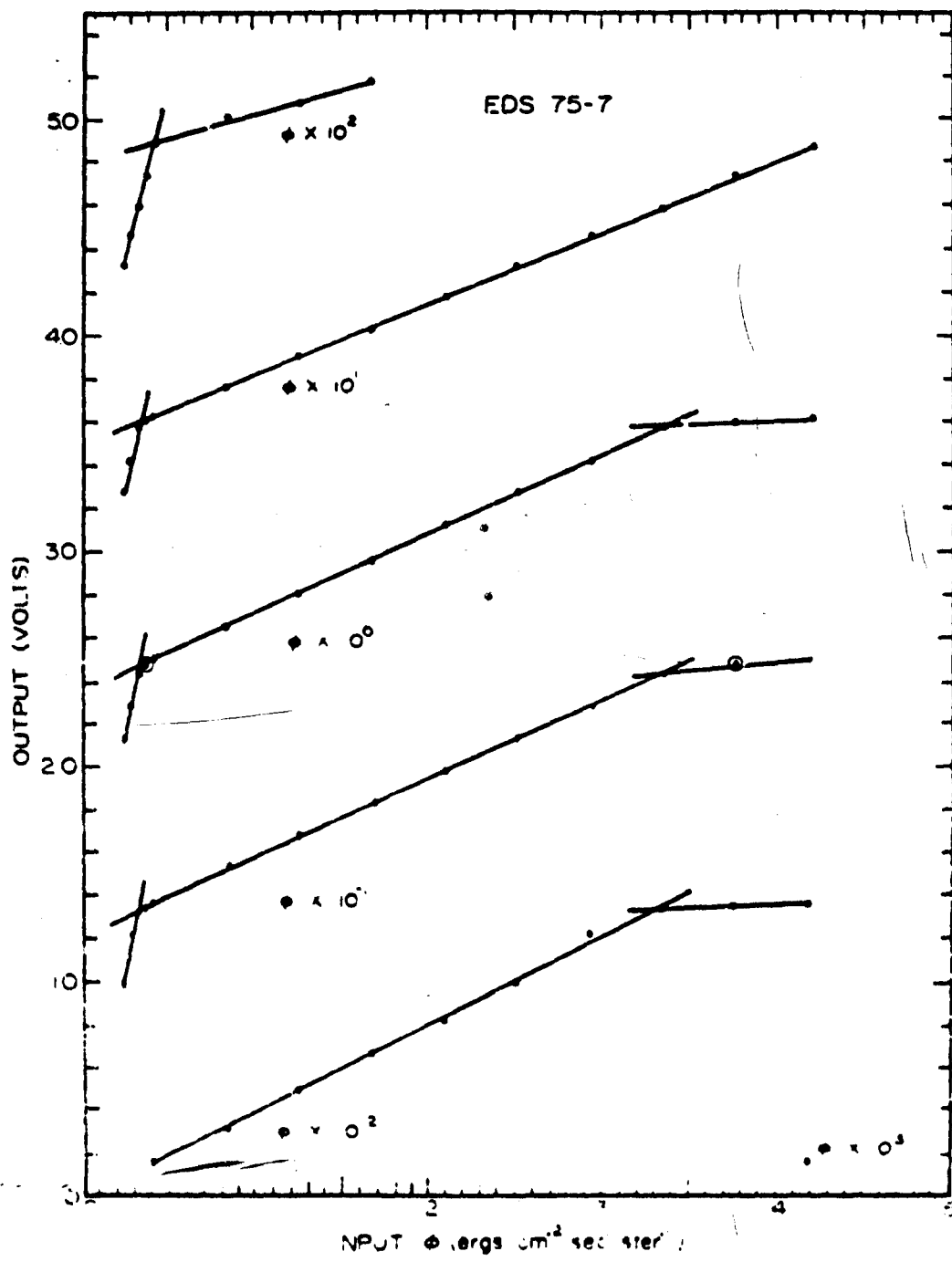


Figure B-2. Input power density versus output voltage calibration for EDS 75-7.

**APPENDIX C**

**Photometers**

**PM2-96  
PM2-99B  
PM2-107B**

A schematic diagram of the model PM2 photometers is included as Figure C-1.

A monitor or the high voltage to the photomultiplier in each photometer assures that the value of this important parameter is known during operation. Table C-1 shows the values measured at the monitors during calibration of the instruments. Figure C-2 is the calibration curve that equates the monitor value to the high voltage actually applied to the photomultiplier and is applicable to all model PM2 units.

One additional characteristic curve is applicable to all of the PM2 photometers included aboard A30.276 and is of interest in considering the optical design of the instruments. This is the light transmission characteristics curve for the flexible fiber optics used to transmit the incoming radiation from the collecting heads situated at the front end of the payload, to the photomultipliers located behind the interferometer. The transmission characteristics are shown in Figure C-3.

Several additional calibration parameters are particular to each photometer and are of value in considering the accumulated data from these sources. Figures C-4 through C-12 include these calibration curves.

TABLE C-1  
High Voltage Monitor Values for A30.276 Photometers

| Photometer S/N | HV Monitor Output |
|----------------|-------------------|
| PM2-96         | +1.84 volts       |
| PM2-998        | +1.65 volts       |
| PM2-107B       | +1.49 volts       |

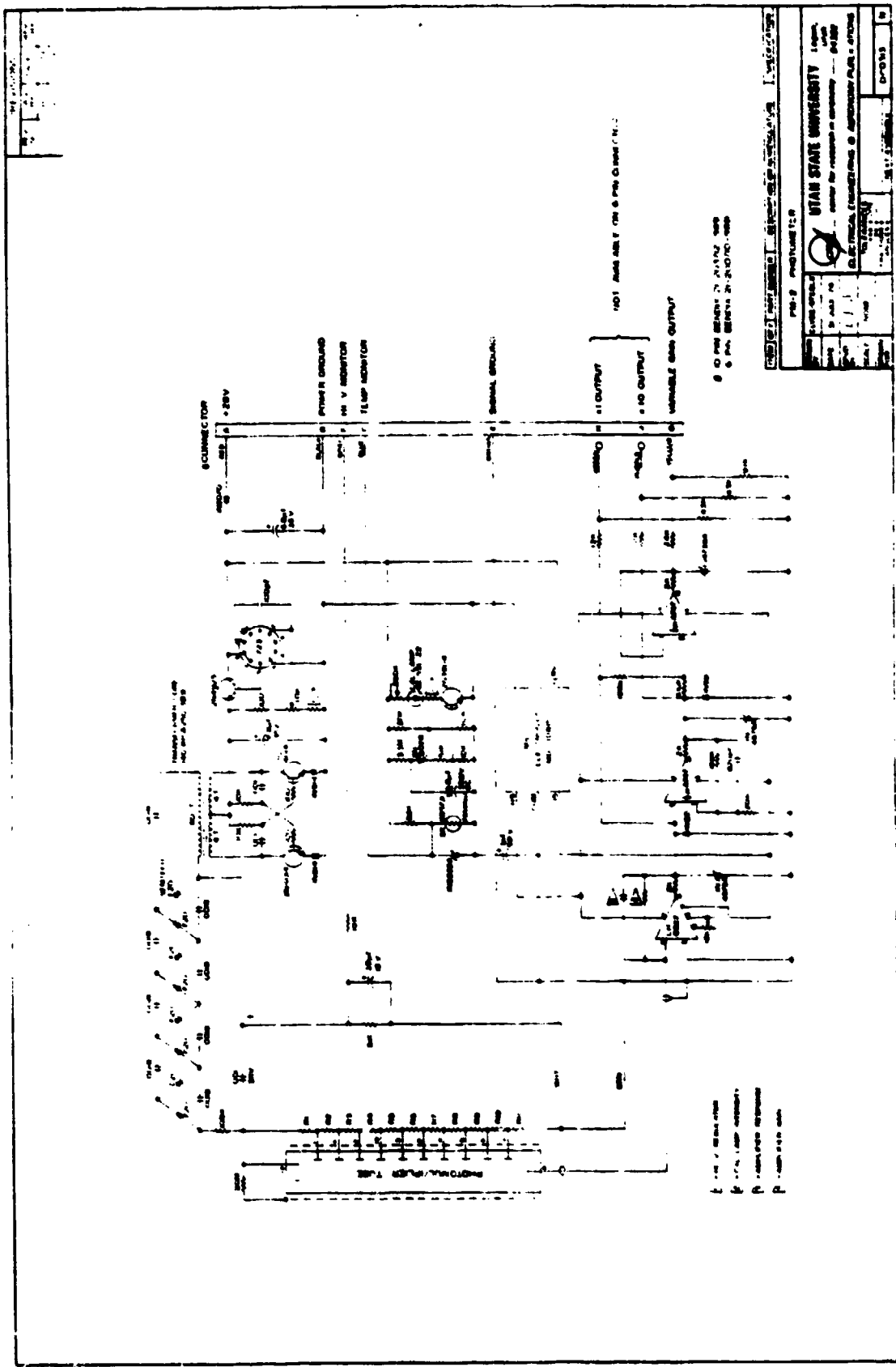


Figure C-1. Schematic diagram of the 3914-1 photometers.

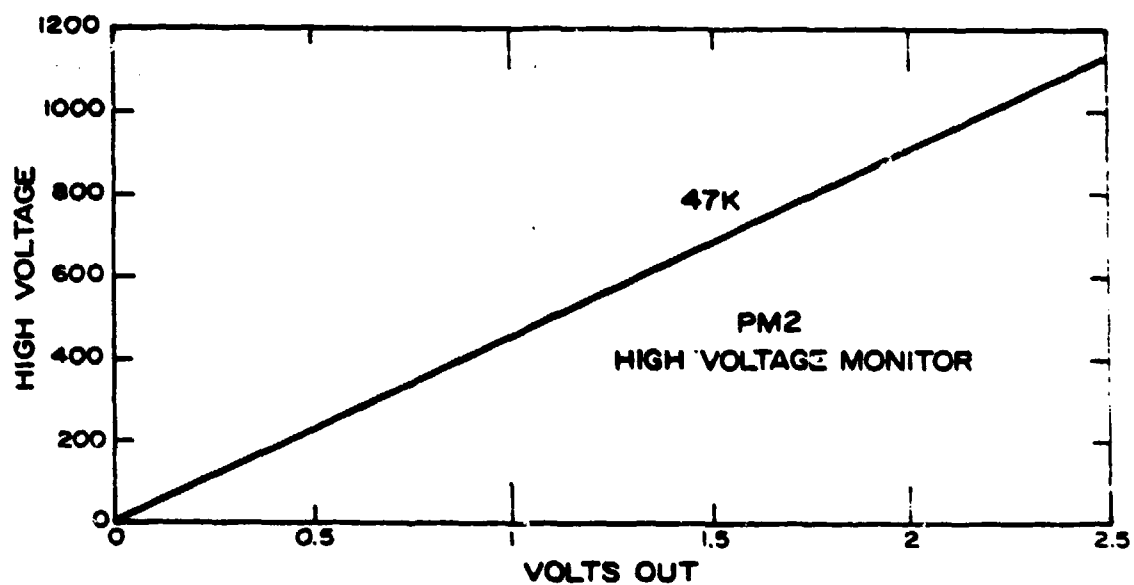


Figure C-2. Photometer high voltage monitor calibration curve.

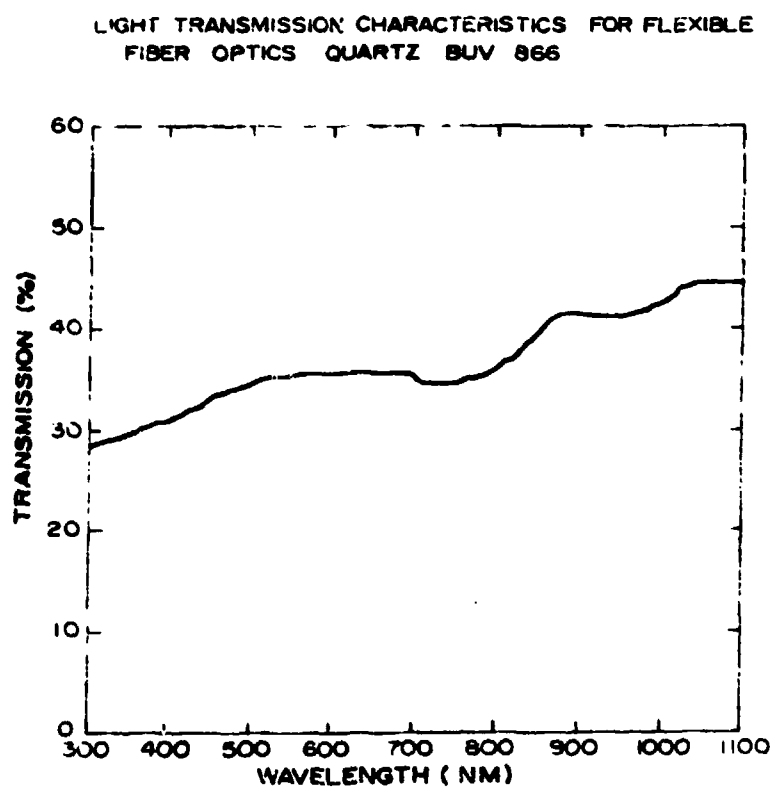


Figure C-3. Light transmission characteristics for flexible fiber optics used as light pipes for the photometers.

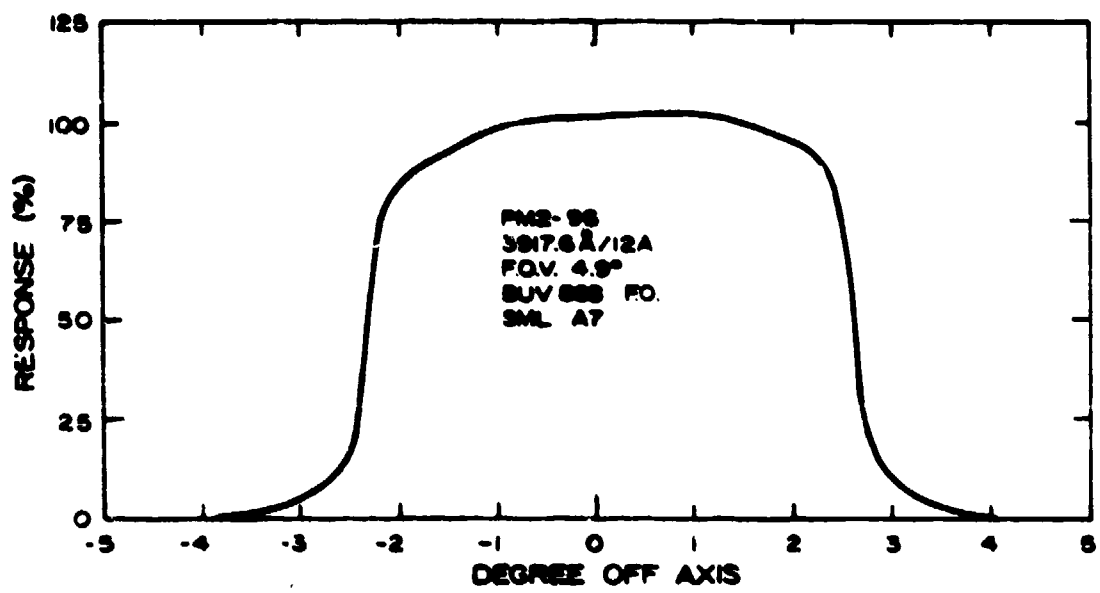


Figure C-6. Photometer PM2-96 field of view.

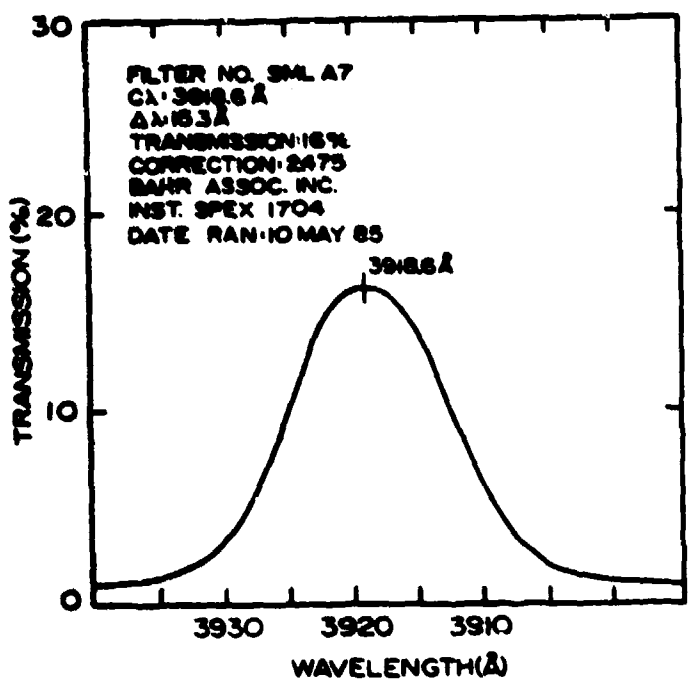


Figure C-5. Photometer PM2-96 filter transmission characteristics.

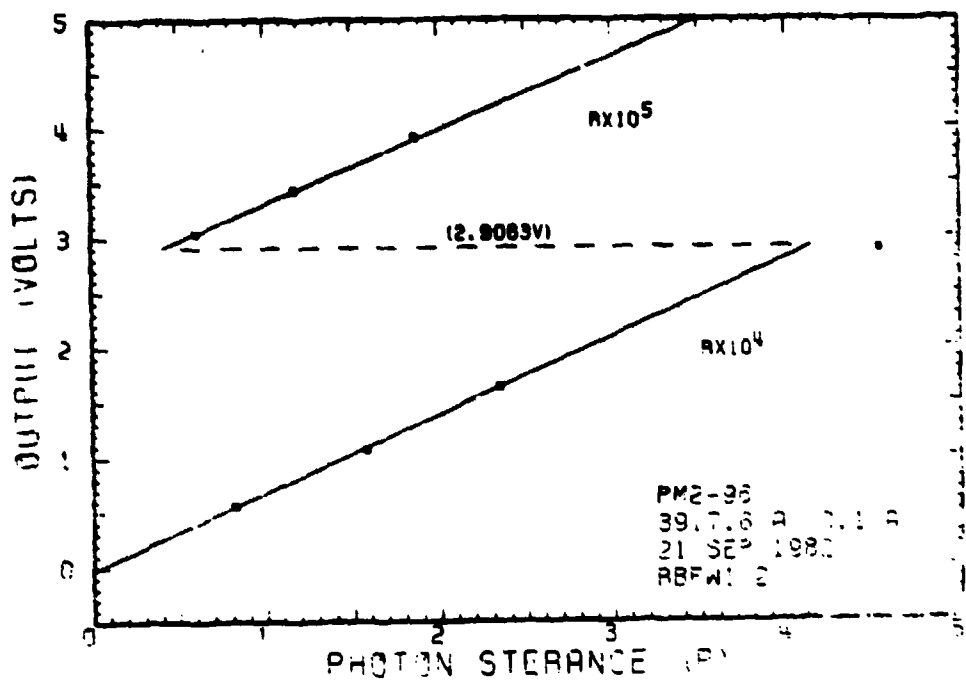


Figure C-6. Photometer PM2-96 output voltage vs. photon sterance calibration.

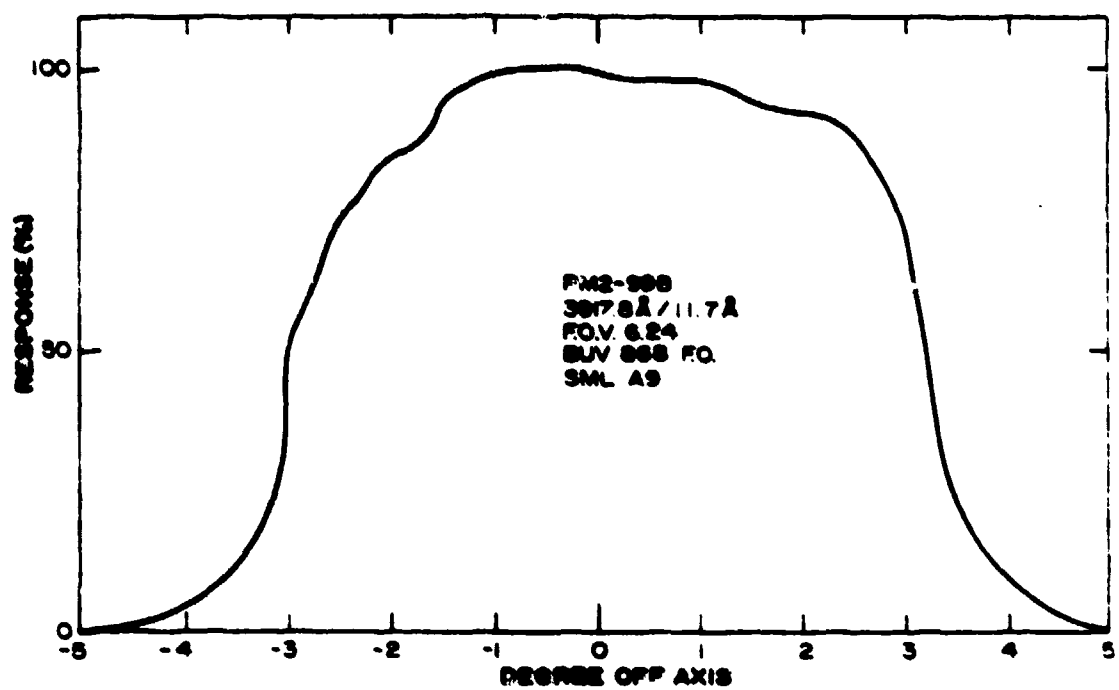


Figure C-7. Photometer PM2-998 field of view.

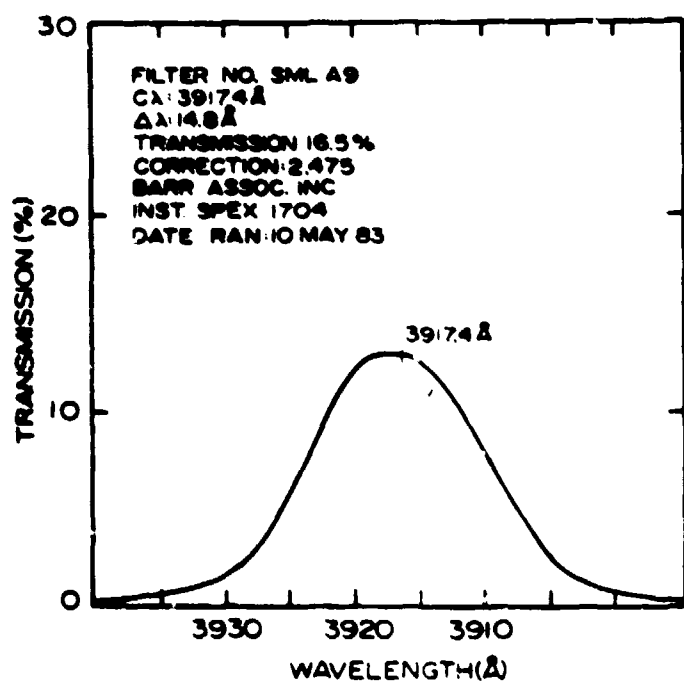


Figure C-8. Photometer PM2-998 filter transmission characteristics.

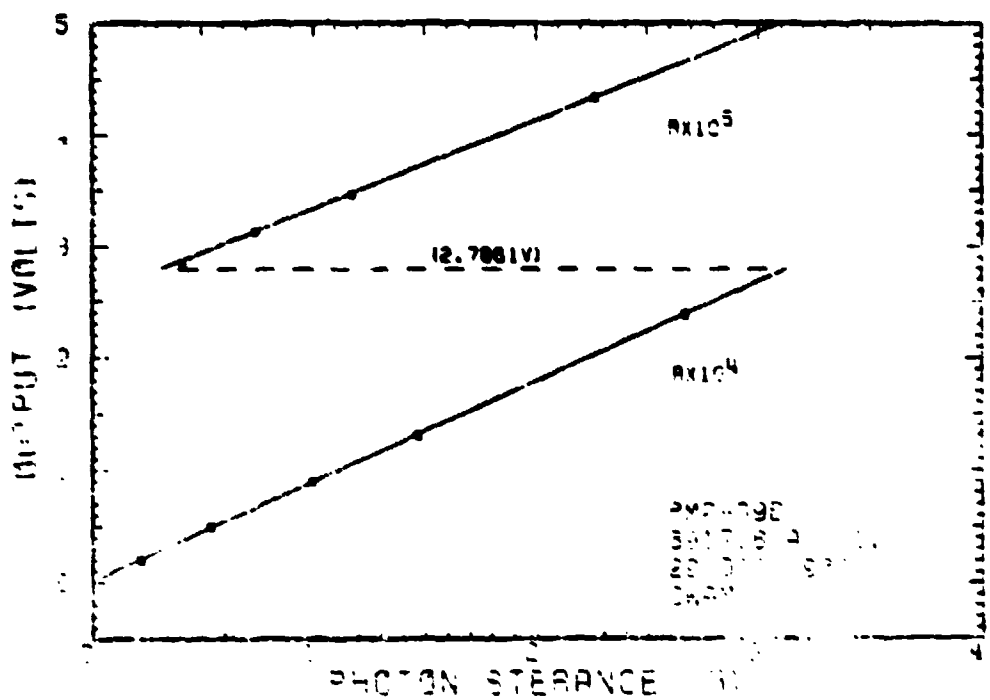


Figure C-9. Photometer PM2-99B output voltage vs. photon sterance calibration.

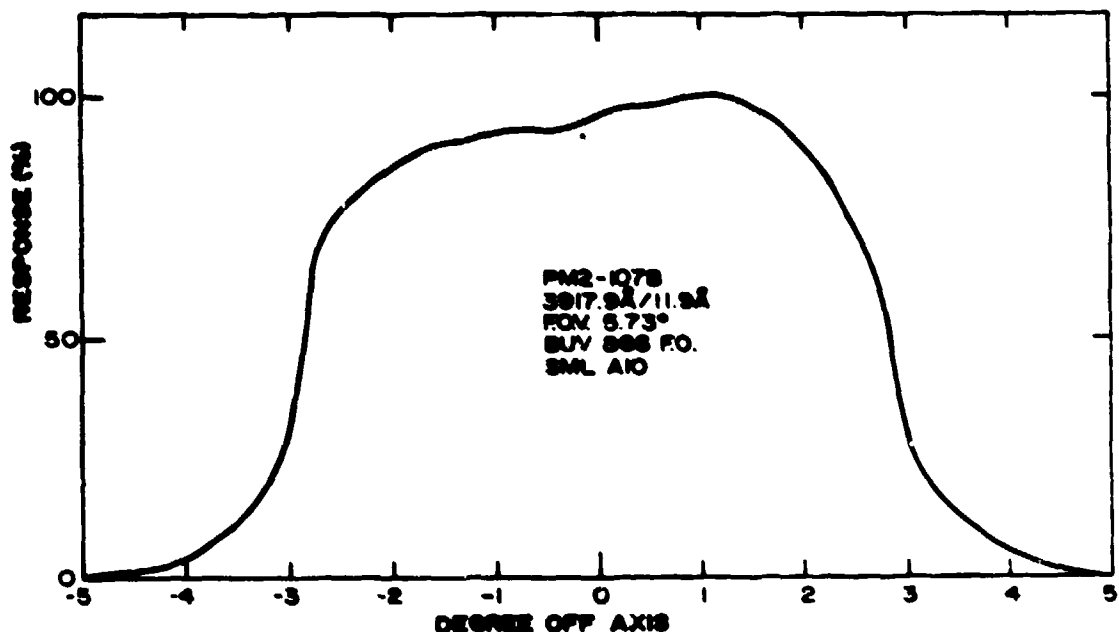


Figure C-10. Photometer PM2-107B field of view.

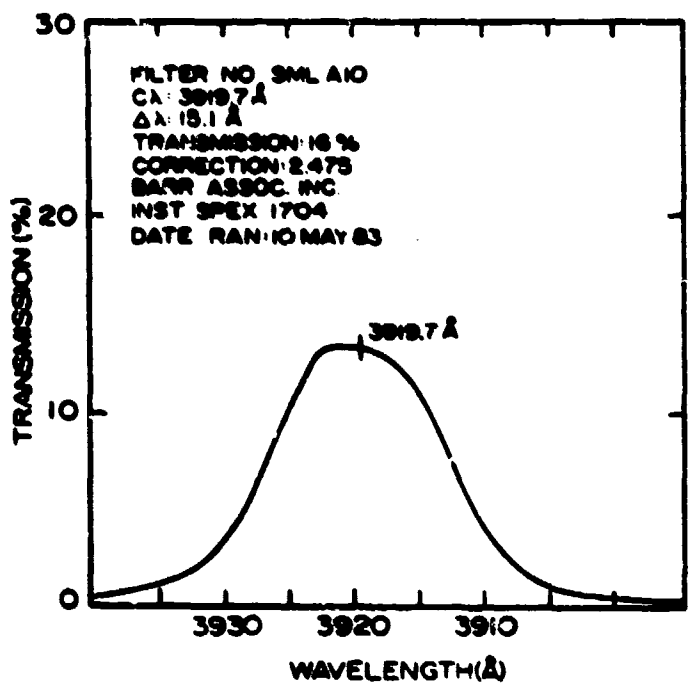


Figure C-11. Photometer PM2-107B filter transmission characteristics.

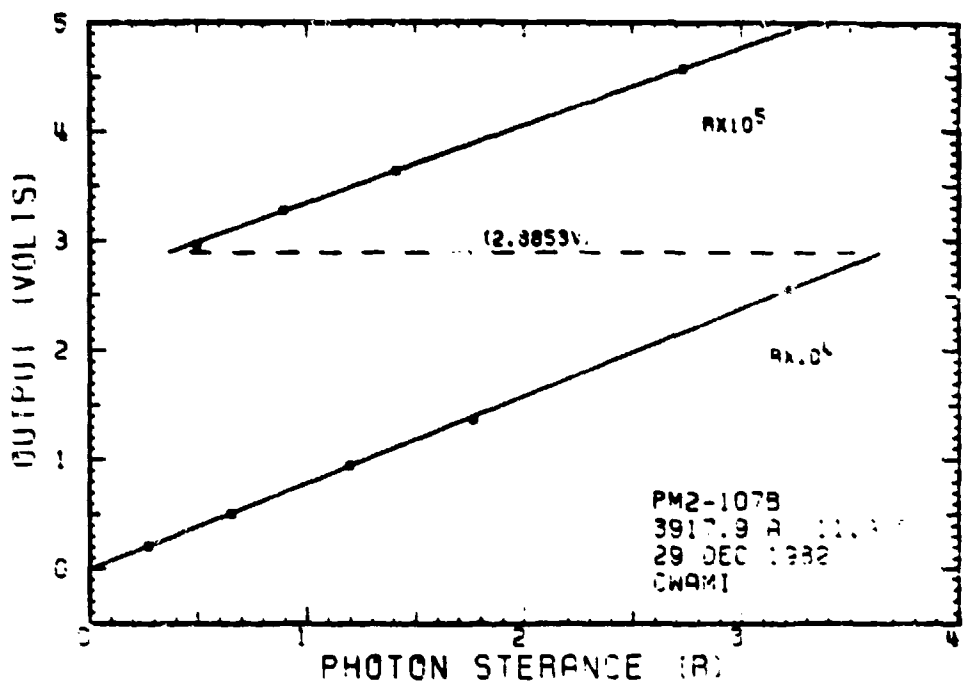


Figure C-12. Photometer PM2-107B output voltage vs. photon sterance calibration.